KEMIAN LAITOS
JYVÄSKYLÄN YLIOPISTO

Fluorescent SMILES nanoparticles

Master's Thesis

University of Jyväskylä

Department of Chemistry

25.6.2024

Nelma Peuhu

Abstract

The literature review of this master's thesis introduces the theory of small-molecule ionic isolation lattices (SMILES) materials and the preparation of SMILES nanoparticles. Furthermore, the basic concepts of analytical methods to study the characteristics of SMILES nanoparticles, including their size and optical properties, are discussed. The main focus of the thesis concerns the attractive fluorescent properties and effective energy transfer processes of SMILES nanoparticles, contributing to their promising bioimaging applications.

The aim of the experimental part was to investigate the energy transfer processes from the cyanostar anion complex to dye molecules in SMILES nanoparticles. This was conducted by preparing optically active SMILES nanoparticles containing rhodamine and DAOTA dyes and SMILES nanoparticles with an optically inactive cation. The SMILES nanoparticles containing optically inactive cations were prepared using imidazole and tetrabutylammonium cations to study the cyanostar anion complex. The energy transfer efficiency and the dominant energy transfer mechanism were determined.

The size of the nanoparticles was determined using dynamic light scattering (DLS) and cryo-transmission electron microscopy (cryo-TEM). Absorption and fluorescence spectroscopy were employed to investigate the fluorescent properties. Fluorescence lifetimes were measured using time-correlated single photon counting (TCSPC).

Tiivistelmä

Tämän opinnäytetyön kirjallisuuskatsaus käsittelee SMILES-materiaalien perusteoriaa sekä SMILES-nanopartikkeleiden valmistusta. Lisäksi tutkielmassa tarkastellaan analyyttisiä menetelmiä SMILES-nanopartikkeleiden optisten ominaisuuksien sekä koon määrittämiseksi. Tutkielmassa syvennytään erityisesti SMILES-nanopartikkeleiden fluoresoiviin ominaisuuksiin ja tehokkaisiin energiansiirtoprosesseihin, joiden tarkastelua pidetään tarpeellisina potentiaalisten biokuvantamissovellusten kannalta.

Opinnäytetyön kokeellisen osion tavoitteena oli tutkia energiansiirtoprosessia ja sen tehokkuutta pentasyanopentabentso[25] (cyanostar) -anionikompleksilta väriainemolekyylille SMILES-nanopartikkeleissa. Tätä varten valmistettiin rodamiini- sekä DAOTA-väriaineen sisältäviä optisesti aktiivisia SMILES-nanopartikkeleita sekä optisesti inaktiivisen kationin sisältäviä SMILES-nanopartikkeleita. Optisesti inaktiiviset SMILES-nanopartikkelit valmistettiin käyttäen imidatsoli- ja tetrabutyyliammoniumkationeja pentasyanopentabentso[25]anionikompleksin tutkimista varten.

Nanopartikkeleiden koko määritettiin dynaamisen valonsironnan (DLS) ja kryo-läpäisyelektronimikroskopian (cryo-TEM) avulla, kun taas fluoresenssiominaisuuksien tutkimiseen käytettiin absorptio- sekä fluoresenssispektroskopiaa. Fluoresenssin eliniät määritettiin hyödyntäen aikakorrelaatioon perustuvaa yksittäisen fotonin laskentaa (TCSPC).

Preface

The literature part of this master's thesis was written in the autumn 2023. The experimental part was performed at the Department of Chemistry at the University of Copenhagen, Denmark in spring 2024. The literature was searched via JykDok and Google Scholar, and some were provided by the supervisors.

The master's thesis was supervised by Maija Nissinen from University of Jyväskylä and hosted by Bo Wegge Laursen from University of Copenhagen to whom I would like to express my gratitude. I also want to thank Stine Stenspil for practical guidance. My interest in fluorescent dyes was first sparked during my bachelor's thesis, conducted under the guidance of Maija Nissinen. This inspired me to search for a research group specializing in the topic abroad, leading me to discover the ideal research group in Copenhagen.

In addition to my supervisors, many thanks are due to my colleagues in the research group for helping me with practical issues during the experimental part and to my student dormitory community for making my time in Copenhagen memorable. I would also like to thank the University of Jyväskylä for providing me with the opportunity and financial support to perform the experimental part of this thesis as an internship at the University of Copenhagen. Lastly, I am indebted to my partner and family, whose unwavering support has been essential to the completion of my master's thesis.

Table of contents

Abbreviations

SMILES	Small Molecule Ionic Isolation Lattices
NP	Nanoparticle
DAOTA	Diazaoxatriangulenium
ACQ	Aggregation caused quenching
AIE	Aggregation induced emission
IC	Internal conversion
FRET	Förster resonance energy transfer
ISC	Intersystem crossing
BODIPY	Boron-dipyrromethene
QD	Quantum dots
in vitro	Experiment performed outside of a living system
in vivo	Experiment performed within a living organism
AIEgens	Aggregation induced emission luminogens
DSPE-PEG	1,2-distearoyl-sn-glycero-3-phosphoethanolamine-polyethylene-glycol
THF	Tetrahydrofuran
PVP	Polyvinylpyrrolidione
PAA	Polyacrylic acid
$DiOC_6$	3,3'-dihexyloxacarbocyanine iodide
UV-Vis	Ultraviolet and visible
NIR	Near-infrared
TCSPC	Time-Correlated Single Photon Counting
FLIM	Fluorescence Lifetime Imaging
DLS	Dynamic Light Scattering
Cryo-TEM	Cryo-Transmission Electron Microscopy
IMZ	Imidazolium
TBA	Tetrabutylammonium
DCM	Dichloromethane

LITERATURE REVIEW

1 Introduction

Fluorescence is a critical phenomenon for a wide range of optical materials that emit light. Fluorescent materials have an important role in modern technologies and electronic devices such as light-emitting diodes[1], solar cells[2], sensors[3] and bioimaging reagents[2]. In particular, organic electronic materials provide an attractive starting point for constructing fluorescent materials, especially fluorescent nanoparticles (NP). When interacting with light, optical materials can undergo various photophysical processes leading to light emission. The widely tunable optical properties of organic molecular emitters, determined by their covalent structure, offer alternative possibilities for their applications in sensing and imaging. The advantage of organic dyes over inorganic nanoparticles is their high processability and flexibility.[2] In addition, they are free from toxic elements often present in inorganic NPs.[4,5]

Although organic fluorescent dyes are considered key components of optical materials, transferring their attractive optical properties from the solution state to densely packed solid-state materials is challenging. When fluorescent dyes are packed closely in the crystal structure, their electronic transitions are strongly influenced by the other chromophores. This leads to their electronic coupling to produce new excitonic states causing spectral shifts and fluorescence quenching. This undesired phenomenon called aggregation-caused quenching (ACQ) affects the brightness of the materials through the losses in light absorption and emission.[4,5]

Many strategies have been developed to prevent the aggregation-caused quenching and improve the brightness of organic fluorescent nanoparticles. The most common approaches are the introduction of space-filling groups, such as the covalent introduction of bulky side groups into organic dyes,[6] pairing cationic dyes with large counterions[7,8] and the use of aggregation-induced emission (AIE) dyes that are less sensitive to quenching.[9–11]

To solve the problem of strong coupling between dyes, ultrabright fluorescent nanoparticles offer an effective approach. Recently, a new class of extremely bright molecular crystals were discovered by the formulation of cationic dyes directly from solution into high-density ionic

lattices, called SMILES materials. These small-molecule ionic isolation lattices (SMILES) consist of cationic dye with cyanostar as an anion-receptor. The cyanostar anion complex provides spatial and electronic isolation of the dye molecules, diminishing the aggregation-caused quenching. Various commercial cationic dyes are suitable for making fluorescent SMILES crystals. These dyes include rhodamines, cyanines, trianguleniums, oxazines and styryls, all providing highly improved emission brightness exceeding all the previous fluorescent materials based on organic dyes.[5,12]

In addition to preventing aggregation-caused quenching, cyanostar molecules increase the fluorescence quantum yield of SMILES NPs by the excess of cyanostar molecules. Secondly, the cyanostar anion complex serves as a UV antenna by funneling the UV excitation energy to rhodamine dye and enhancing the brightness of SMILES NPs. A large molar absorption coefficient of cyanostar molecules in the UV region and effective energy transfer from cyanostar to fluorescent dye leads to efficient UV light energy harvesting processes that play an important role in future ultrabright fluorescent nanoparticles.[13]

For bioimaging applications, it is crucial for the fluorescent SMILES NPs to obtain colloidal stability and biocompatibility in aqueous systems. This is enabled by amphiphilic surface coatings.[14] With high brightness and biocompatibility, SMILES NPs together with cationic dyes provide a powerful approach for discovering advanced optical materials.[12]

2 Fluorescence

Fluorescence occurs in certain molecules, such as aromatic molecules, due to their delocalized π-electron systems that often have electronic energy levels suitable for fluorescence. The conjugated π-systems in aromatic rings lead to more efficient absorption and emission of light.[5,15] Also, many inorganic substances, such as quantum dots can exhibit fluorescence.[5] These fluorescent substances are called fluorophores.[16]

Fluorescence is an optical phenomenon where the substance first absorbs light or other electromagnetic radiation at a specific wavelength and then emits it at a longer wavelength. The emitted light is typically at lower energy. The processes occurring between the absorption and emission of light are illustrated by the Jablonski diagram (Figure 1).[16,17]

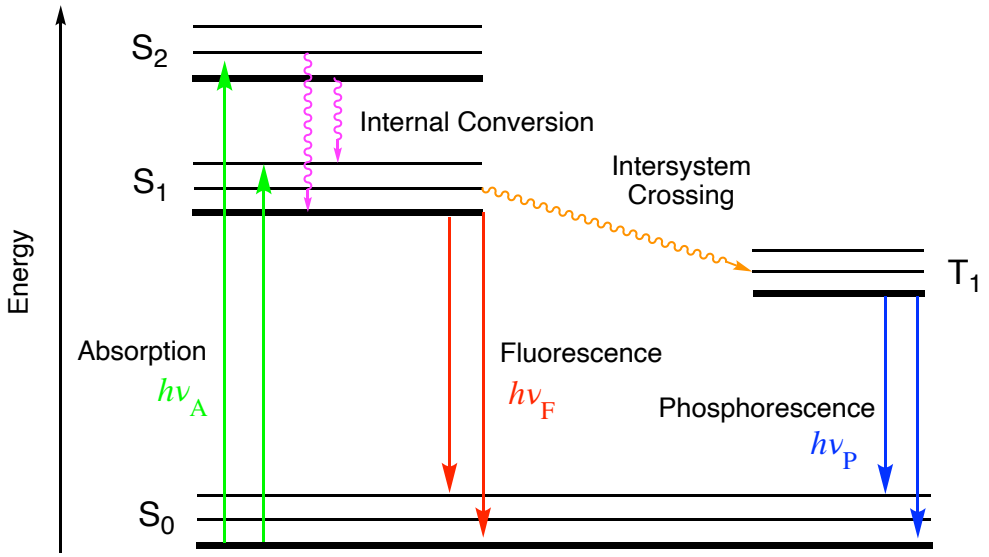

Figure 1. Jablonski diagram showing the excitation from ground state S_0 to first and second electronic states S_1 and S_2, internal conversion from S_2 to S_1, fluorescence from S_1 to S_0, intersystem crossing from S_1 to triplet state T_1, and phosphorescence from T_1 to S_0.[17]

Fluorescence is a three-stage process, the first of which is excitation. Light absorption at a certain wavelength excites the chromophore from the ground state to the excited states. A photon of energy $h\upsilon_A$ supplied by an external source interacts with a molecule that requires the same amount of energy for an electronic transition. A fluorophore absorbs the energy of a photon, and the outer electrons of the molecule redistribute from the ground state (S_0) to the excited electronic singlet state (S_1 or S_2). Subsequently, the energy of S_2 is partially dissipated, leading to internal conversion (IC), where the molecule relaxes to the lowest vibrational state of (S_1) within the femtosecond to the picosecond (fs-ps) time scale. The excited state S_1, from which fluorescence emission most commonly originates, exists for a limited time (typically 1-10 ns). During the final process, the energy of a photon is emitted causing the fluorophore to return from the excited state (S_1) to the ground state (S_0). Due to the energy loss of the excited state, the emitted photon is lower in energy and, therefore, longer in wavelength than the excitation photon. The difference in absorbed and emitted wavelengths or energies is defined as Stokes sift.[2,16,17]

However, not all the molecules immediately after excitation return to the ground state, leading to fluorescence. Other pathways depopulating S_1 are possible, such as vibrational relaxation to S_0, which involves the conversion of energy into heat without emitting light, as well as

collisional quenching and Förster resonance energy transfer (FRET). In these processes the energy is dissipated non-radiatively.[2,16,17]

Another non-radiative transition alternative to fluorescence is intersystem crossing (ISC), where molecules in the S_1 state undergo a spin conversion to the first excited triplet state T_1. This process occurs if the energy gap between singlet and triplet states is sufficiently small. The emission of photons from T_1 to S_0 is known as phosphorescence. The excited T_1 state has a longer lifetime (microseconds to seconds) and the emission is shifted to longer wavelengths and lower energy compared to fluorescence.[2,17]

2.1 Organic fluorophores

A molecule with fluorescent properties is called a fluorophore. Common commercially available organic fluorophores include fluorescein, Alexa Fluor dyes, BODIPY, cyanine and rhodamine dyes.[16,18] Fluorophores can act as fluorescent probes designed to respond to a specific stimulus or to locate a specific region in a biological sample.[16] This makes them valuable tools in various fields, including biology and medicine.[18]

Fluorophores can re-emit light upon light excitation. Most organic fluorophores consist of conjugated systems, including multiple aromatic rings. As well known, π-π interactions are widely present in organic fluorophores with an aromatic conjugated system.[8,19] The fluorophores with large π-planes tend to π-stack and form H- and J-aggregates with low quantum yields. H-aggregates occur when aromatic molecules stack primarily in a face-to-face arrangement with overlapping π-electron clouds resulting in a blue shift (hypsochromic shift) in the absorption and a red shift in the emission spectrum. In contrast, aggregates with absorption bands shifted to a longer wavelength (bathochromically shifted) are called J-aggregates. Herein, the π-electron overlapping is caused by the head-to-tail stacking of aromatic molecules.[20]

Since the π-π interactions between molecules are strong in the solid state, most fluorophores consume their excited state energy in the non-radiative process, leading to self-quenching and weak solid-state fluorescence. To obtain efficient solid-state emitters, it is important to overcome these strong π-π interactions. Various methods to prevent the formation of non-fluorescent aggregates and enhance solid-state emission have been presented in recent years.

Overcoming the current limitations of organic fluorophores would provide new insights for developing raw materials for biomedical applications such as bioimaging and biosensing.[8,19]

Many organic fluorescent molecules have demonstrated potential in the imaging-driven clinical treatment of cancer. Despite this, their practical applications have encountered challenges due to their poor photostability, low water solubility and lack of tumor targeting ability. Different strategies to improve the optical and biological properties of the fluorescent materials have developed, including an effective packing of small fluorescent molecules as nanoprobes.[15] In the last few years, molecules with bright aggregation-induced emission (AIE) have been successfully utilized in preparing organic fluorescent nanoparticles as robust in vitro and in vivo bioimaging probes. Unlike the traditional organic fluorescent molecules with aggregation-induced quenching (ACQ) effect, the aggregation-induced emission luminogens (AIEgens) show strong emission upon aggregation. Although these high-performance fluorescent molecules with versatile functionalities and superior optical properties have demonstrated great potential in various imaging and therapeutic applications, there are still challenges to be overcome before practical applications. Future research and development of these materials should focus on developing increasingly biodegradable and biocompatible materials and new materials to solve the aggregation-caused quenching.[10,21]

3 SMILES

A new class of organic fluorescent materials, SMILES, with super-bright emission, have been discovered by Laursen, Flood and coworkers.[12] These small-molecule ionic isolation lattices consist of fluorescent dyes packed together in a crystal lattice with a cyanostar macrocycle. The well-defined SMILES lattice is made of an alternating array of cationic dyes and cyanostar anion complexes. The cyanostar anion receptor assembles around the counter anions inducing alternating charge-by-charge packing, which isolates the dye molecules from each other. The ionic crystallization with cyanostar causes the electronic and spatial isolation of the fluorophores. The hierarchical assembly produces spatial isolation, where the dye's counter anions form 2:1 disc-shaped complexes with cyanostar.[12,22] In SMILES crystals (Figure 2), the spatially and electronically isolated dye molecules avoid self-quenching and retain their attractive properties observed in dilute solution.[12]

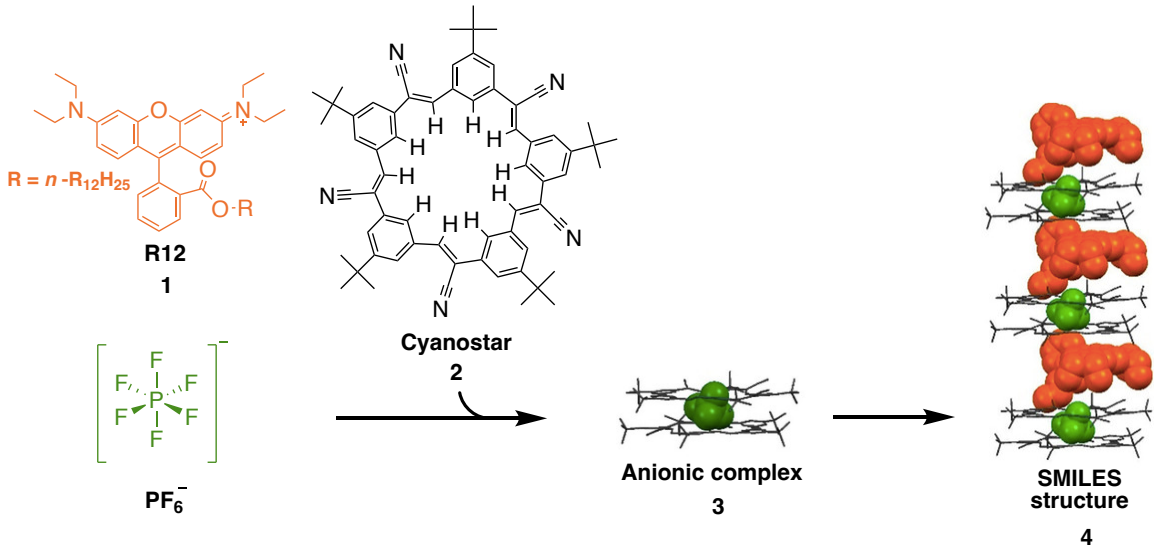

Figure 2. Schematic illustration of SMILES structure. The molecular structure of rhodamine R12 **1** and cyanostar anion receptor CS **2**, which binds the PF_6^- ion in a 2:1 anionic complex **3**. SMILES structure **4** is formed by the crystallization of the cationic dye with cyanostar anion complex.[13] Reproduced with permission from Chen, J.; Fateminia, S. M. A.; Kacenauskaite, L.; Bærentsen, N.; Grønfeldt Stenspil, S.; Bredehoeft, J.; Martinez, K. L.; Flood, A. H. ja Laursen, B. W., Ultrabright Fluorescent Organic Nanoparticles Based on Small-Molecule Ionic Isolation Lattices, *Angew. Chem. Int. Ed.*, **2021**, *60*, 9450–9458, copyright 2021, published by John Wiley and Sons, https://creativecommons.org/licenses/by-nc-nd/4.0/.

SMILES materials work as plug and play, meaning that any commercial cationic dye can be plugged into an ionic SMILES lattice. This requires considering the key design rules established by the control studies of Laursen, Flood and coworkers.[12] The control study included the use of commercial dyes (xanthenes, oxazines, styryls, and cyanines) to prove the generality of electronic isolation of dyes using cyanostar. The isolation of dyes results from using colorless cyanostar anion complexes with a wide 3.45 eV bandgap. According to the control studies, the two design rules state that the dye must be 1) spatially and 2) electronically isolated. These design rules provide the basis for the preparation of SMILES materials and solve the problem of emission quenching of fluorophores. No other method offers such a wide range of applications as the wide bandwidth of cyanostar complexes.[12]

3.1 Preparation of SMILES nanoparticles

SMILES can be easily prepared by mixing the cyanostar macrocycles and the cationic dyes in a simple 2:1 ratio. The materials can be formulated into any form, from thin films, crystals, powders, and nanoparticles, and dissolved in polymers for solution casting, extrusion, and 3D printing. Transferring the SMILES materials into SMILES nanoparticles without performance degradation could offer potential applications notably in bioimaging. The preparation of SMILES NPs precursor solution involves dissolving all the necessary components needed to form SMILES NPs in an appropriate solvent and removing the solvent. A remarkable feature of SMILES NPs preparation is that the whole process, including the preparation of the precursor solution and the formation of SMILES NPs, can be completed within 10 minutes.

Flood, Laursen and coworkers[13] presented the synthesis of SMILES NPs using an antisolvent nanoprecipitation method. The SMILES NPs precursor solution was prepared by dissolving the cationic dye, here lipophilic rhodamine (R12) **1** PF_6^- salt, and the cyanostar anionic receptor **2** in tetrahydrofuran (THF). The SMILES NPs were formed by injecting the precursor solution (520 µl) into a large volume (10 ml) of water under 1 min of sonication. The red transparent and highly fluorescent aqueous solution displayed the successful formation of SMILES NPs with a broad size distribution (25 ± 8 nm). As a reference, similar R12 THF solutions without lattice-forming cyanostar were used in the nanoprecipitation method. After injecting the control precursor solution into water, the formed colloids showed aggregated structures, referred to as R12 aggregates, displaying a broadened and red-shifted absorption and weak fluorescence emission. Moreover, the fluorescence of SMILES NPs differed from the control sample without cyanostar, which did not show fluorescence under UV excitation. The absorption and fluorescence studies confirmed that when preparing the SMILES NPs from the R12 precursor solution with 2.5 molar equivalents of cyanostar, SMILES NPs showed similar absorption and emission spectral shapes as the solution of the R12 dye dissolved in THF. Also, the brightness per volume (*B/V*) of the R12 SMILES NPs reached a maximum (4,725 M^{-1} cm^{-1}/ nm^3) with 2.5 molar equivalent of cyanostar.

However, since Laursen, Flood and coworkers[12] in their study verified that all the major commercial dyes, including rhodamines, cyanines, xanthenes, styryls, and trianguleniums, produce fluorescence in the solid state, the properties of SMILES materials can be generalized. This allows the use of other commercial dyes in addition to rhodamine in the manufacture of SMILES NPs.

3.2 Stabilizing SMILES nanoparticles by capping with polyethylene glycol amphiphiles

Since bioimaging is considered one of the most important applications of SMILES NPs due to their brightness and high quantum yield, it is essential to enhance their biocompatibility and colloidal stability by capping the SMILES NPs with amphiphilic materials.[13] Already in the early studies of SMILES materials, the compatibility of SMILES doping with water-soluble polymers such as polyethylene glycol (PEG), polyvinylpyrrolidone (PVP) and polyacrylic acid (PAA) have been demonstrated.[12]

Flood, Laursen and coworkers[13] reported the use of polyethylene glycol-based detergent 1,2-distearoyl-sn-glycero-3-phosphoethanolamine-polyethylene glycol (DSPE-PEG) (Figure 3) as an amphiphilic surface capping agent for SMILES NPs. DSPE-PEG derivatives are optimal capping agents for the surface of hydrophobic SMILES NPs. Due to their amphiphilic structure and self-assembly, DSPE-PEG derivatives tend to aggregate and encapsulate the SMILES NPs inside the core, while the hydrophilic chains act as a shell for stabilizing the resulting nanoparticles. These surface-encapsulated SMILES NPs can be prepared by dissolving the DSPE-PEG **5** in the previously described THF precursor solution during the nanoprecipitation process (Chapter 3.1) (Figure 4).[13]

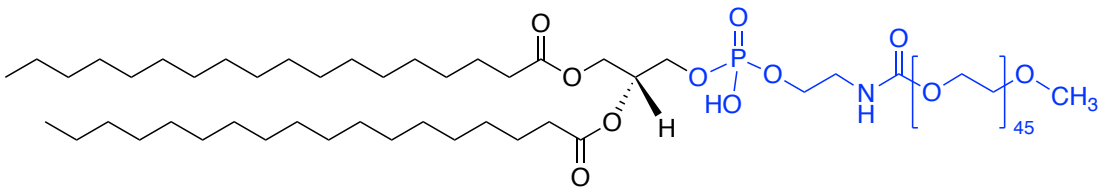

5

Figure 3. The structure of DSPE-PEG **5**.

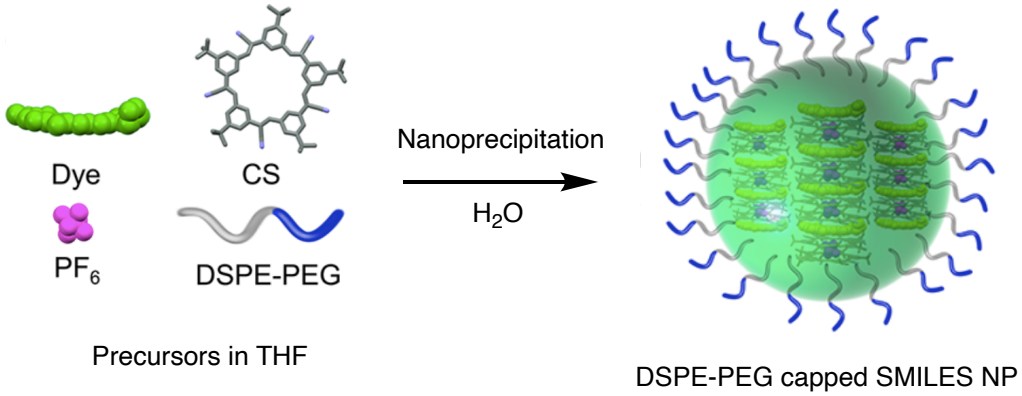

Figure 4. Schematic illustration of the preparation of DSPE-PEG capped SMILES NPs through nanoprecipitation.[23]

The obtained surface-capped SMILES NPs were smaller and showed a narrower size distribution than SMILES NPs without the capping agent.[13] In addition, the NPs prepared without the capping agent showed agglomeration over time. However, the SMILES NPs with DSPE-PEG capping displayed colloidal stability and higher photostability in water compared to the R12 dye in THF solution. Moreover, DSPE-PEG has been reported to prevent the NPs agglomeration and reduce their toxicity in *in vivo* imaging.[13,24]

4 Analytical methods to study SMILES nanoparticles

The optical properties, such as maximum absorption and emission wavelengths, molar absorption coefficient, fluorescent quantum yield and lifetime, are important factors in characterizing organic fluorescent dyes. The absorption properties of organic fluorescent dyes are significant parameters for designing fluorescent dyes for specific applications in various research fields, including bioimaging and phototherapy. Similarly, the fluorescence properties characterized by the maximum emission wavelength, excited state lifetime and bandwidth are essential in developing fluorescent dyes, sensors, and emitters.[25]

Several analytical methods are employed to study the optical properties of organic fluorescent dyes. These include UV-visible spectroscopy for measuring the absorption and emission

spectra[26], fluorescence spectroscopy to study specifically the emission properties of fluorescent dyes[27] and time-correlated single photon counting (TCSPC), particularly to determine the fluorescence lifetime of the dyes.[28]

Furthermore, other techniques, such as dynamic light scattering (DLS), can be employed for comprehensive nanoparticle characterization. DLS is ideal for determining the particle size and size distribution by measuring the hydrodynamic diameter of the nanoparticles. Particle size characterization is crucial for understanding the physical dimensions of the particles in the sample. The changes in size over time can be related to changes in the optical properties of fluorescent nanoparticles. DLS is also valuable for measuring the stability in solutions and suspensions under varying environmental conditions and during the preparation of nanomaterials.[29]

A more precise technique for nanoparticle size analysis is Cryo-TEM, which offers several advantages over the other size analysis methods by providing more detailed information about the size distribution, structure, and morphology of nanoparticles. With high-resolution images of individual nanoparticles, the cryo-TEM allows accurate measurements of the size and shape of nanoparticles.[30,31]

4.1 Absorption spectroscopy

Absorption spectroscopy is a widely used spectroscopic technique for measuring the absorption of electromagnetic radiation as a function of the wavelength or frequency of the incident light. It is broadly applied in various fields of chemistry, material science and physics to characterize the electronic structure of compounds. Absorption spectroscopy is a versatile technique for studying the interaction of light with matter, providing valuable information about the chemical composition and optical properties of different materials.

When radiation interacts with matter, the energy of a photon is transferred to the matter. If the energy of a photon is equal to the energy between the ground state and the excited state of an electron in an atom or molecule, the electron can absorb the energy of a photon. When a molecule absorbs light, the energy of the molecule increases, causing a transition of electrons from the ground state to a higher energy or excited state. Excitation of atoms to higher energy states requires different amounts of energy, which determines their absorption. The wavelength

of light absorbed by a molecule depends on the different energy levels and electronic distribution of the material. The energy of a photon and wavelength are related by

$$E = h\nu = h\frac{c}{\lambda}, \quad (1)$$

where ν is frequency, h is Planck's constant, c is the speed of light in vacuum (2.998×10^8 m/s) and λ is the wavelength.[26,27]

Since the amount of energy is inversely proportional to the wavelength, longer wavelengths contain less energy, and shorter wavelengths contain more energy. Because atoms absorb and emit light at specific wavelengths, absorption spectroscopy can be used to identify the chemical compound and determine the concentration of a substance in a sample. In absorption spectroscopy, the light is propagated through the sample, and the amount of light that passes through the sample is measured and compared to that of a reference sample. The amount of light absorbed by the sample is expressed as absorbance. The absorbance can be measured from the incident light and the light that passes through a sample, which is called transmittance:

$$A = \log_{10}\left(\frac{I_0}{I}\right) = -\log T, \quad (2)$$

where A is absorbance, I_0 is the intensity of the incident light, I is the intensity of transmitted light, and T is transmittance.[27]

The light absorbed is directly proportional to the sample concentration and path length. The absorbance is presented using the Beer-Lambert Law:

$$A = \varepsilon cL, \quad (3)$$

where ε is the molar absorption coefficient, c is the concentration of the absorbing species, and L is the path length.[27]

Absorption spectroscopy is employed as an analytical technique for the quantitative analysis and identification of compounds. Near-infrared (NIR) and ultraviolet-visible (UV-Vis) spectroscopy are commonly used in analytical applications. UV-Vis spectroscopy uses the ultraviolet (180 to 380 nm) and visible (380 to 780 nm) regions of the electromagnetic spectrum,

and infrared spectroscopy uses the lower-energy infrared region. UV-Vis spectrophotometry is primarily used to determine the concentration of a substance in a sample, whereas IR-spectroscopy can be used to determine the chemical functional groups in a sample by analyzing their vibrational frequencies at which infrared radiation is absorbed.[27,32,33]

4.1.1 UV-Vis spectrophotometry

UV-Vis spectrophotometer consists of a light source, monochromator, filters, sample and reference cuvettes, detector and signal processors and readout devices for reading the data. The most widely used light sources include deuterium and hydrogen lamps, xenon arc lamps and tungsten/halogen lamps. A tungsten lamp is a notable light source which provides a broad wavelength distribution of visible and near-infrared wavelengths from 320 to 2500 nm. Deuterium and hydrogen lamps provide continuous radiation in the ultraviolet region. A typical UV-Vis spectrophotometer switches between deuterium and tungsten lamps always using the source of the highest intensity.[27,32,33]

In the simplest UV-Vis spectrophotometer, including a single-beam optical system, ultraviolet or visible light from a continuous light source is passed through a monochromator, where a narrow band of wavelengths is selected from the incident beam of light. The monochromatic light travels through a sample in a sample cuvette and then passes to the detector. However, a blank sample used as a reference must be measured before the sample measurement. In practice, the baseline is measured separately from the sample using the solvent. The possible variation of light intensity in the baseline measurement may cause inaccuracy in the absorbance results.[27,32]

Most modern UV-Vis spectrophotometers are based on the more accurate dual-beam design, where the radiation from the monochromator is split into two beams. In a dual-beam-in-space instrument the radiation is split by a beam-splitter mirror and the two beams pass simultaneously through the sample and reference cuvettes before reaching two matched photodetectors (Figure 5). In a dual-beam-in-time spectrophotometer, the two beams are formed by a rotating mirror. The rotating mirror directs the two beams into and out of the light path, passing the sample and reference cuvettes alternately before striking a single photodetector (Figure 6). The intensity of the solution cuvette used as a reference is taken as 100 % transmittance. Both outputs are amplified, and the displayed result is the ratio of the two beams.

Because two beams with the same wavelength are provided, the sample and the reference can be measured simultaneously, allowing the correction of instrument variations in real-time. These real-time corrections provide a highly accurate measurement environment. The results of UV-Vis spectroscopy are usually presented as an absorption spectrum, a plot of absorbance as a function of wavelength.[27,32]

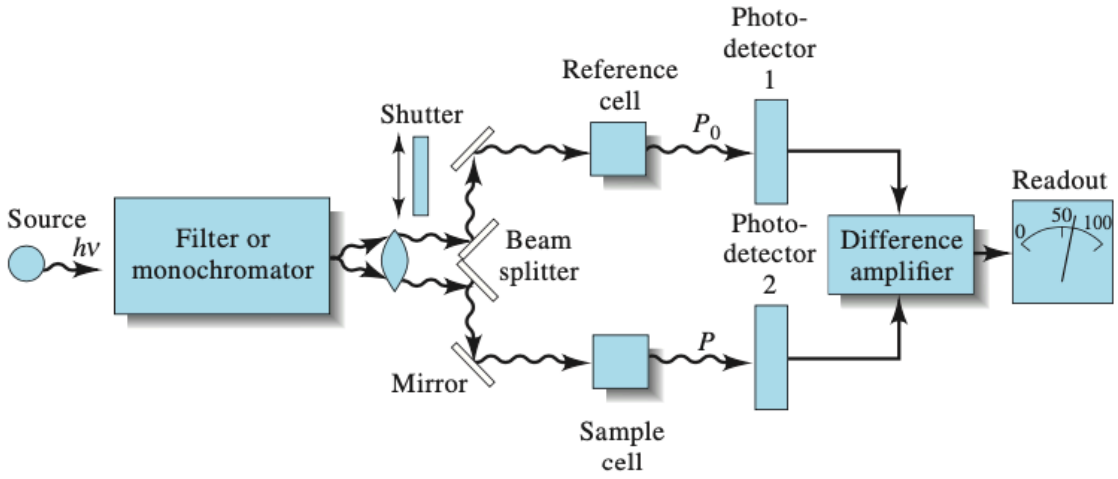

Figure 5. Instrumental design of dual-beam-in-space UV-Vis spectrophotometer. The radiation from the monochromator is split into two beams by a beam splitter. The beams simultaneously pass through the sample and reference cuvettes before striking the two detectors.[32] Cengage Learning Inc. Reproduced by permission. www.cengage.com/permissions.

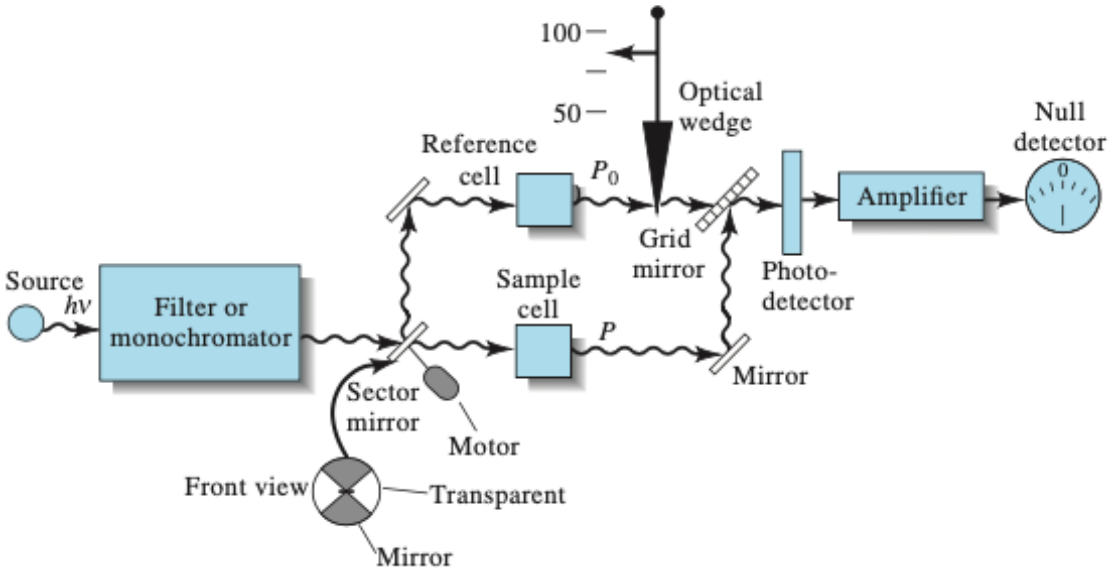

Figure 6. Instrumental design of dual-beam-in-time UV-Vis spectrophotometer. The beam is alternately directed through sample and reference cuvettes by a rotating mirror before reaching a single photodetector.[32] Cengage Learning Inc. Reproduced by permission. www.cengage.com/permissions.

4.1.2 Applications of absorption spectroscopy

Absorption spectroscopy is applicable for both qualitative and quantitative analysis. In quantitative analysis, the concentration of a substance in a sample is determined by measuring the absorption of light at a particular wavelength. In qualitative analysis absorption spectroscopy offers qualitative information about the composition and the functional groups or chromophores in a sample. The fluctuations in light absorption at different wavelengths due to the different electronic structures of compounds enable the identification of particular molecules within a sample.[26,32,33]

Absorption spectroscopy also provides information about energy levels, electronic transitions, and molecular vibrations of the sample. Due to their versatility and ability to provide valuable optical information, absorption spectroscopy is employed in various industries and high-end material science, such as the analysis of solar cells and optical components, as well as in biotechnology and pharmaceutical applications. With ultra-high performance and flexibility, UV-Vis spectroscopy can be used to analyze the optical properties and electronic structure of a wide range of advanced nanomaterials, including SMILES materials.[34]

One of the most important absorption parameters of optical materials, the molar absorption coefficient, ε, can be determined by measuring the absorbance with UV-Vis spectroscopy. For SMILES materials, the molar absorption coefficient of rhodamine (R12) in the SMILES structure can be determined by measuring the maximum absorbance at 560 nm at known concentrations. The absorbance is measured at 560 nm because rhodamine exhibits a strong absorption peak at that wavelength. According to Beer-Lambert law and the linearity between absorbance and concentration of the compound (Formula 3), the slope of the interpolated line is expressed as the molar absorption coefficient. Flood, Laursen and coworkers[13] determined the molar absorption coefficient for R12 SMILES nanoparticles to be 97 000 $M^{-1}cm^{-1}$ using the absorption coefficient of R12 in THF (120 000 $M^{-1}cm^{-1}$). With the determined molar absorption coefficient of the nanoparticles, they calculated the brightness for R12 SMILES nanoparticles to be 24250 $M^{-1}cm^{-1}$.[13]

4.2 Fluorescence spectroscopy

Fluorescence is a photoluminescence process in which atoms or molecules are excited by absorption of electromagnetic radiation (Chapter 2). Fluorescence occurs as the emission of light when the excited atoms or molecules relax to the ground state. Fluorescence spectroscopy is more sensitive than absorption spectroscopy. Therefore, it is possible to observe single molecules by fluorescence spectroscopy.[27,32]

Fluorescence is measured by exciting the sample with an excitation wavelength and measuring light emission at a longer wavelength. The sample is illuminated with monochromatic light, the energy of which can be absorbed by the compounds in the sample. Typical light sources in fluorescence instruments are xenon, mercury and xenon-mercury arc lamps and lasers. The absorbed photons excite the electrons and cause them to emit light. The emitted light is directed to a filter or monochromator and onto a detector where the photons are detected, and their intensities and frequencies are analyzed. Fluorescence measurements provide information about the excited states and structural properties that can be useful for molecular identification or studying molecular changes.[27,32]

In a fluorescence spectrophotometer the excitation wavelength is selected with a monochromator and the emitted light is detected with another monochromator, usually positioned at a 90° angle to the excitation light (Figure 7). The position of the other detector minimizes the intensity of the scattered light entering the detector. The detector analyses the intensity of emitted light and distinguishes its wavelength distribution. If the excitation wavelength is kept constant, an emission spectrum is produced. The emission spectrum is a graph of emission intensities as a function of emission wavelength. The excitation spectrum can be measured by keeping the emission wavelength constant and varying the excitation wavelength. An excitation spectrum is a graph of emission intensities as a function of excitation wavelength.[27,32]

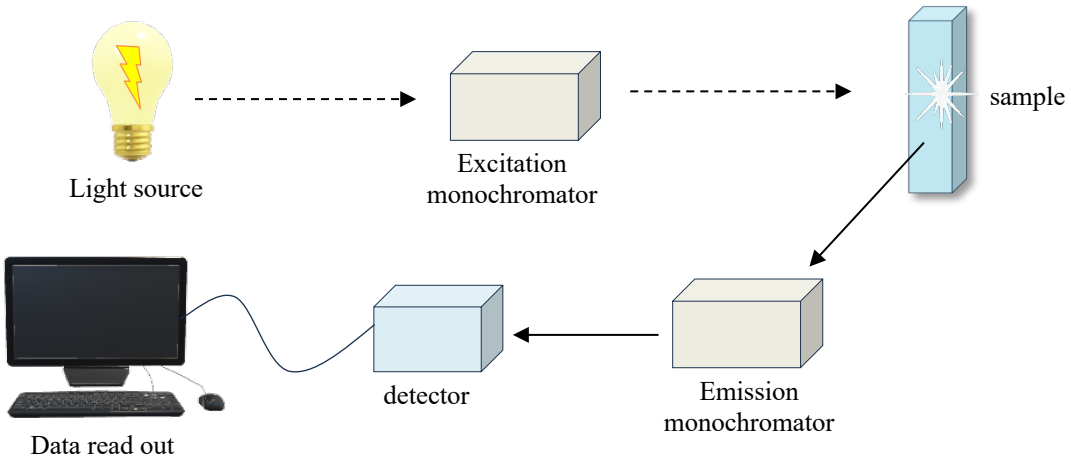

Figure 7. Instrumental setup of fluorescence spectrophotometer. The excitation monochromator selects the excitation wavelength λ_{ex} and the emission monochromator analyzes the emitted light λ_{ex}.

4.2.1 Characterization of fluorescent properties

The most important characteristics of fluorophores are the quantum yield and fluorescence lifetime. Fluorescence quantum yield is the ratio of photons absorbed to photons emitted through fluorescence.[17]

$$\Phi = \frac{\text{number of photons emitted through fluorescence}}{\text{number of photons absorbed}} \tag{4}$$

When focusing on the fluorescence processes from the excited state to the ground state (discussed in Chapter 2), the emissive rate of the fluorophore Γ and its rate of non-radiative relaxation process k_{nr} to S_0 are the key determining factors of quantum yield. Therefore, quantum yield is defined by the fraction of excited state fluorophores that decays through emission, given by

$$\Phi = \frac{\Gamma}{\Gamma + k_{nr}} \tag{5}$$

The substances with the highest quantum yields display the brightest emission. An example of such a substance is rhodamine. The other relevant parameter when considering the fluorescent properties of substances is fluorescence lifetime. Fluorescence lifetime is the average time a

fluorescent molecule spends in the excited state before emitting a photon and returning to its ground state. It is considered an important feature, as it determines the time available for the relaxation process of the fluorophore resulting in the relaxed S_1 state.[17] However, when observing the fluorophore's decay to S_0, the fluorescence lifetime can be expressed in terms of rate constants as follows:

$$\tau = \frac{1}{\Gamma + k_{\mathrm{nr}}} \tag{6}$$

Fluorescence spectroscopy enables the determination of fluorescence quantum yield using relative and absolute quantum yield methods. In the relative quantum yield method, the fluorescence quantum yield is calculated by comparing the fluorescence intensity of a sample to that of a reference sample with a known quantum yield. Common fluorescent standards with known and relatively high fluorescence quantum yield include rhodamine 6G, quinine sulfate and fluorescein. The emission spectra of the sample and reference standard are measured under identical measurement conditions using the same excitation wavelength. The ratio of the integrated fluorescence intensities is used to calculate the quantum yield of the sample.[35,36]

In the absolute quantum yield method, an integrating sphere is used to collect all the photons emitted from the sample without the need for a reference sample. The absolute fluorescence quantum yield is thus calculated simply by comparing the total number of emitted photons to the total number of absorbed photons. Because a reference standard is not required, this method provides a faster measurement of quantum yield since the quantum yield can be obtained directly from a single measurement. Secondly, a wider range of emission wavelengths is available that are not limited by the reference sample wavelengths. This method can be applied to different sample types from solutions to solids, and it is particularly suitable for samples that absorb and emit in wavelength ranges for which reliable reference samples exist.[35,36]

A common parameter needed to optimize the emissive materials is brightness (B). The brightness of molecular materials is defined as the ability of the material to absorb the excitation light (molar absorption coefficient, ε) and its ability to emit light (fluorescence quantum yield, ϕ), giving the formula:

$$B = \varepsilon \times \phi \tag{7}$$

For organic fluorescent nanoparticles, the brightness could be defined by the number of dyes (n) in the particle.[5]

$$B = n \times \varepsilon \times \phi \tag{8}$$

Nevertheless, when considering the bioimaging applications of fluorescent nanoparticles, the pursuit of brighter and larger particles is countered by a preference for smaller particles.[14] Therefore, the brightness per unit volume (B/V) is used to describe the brightness regardless of particle size and to compare the efficiency of different materials.[5] For SMILES materials, the brightness per volume is presented as follows, assuming the density of the considered materials to be $1\ \mathrm{g/cm^3}$:

$$B/V = \frac{\varepsilon \times \phi}{V_{\mathrm{per\ dye}}}, \tag{9}$$

where $V_{\mathrm{per\ dye}}$ is the molecular volume of one dye together with the composition of n molar equivalents of cyanostar. $V_{\mathrm{per\ dye}}$ can be calculated with formula weight using the following formula:

$$V_{\mathrm{per\ dye}} = \frac{FW_{\mathrm{dye}} + n \times FW_{\mathrm{CS}}}{N_{\mathrm{A}} \times 1\ \mathrm{g/cm^3}}, \tag{10}$$

where FW_{dye} is the formula weight of dye, FW_{CS} is the formula weight of cyanostar, n is the molar equivalent number of cyanostar, and N_{A} is Avogadro's constant.

For DSPE-PEG capped SMILES nanoparticles, the $V_{\mathrm{per\ dye}}$ can be calculated by taking into consideration the DSPE-PEG capping agent by the following formula:

$$V_{\mathrm{per\ dye}}(\mathrm{wt\%DSPE-PEG}) = \frac{V_{\mathrm{per\ dye}}(\mathrm{wt\%DSPE-PEG} = 0)}{(1 - \mathrm{wt\%DSPE-PEG})}, \tag{11}$$

4.3 Time-Correlated Single Photon Counting (TCSPC)

Time-correlated single photon counting is a special form of time-resolved fluorescence spectroscopy. It is a common analytical technique used to measure fluorescence decay over time. Thus, it has become one of the standard techniques for fluorescence lifetime imaging (FLIM). In TCSPC, the time required for a single photon to be emitted from a fluorescent dye after excitation is measured and the emission times are correlated at high time resolution. TCSPC exploits low-level light intensity and high-repetition rate signals so low that the probability of detecting more than one photon in a single signal period is negligible.

In TCSPC, a pulsed laser excites the fluorescent dyes while a reference pulse from the laser is used as a start signal to initiate the counting electronics. A photon emitted by the fluorescent dye is detected using a photodetector. The detector converts a single photon into an electronic pulse, and the arrival time of this pulse is measured with respect to the excitation pulse. Hence, the emitted photon is used as a stop signal to record the time it takes to detect the photon. After a large number of photons has been detected and accumulated in the memory, TCSPC builds up a histogram of the photon times. The result is a distribution of the photons over the time after excitation pulses, i.e. the waveform of the optical pulse (Figure 8).[28,37]

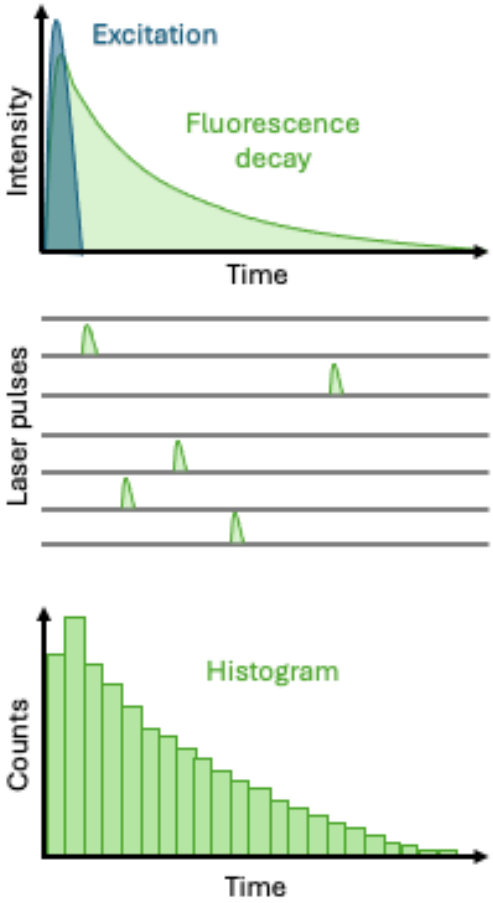

Figure 8. Principle of TCSPC: The sample is repeatedly excited, and the arrival time of multiple fluorescence photons is recorded. The recording process forms a distribution of the photons over time that represents the fluorescence decay.

The histogram is further used to convert the fluorescence decays to fluorescence lifetimes by through analyzing the time-resolved fluorescence data. The analysis involves fitting the decay curve to an exponential fluorescence decay function given by

$$I(t) = I_0 e^{-t/\tau} \tag{12}$$

where $I(t)$ is the fluorescence intensity at time t, I_0 is the intensity of the initial fluorescence at $t = 0$, t is time, and τ is the fluorescence lifetime.[17] The fluorescence lifetime is an essential parameter in fluorescence studies because it provides information about the average time a fluorophore spends in the excited state before undergoing a decay process and returning to the ground state. Fluorescence lifetime measurements are applicable in fluorescence lifetime imaging (FLIM), where the spatial distribution of fluorescence decay times in each pixel of the image is determined simultaneously. In Förster Resonance Energy Transfer (FRET) studies,

fluorescence lifetime measurements are used to study the molecular interactions and evaluate the molecular mechanisms.[37]

TCSPC consists of a pulsed laser, a detector, and a timing electronics system. The main components in timing electronics systems for signal processing are a constant-fraction discriminator (CFD), a time-to-amplitude converter (TAC), an analogue-to-digital converter (ADC), and a digital memory.[28]

A sample is excited with a pulsed laser source with a high repetition rate. The emitted individual photons are detected using a highly sensitive photodetector, usually a PMT (photomultiplier tube). When a single photon is detected, the electronic signal generated in the detector is directed into CFD, which is responsible for initiating a voltage ramp in the TAC. This eliminates the low-amplitude noise from being counted as a real signal. The second CFD is used to obtain a timing reference pulse from a light source. The output pulses of the CFD are used as start and stop pulses for the time-amplitude converter. The TAC produces an output signal proportional to the time between the start and stop pulses. The amplified TAC signal is led to ADC, where the voltage is converted into time. When a photon is detected, the ADC output indicates a memory location corresponding to the time of the photon (Figure 9).[28,37]

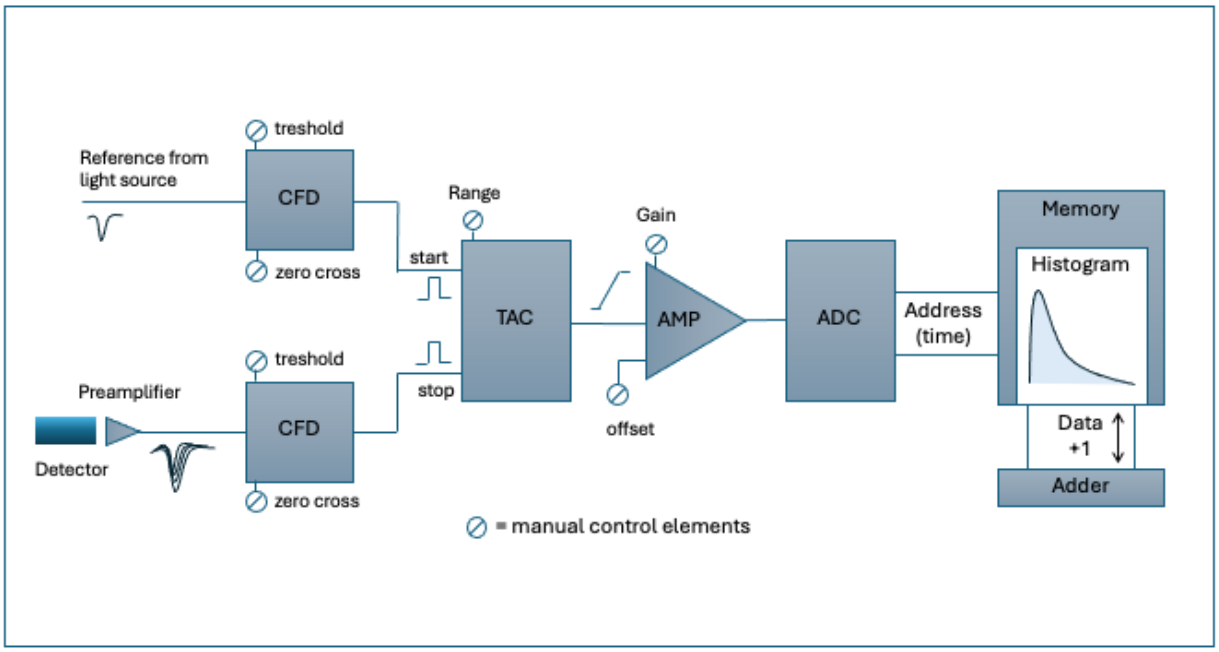

Figure 9. A classic TCSPC setup.

TCSPC has multiple outstanding features. First, TCSPC reaches a near-ideal photon efficiency, meaning the recording process has no photon loss. Every photon seen by the detector arrives in the photon distribution and contributes to the result. Second, TCSPC is a highly sensitive and accurate technique with excellent time resolution. The time resolution of TCSPC is not limited by the width of the single electron response (SER) of the detector, as in analog recording techniques. Instead, the resolution is determined by the accuracy with which the arrival times of the individual pulses can be measured. This accuracy surpasses the width of the pulses. The instrument response function (IRF) is obtained from the transit time spread (TTS) of the detector, which can be up to 10 to 50 times smaller than the single photon response of the detector. As a result, photon counting techniques provide significantly higher bandwidths and shorter IRF than detector response in analogue recording methods. With near-ideal counting efficiency and multiwavelength capability, TCSPC imaging is one of the most optimal signal recording techniques for detecting fluorescence decay functions.[28,37]

4.4 Dynamic Light Scattering (DLS)

Dynamic light scattering (DLS), also known as photon correlation spectroscopy (PCS), is a spectroscopic technique for particle size analysis in the nanometer range. In addition, DLS is a powerful technique to determine the particle size distribution and stability in solutions or suspensions. It is a non-invasive method that measures the light intensity scattered by the nanoparticles. The fluctuations in the intensity of scattered light caused by the Brownian motion of particles are analyzed. The analysis of these fluctuations gives information about the particle size.[29,38]

When particles are suspended in a liquid, they experience Brownian motion, which is a random thermally driven particle movement. Brownian motion occurs when the fluid molecules collide with particles, causing them to move in random directions. Smaller particles diffuse more rapidly and move faster than larger particles and, therefore, cause fluctuations in scattered light intensity over time. The fluctuation speed is related to the size of the particles.[29,38,39]

By measuring the speed of the Brownian motion, the translational diffusion coefficient D can be determined. Determining translational diffusion coefficient D is useful in obtaining the hydrodynamic radius, defined as the radius of a hypothetical sphere. The translational diffusion

coefficient D is related to the hydrodynamic radius R_h of the particles according to the Stokes-Einstein equation:

$$D = \frac{k_\mathrm{B}T}{6\pi\eta R_\mathrm{h}}, \tag{13}$$

where k_B is the Boltzmann constant (1.380×10^{-23} $\mathrm{kgm^2/Ks^2}$), T is an absolute temperature, and η is the viscosity of the solution.[29]

The DLS instrument setup (Figure 10) involves a laser, a sample cuvette, a detector, a correlator and a computer for data analysis. When the laser beam is directed through the sample, the incident light scatters in all directions if the particle sizes are small compared to the wavelength of the incident light. The monochromatic incident light undergoes a phenomenon called Doppler broadening, which states that the frequency of scattered light from a particle is shifted due to the particle motion. The intensity of scattered light fluctuates over time because of the Brownian motion of small particles in a suspension. The fluctuation occurs because small particles moving faster do not adopt a specific position in a solution. The scattered light will either lead to constructive or destructive interference. The destructive phases will cancel each other out, while the constructive phases will result in a detectable signal. The scattered light intensity is recorded by a detector at a certain angle as a function of time. Depending on the detection angle, the scattered light is detected as a backscattered, forward-scattered or side-scattered light. The fluctuations in the scattered light intensity are correlated by an autocorrelator to determine the rate of the intensity fluctuations. The particle size distributions are obtained from the analysis of the correlation functions using the Stokes-Einstein equation. To convert the measured diffusion coefficient into a hydrodynamic radius, the viscosity of the sample must be entered into the Stokes-Einstein equation.[29,38,39]

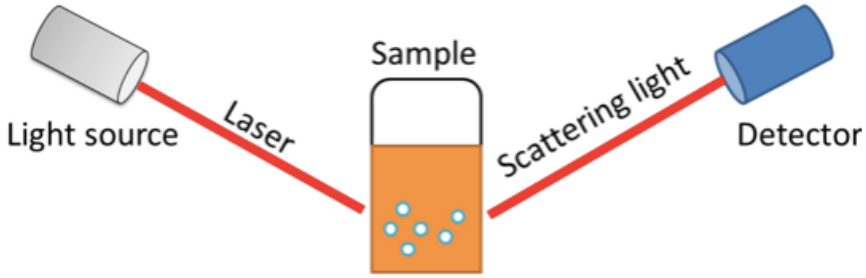

Figure 10. Operation principle of DLS.[29]

In addition to particle size distributions, other useful parameters that can be determined with DLS are the polydispersity index (PI) and the peak width. The polydispersity index measures a sample's heterogeneity based on size, with values ranging from 0 to 1. Since it is defined by the width of the size distribution curve, a smaller PI indicates a narrower size distribution and monodisperse particles. A larger PI corresponds to polydisperse particles with a broader size distribution. Polydisperse particles may occur due to agglomeration or aggregation during the nanoprecipitation or analysis. PI values smaller than 0.05 are more common to highly monodisperse particles, while PI values larger than 0.7 indicate a sample with a broad particle size distribution that is unlikely to be suitable for analysis by DLS. Peak width is another factor determining the homogeneity of the size distribution within the sample. The size distribution is narrow in a monodisperse sample, leading to a narrow peak width. In contrast, a broad peak width of the size distribution indicates the presence of polydisperse particles or aggregates in the sample. The width of the peak in DLS statistics is usually defined as the standard deviation of the peak.[29,30,40]

Although DLS is considered a significant method for particle size analyses, it has some disadvantages. DLS is most effective for particles in the nanometer size range and typically detects particle sizes from 0.3 nm to 10 µm. DLS is sensitive to the concentration of the particles. As DLS measures the scattering light, the multi-scattering and agglomeration of particles at high concentrations may lead to invalid results. The DLS measurement can be sensitive to solvent viscosity and temperature fluctuations. Therefore, the solvent's viscosity must be known, and the temperature control must be considered. In addition, DLS assumes the particles to be monodisperse and spherical. Despite these assumptions, DLS is highly suitable for studying colloidal and nanoscale systems.[29,38]

DLS is considered an essential tool during nanomaterial synthesis because it provides crucial information about the particle size distribution during the preparation of nanoparticles. Also, DLS is non-destructive, i.e., it does not damage the sample during the measurement. DLS has been widely applied in different fields, such as biochemistry and nanotechnology, to characterize the size of various particles from proteins to different nanomaterials.[29,38]

4.5 Cryo-TEM

Alongside DLS, the preferred method of imaging small nanoparticles in aqueous solution is cryo-transmission electron microscopy, cryo-TEM. Cryo-transmission electron microscopy is a type of transmission electron microscope (TEM) used to image radiative-sensitive specimens at cryogenic temperatures. It is applicable for studying the three-dimensional shape and structure of complicated biological complexes like proteins, viruses, and bacteria. By rapidly cooling the samples in a layer of glass-like ice, cryo-TEM preserves the natural structure of the specimen and reduces the radiation damage, making it ideally suitable for examining highly sensitive biological samples. With precise information on particle morphology, cryo-TEM provides an ideal way to characterize sensitive organic nanomaterials and heterogeneous nanoparticle samples.[30,31]

For the cryo-TEM measurement, the sample preparation can be performed in several ways depending on the nature of the sample. The rigorous conditions related to the high vacuum and intense radiation in cryo-TEM must be considered in the sample preparation to minimize the sample damage and reduce the electron beam damage. One of the most efficient sample preservation methods is cryo-fixation, where a small amount of sample is applied to a holey carbon grip and blotted with a filter, leaving a thin layer of solution in the holes of the grip. The grip is plunged into a liquid ethane cooled with liquid nitrogen. The rapid plunge-freezing process produces vitrified glass-like ice, preventing the formation of ice crystals that can cover and damage the sample. While the sample is kept frozen, it is imagined with an electron cryomicroscope. The cryo-fixation method is widely used to prepare samples for cryo-TEM applications such as tomography and single-particle imaging.[30,31,41]

The cryo-TEM instrument consists of an electron source, condenser lenses, specimen holder, objective lens, intermediate lens, projector lenses and image-recording system, including a camera or fluorescent screen (Figure 11). After the vitrified sample is loaded into a high-vacuum cryo-TEM instrument, an electron beam is directed to the sample. The electron beam is produced by the electron gun and focused on the sample by the condenser lenses. The high-energy electron beam passes through the sample and interacts with its atoms and molecules. These interactions lead to the generation of transmitted, scattered, and secondary electrons. The transmitted electrons are collected by a detector, and the data is used to create images on a fluorescent screen or a computer screen using a camera.[31,41]

The denser the specimen, the more electrons are scattered as they pass through the sample, forming a darker image, while fewer electrons reach the screen for imaging. For more transparent specimens, the intensity of transmitted electrons leads to a brighter appearance in the image. To create 3D images, the sample is tilted at different angles within the microscope to collect a series of (2D) projection images. These images are used to reconstruct a 3D image using tomographic reconstruction algorithms and visualized with specialized software. For 3D tomographic imaging, the samples must be thin enough to transmit the incident electron beam.[31,41]

Imaging at cryogenic temperatures reduces the radiation damage of the samples. This means that images taken at cryogenic conditions in cryo-TEM can use higher electron doses to improve the signal-to-noise ratio because the amount of radiation damage per unit of electron dose is lower.[31] Other advantages of cryo-TEM include the capability to capture dynamic processes in real-time, allowing the study of the structural changes and interactions within the sample. In addition, resolution of less than one nanometer has been achieved, enabling near-atomic resolution.[42]

Unlike the other structural analysis methods, such as X-ray crystallography and NMR spectroscopy, cryo-TEM does not require crystals. However, in cryo-TEM, the data collection is still slower than in X-ray crystallography, and the minimum molecular weight limit of sample particles has been reported to be 52 kDa with 3.2 Å resolution.[43] Therefore, cryo-TEM is suitable for studying larger complexes than X-ray crystallography and NMR spectroscopy,.[42]

Although continuous improvement in resolution, cryo-TEM currently achieves resolutions of around 3 Å and, in some cases, even below 3 Å. Nevertheless, challenges remain in achieving

atomic resolution, primarily due to low signal-to-noise ratio and poor contrast, which are the main challenges of cryo-TEM.[42] By integrating the established structure determination techniques of X-ray crystallography and NMR spectroscopy with cryo-TEM, it is possible to generate atomic-resolution models of complex assemblies.[31,42] Despite some of its limitations, cryo-TEM is an attractive technique for the visualization of the sample in its most native functional state and for obtaining relevant high resolution in nanoparticle imaging.[41]

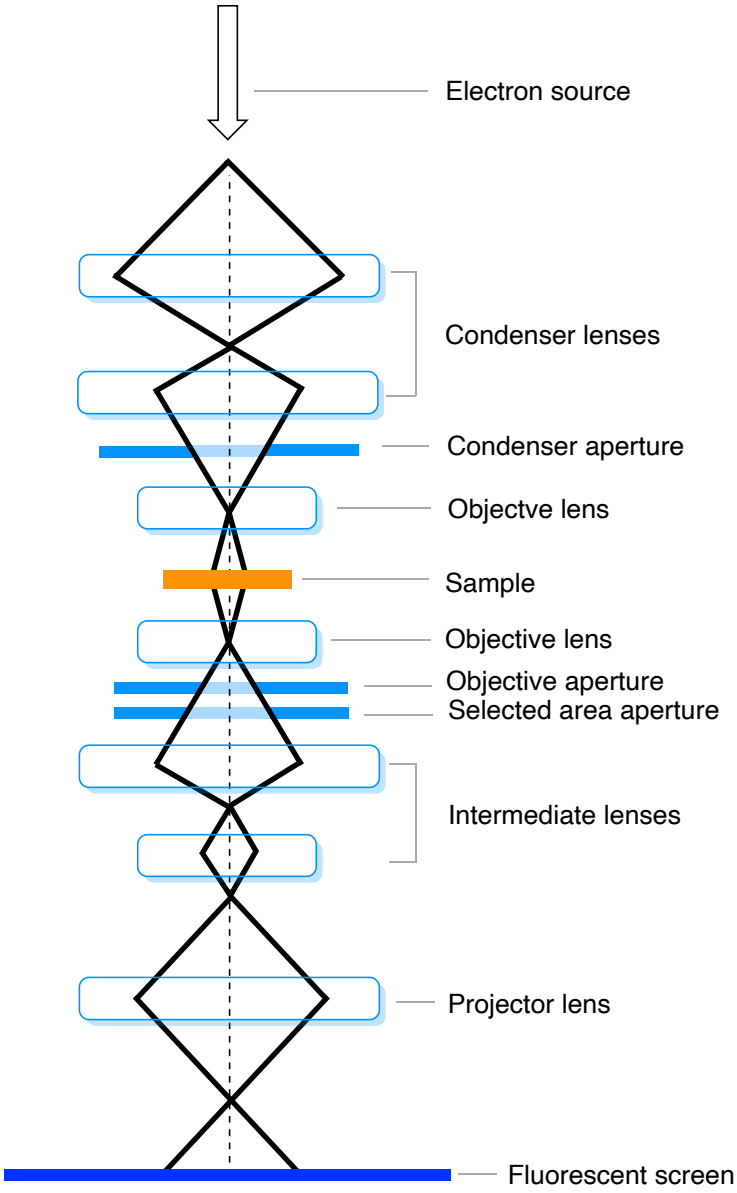

Figure 11. Schematic illustration image of TEM.

5 Fluorescent properties of SMILES nanoparticles

SMILES materials have shown significant fluorescent properties in recent studies. DSPE-PEG (11 wt %) coated rhodamine R12 SMILES NPs with 2.5 molar equivalent of cyanostar displayed ultrabright emission and high quantum yield.[13] The fluorescence quantum yield was 30 %, the brightness per volume (*B/V*) of over 5000 M^{-1} cm^{-1}/nm^3 when excited in the main rhodamine absorption peak at 560 nm and molar absorption coefficient 4×10^7 M^{-1} cm^{-1} for the SMILES nanoparticles.[13]

When exciting the SMILES NPs in the UV region, the brightness (*B/V*) reached 6600 $M^{-1}cm^{-1}/nm^3$.[13] In this region, the absorption of R12 dye is insignificant, but because cyanostar has a large molar absorption in the 300-350 nm range, the energy absorbed in the UV region by the cyanostar can be funneled to the dye molecule. This leads to a significant increase in the brightness of the SMILES NPs. These brightnesses are the highest ever reported for dye-based organic fluorescent nanoparticles. The very high brightness of SMILES indicates that it is possible to produce ultra-bright nanoparticles.[5,13]

5.1 Energy transfer

Flood, Laursen and coworkers[23] studied energy transfer from cyanostar to rhodamine (R12) and cyanine ($DiOC_6$) dye molecules in SMILES NPs. The energy transfer efficiency increased from 83 % in R12 SMILES NPs to 100 % in cyanine SMILES NPs due to the increased spectral overlap. The emission brightness of both nanoparticles approximately doubled when the cyanostar of the SMILES NPs was excited with UV light harvesting. This UV antenna system constituted by cyanostar increases the brightness due to the effective energy transfer from cyanostar to the dye and the high molar absorption coefficient of cyanostar in the UV region. The efficient UV light energy harvesting arises from the high energy transfer rates between the cyanostar and the dye molecule. The energy transfer rate is proportional to the spectral overlap integral between the donor (cyanostar) emission and acceptor (dye molecule) absorption spectra. The increased energy transfer and UV light harvesting efficiency in SMILES provide a future approach to engineering functional ultrabright nanomaterials with UV light harvesting processes.[13,23]

The efficiency of energy transfer can be determined by the excitation spectrum of the acceptor. The excitation intensity of the energy acceptor at a specific wavelength can be expressed by the absorbance of the energy acceptor A_{A} and energy donor A_{D}, respectively as shown below.[44]

$$I = A_{\mathrm{A}} + \phi_{\mathrm{ET}} A_{\mathrm{D}} \tag{14}$$

Without energy transfer, the excitation spectrum is the same as the absorption spectrum of the energy acceptor. When the efficiency of energy transfer, ϕ_{ET} is 100%, all the energy the donor absorbs is completely transferred to the acceptor. As a result, the excitation spectrum of the acceptor is equal to the sum of the absorption spectra of the acceptor and donor.[23,44]

Since the acceptors used in SMILES structures do not show any absorbance at the absorption band of the donor (cyanostar) at 320 nm, the energy transfer efficiency can be calculated from the intensity ratio of the NPs absorption and excitation spectra. For this, the two spectra must be normalized to the $S_0 \rightarrow S_1$ absorption bands of the respective dye. The normalization of absorption and excitation spectra ensures that the spectra are directly comparable and specific to the absorption characteristics of the component involved in the energy transfer process. The excitation energy transfer efficiency Φ_{EET} can be obtained as presented below.[23]

$$\Phi_{\mathrm{EET}} = \frac{\mathrm{Normalized\ excitation}_{320\ \mathrm{nm}}}{\mathrm{Normalized\ absorption}_{320\ \mathrm{nm}}} \times 100\% \tag{15}$$

The previous studies of Flood, Laursen et al.[23] indicate that the energy transfer mechanism in SMILES NPs is dominantly caused by the Förster Resonance Energy Transfer (FRET). FRET is a mechanism that describes the energy transfer process between two light-sensitive molecules. FRET occurs when the donor and acceptor fluorophores are in close proximity (10-100 Å). A donor molecule in the excited state transfers the energy to an acceptor molecule in the ground state through a non-radiative process and promotes the acceptor to its excited state (Figure 12).[17,45]

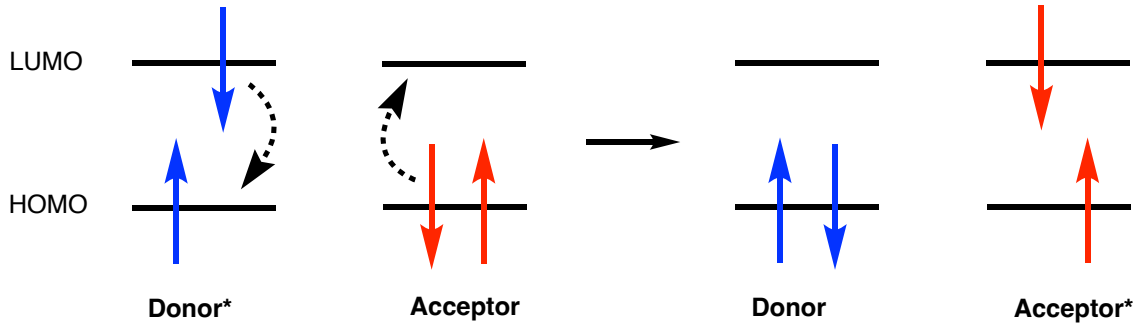

Figure 12. Schematic diagram of Förster resonance energy transfer.

This type of energy transfer occurs when the emission spectrum of the donor molecule and the absorption spectrum of the acceptor molecule overlap. The energy transfer results from dipole-dipole interactions between the donor and acceptor, and it does not include the appearance of a photon. The energy transfer rate depends on the spectral overlap of the donor emission spectrum with the acceptor absorption spectrum, the quantum yield and the donor's lifetime, the relative orientation of the transition dipole moments of the donor and acceptor and the distance between the donor and the acceptor.[17]

The energy transfer rate for a donor and acceptor separated by a distance r is given by

$$k_{\mathrm{T}}(r) = \frac{\phi_{\mathrm{D}}\kappa^2}{\tau_{\mathrm{D}} r^6}\left(\frac{9000(\ln 10)}{128\pi^5 N_{\mathrm{A}} n^4}\right)\int_0^\infty F_{\mathrm{D}}(\lambda)\varepsilon_{\mathrm{A}}(\lambda)\,\lambda^4\,d\lambda, \qquad (16)$$

where ϕ is the quantum yield of the donor in the absence of the acceptor, τ_{D} is the lifetime of the donor in the absence of the acceptor, κ^2 is the transition dipole orientation factor, N_{A} is the Avogadro's number, and n is the refractive index of the medium. The integral corresponds to the spectral overlap integral, denoted as $J(\lambda)$. It expresses the degree of the spectral overlap between the donor emission and acceptor absorption as follows:

$$J(\lambda) = \int_0^\infty F_{\mathrm{D}}(\lambda)\varepsilon_{\mathrm{A}}(\lambda)\,\lambda^4\,d\lambda = \frac{\int_0^\infty F_{\mathrm{D}}(\lambda)\varepsilon_{\mathrm{A}}(\lambda)\lambda^4 d\lambda}{\int_0^\infty F_{\mathrm{D}}(\lambda)d\lambda} \qquad (17)$$

where $F_{\mathrm{D}}(\lambda)$ is the fluorescence intensity of the donor normalized to unity and $\varepsilon_{\mathrm{A}}(\lambda)$ is the molar absorption coefficient of the donor at a specific wavelength in units $\mathrm{M}^{-1}\mathrm{cm}^{-1}$.[17]

The efficiency of the energy transfer E indicates the fraction of photons absorbed by the donor transferred to the acceptor. The fraction is expressed as

$$E = \frac{k_{\mathrm{T}}(r)}{\tau_D^{-1} + k_T(r)}, \tag{18}$$

which corresponds to the ratio of the energy transfer rate $k_{\mathrm{T}}(r)$ to the total decay rate of the donor in the presence of the acceptor.[17]

Alongside FRET, another possible energy transfer mechanism in SMILES NPs to be considered is the Dexter energy transfer process, also known as Dexter electron exchange. In Dexter energy transfer, an electron from the excited donor molecule is transferred to an acceptor molecule through a non-radiative process. Electron exchange occurs from the S_1 state of the donor to the S_1 state of the acceptor simultaneously with an electron exchange from S_0 of an acceptor to S_0 of a donor (Figure 13). Unlike FRET, Dexter does not involve dipole-dipole interactions but a strong wavefunction overlap between donor and acceptor. Therefore, Dexter energy transfer is more effective over shorter distances (typically < 10 Å) compared to FRET.[17,45]

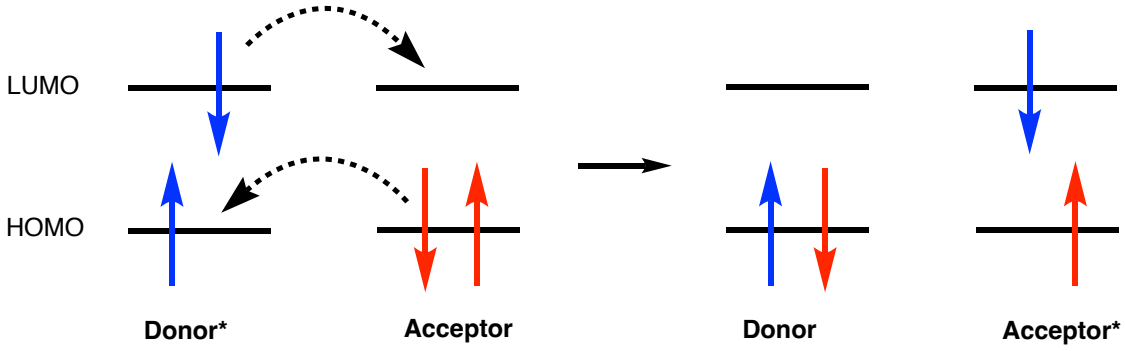

Figure 13. Schematic diagram of Dexter energy transfer.

5.2 Energy migration to trap states

The energy migration plays a crucial role in dye-based nanoparticles because although it does not directly affect the photophysical properties of the nanoparticles, it often leads to fluorescence quenching. In nanoparticles with high dye density, the energy is migrated between the dye molecules. For this process to occur, close dye-dye distances and the spectral overlap

between chromophore absorption and emission are necessary. Due to energy migration, the excited state (exciton) migrates within the nanoparticles until it is deactivated either radiatively or non-radiatively.[46]

However, nanoparticles containing a single dye type often have trap states originating from impurities or nanoparticle formation process. Consequently, efficient energy migration can lead to the migration of the formed exciton to these lower-energy trap states (Figure 14). If the exciton becomes trapped in the dark trap states, it undergoes non-radiative deactivation, resulting in the quenching of nanoparticle emission. Therefore, energy migration significantly influences aggregation-caused quenching (ACQ).[47]

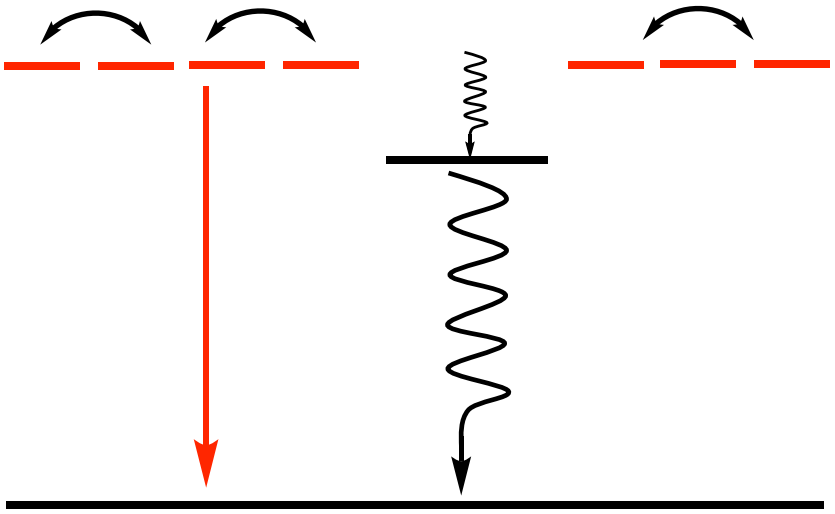

Figure 14. Quenching of fluorescence by energy migration to trap states.

EXPERIMENTAL PART

6 Aim of the study

The aim of this experimental part was to investigate the energy transfer process from cyanostar anion complexes in SMILES nanoparticle to dyes. The optical properties and size of SMILES nanoparticles consisting of cyanostar and optically active dyes as well as cyanostar and optically inactive cations were studied, and the dominant energy transfer mechanism was determined. The study of SMILES nanoparticles was based on previous research by Flood, Laursen and coworkers[13] which focused on optically active SMILES. However, the study of optically inactive cations in SMILES nanoparticles presents the primary intriguing aspect of the research, especially considering the absence of previous studies on this topic.

Given the versatility of utilizing any commercially available cationic dyes in the preparation of SMILES NPs, the investigation expanded beyond the previously explored rhodamine-based SMILES nanoparticles. Thus, in addition to rhodamine (R12), 4,8-dioctyl-propyl-4,8-diaza-12-oxatriangulenium (DAOTA **6**) (Figure 15) was selected as a dye for SMILES nanoparticles. This choice was motivated by the lack of prior research on DAOTA within the context of SMILES nanoparticles. Also, the very different molar absorption coefficients of R12 and DAOTA are crucial when assessing their energy transfer mechanism.

SMILES nanoparticles including cyanostar and rhodamine or DAOTA as dye molecule as PF_6^- salts were prepared. Similarly, SMILES nanoparticles with imidazolium (IMZ **7**) and tetrabutylammonium (TBA **8**) as PF_6^- salts (Figure 15) were prepared to study the fluorescent properties of the cyanostar anion complex and to investigate the energy transfer process from the cyanostar anion complex to R12 and DAOTA dye molecules. The SMILES nanoparticles were characterized using absorption and fluorescence spectroscopy, dynamic light scattering and cryo-TEM.

DAOTA is an organic dye that belongs to the class of triangulenium dyes. Triangulenium dyes constitute a group of organic dyes characterized by their planar, fully conjugated triangulenium core. Specifically, diazaoxatriangulenium (DAOTA) is part of notable cationic azaoxa-triangulenium dyes. Due to its strong absorption and attractive fluorescent properties, it has been widely used as a fluorescent probe in various fluorescence-based technologies,

particularly in fluorescence microscopy and bioimaging applications.[48–50] The molar absorption coefficient, ε, for DAOTA used in this study is 15 000 $M^{-1}cm^{-1}$.[48]

IMZ and TBA are organic cations that do not have absorption or emission in the visible region. Instead, they absorb at lower wavelengths and higher energy. Their cationic nature and distinct absorption properties, differing from those of cyanostar, make them suitable for the characterization of cyanostar anion complex ($CS_2PF_6^-$) in SMILES nanoparticles. For the study of cyanostar anion complex in IMZ and TBA SMILES nanoparticles, the cyanostar's molar absorption coefficient of 120 000 $M^{-1}cm^{-1}$ was utilized.[13]

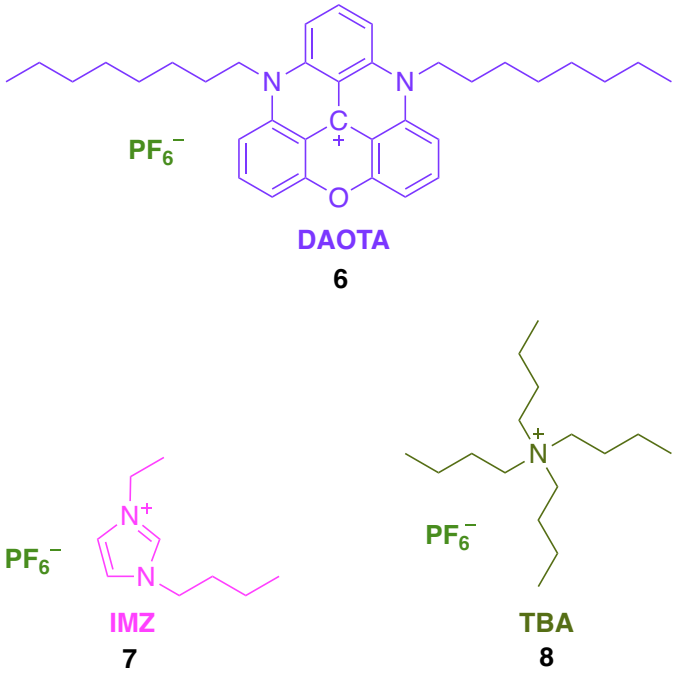

Figure 15. The structure of DAOTA **6,** IMZ **7** and TBA **8** as a salt of PF_6^-.

7 Materials and methods

Cyanostar and the fluorescent dyes rhodamine R12 **1** and DAOTA **6** used in the experimental part were previously synthesized at the University of Copenhagen by Bo Wegge Laursen's group.[13,23] Rhodamine R12 was obtained by modifying the rhodamine B with a lipophilic carbon chain using a method reported by Klymchenko and coworkers.[51] DAOTA **6** was obtained by modifying the DAOTA structure with octane chains based on previous

procedures.[50] R12, DAOTA, IMZ and TBA cations were obtained and used of as PF_6^- salts. 1,2-distearoyl-sn-glycero-3-phosphoethanolamine-polyethylene glycol (DSPE-PEG **5**) was purchased from Biochempeg. Milli-Q water (18.2 MΩ) was obtained using a Millipore purification system.

All the other chemicals used in this study are listed in Table 1. All the chemicals were used as received without any further purification.

Table 1. Chemicals used in the experimental part.

Chemical	Manufacturer	Purity %
Tetrahydrofuran (THF)	VWR	≥ 99.7
1-Butyl-3-ethylimidazolium hexafluorophosphate (IMZ)	abcr	98
Tetra-n-butylammonium hexafluorophosphate (TBA)	Alfa Aesar	98
Dichloromethane (DCM)	VWR	≥ 99.8

Ohaus Explorer scale from Buch Holm was used to weigh the reagents, and EMAG Ultrasonic cleaner Emmi- 30 HC was used for sonication.

The Dynamic Light Scattering (DLS) Zetasizer Ultra from Malvern was used for particle size measurements. A 3500 µl synthetic quartz glass cuvette from Thorlabs with a path length of 10.00 mm was used for all the DLS measurements. ZS Xplorere software from Malvern Panalytical was used to analyse the DLS data.

The cryo-TEM images were recorded with a FEI Tecnai G2 20 TWIN 200 kV transmission electron microscope. The samples were prepared using an on-site cryo-sample preparation instrument, a FEI Vitrobot Mark VI, based on vitrification (rapid cooling) of aqueous samples in liquid ethene to reduce the possibility of ice crystal formation. The samples were transferred in liquid nitrogen to a Tecnai G2 TEM for imaging.

The absorption spectra were measured using the Lambda 1050 Uv-Vis-NIR spectrophotometer from Perkin Elmer. The emission and excitation spectra were recorded on a FluoTime 300 spectrometer fitted with a cw-xenon lamp from PicoQuant. Fluorescence decays were recorded

with FluoTime 300 fitted with pulse diode lasers 300 nm or 560 nm. A high-performance quartz cuvette from Hellma Analytics was used for all the spectroscopic measurements.

8 Preparation of SMILES

SMILES nanoparticles were prepared in two otherwise similar ways, but in the second preparation process, the NP precursor solutions were injected into water more aggressively to form the nanoparticles faster. The fast injection was expected to reduce the particle size.

8.1 Preparation of SMILES nanoparticles 1.0

SMILES nanoparticles with 100% dye or optically inactive cation were prepared. The stock solutions of R12 (1 mM), DAOTA (1 mM), IMZ (1 mM), TBA (1 mM), CS (2 mM) and DSPE-PEG (4mg/ml) were prepared in THF. The weighted masses and the required volumes of THF for the stock solutions are presented in Table 2.

Table 2. Weighted masses and calculated volumes of reagents for NPs 1.0 stock solutions.

Reagent	Mass (mg)	THF Volume (µl)
R12	0.29	383
DAOTA	0.61	935
IMZ	7.63	35 815
TBA	0.53	1367
CS	1.09	595
DSPE-PEG	4.19	1048

The precursor solutions (500 µl) were prepared using 100 µl of either R12 (1mM), DAOTA (1mM), IMZ (1mM) or TBA (1 mM), 2.5 molar equivalent (125 µl) of cyanostar (2 mM) and 66 wt% of DSPE-PEG. The weight percentage (wt%) of DSPE-PEG was calculated from the mass of the dye (or inactive cation). The weight percentage (wt%) of DSPE-PEG was controlled by varying the amount of DSPE-PEG stock solution. THF was added to each precursor solution to obtain a total volume of 500 µl (Table 3.).

Table 3. Precursor solutions of NPs 1.0.

	Cation (µl)	CS (µl)	DSPE-PEG (µl)	THF (µl)
R12	100	125	150	125
DAOTA	100	125	150	125
IMZ	100	125	125	150
TBA	100	125	130	145

0.5 ml of each precursor solution was injected alternately into 10 ml of Milli-Q water under 5 minutes of sonication. Vials containing the pink or transparent SMILES NPs in aqueous solutions (Figure 16) were left open in the fume hood to let the THF evaporate. The SMILES NPs were used as prepared for further characterization.

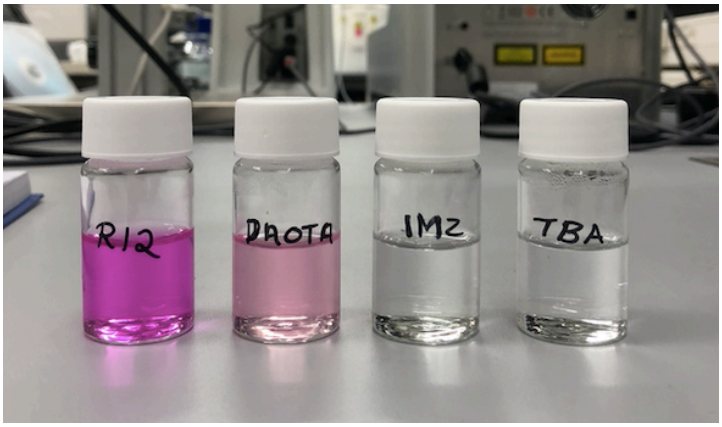

Figure 16. Synthesized R12, DAOTA, IMZ and TBA SMILES nanoparticles 1.0 in aqueous solution.

8.2 Preparation of SMILES nanoparticles 2.0

The SMILES nanoparticles with 100% dye or optically inactive cation were prepared as described earlier (Chapter 7.1), except that precursor solutions were prepared in double (1 ml), half of which was used for nanoprecipitation and half for the further characterization of dyes (Chapter 1.2). The weighted masses and the required volumes of THF for the stock solutions are presented in Table 4.

Table 4. Weighted masses and calculated volumes of reagents for NPs 2.0 stock solutions.

Reagent	Mass (mg)	THF Volume (l)
R12	0.45	595
DAOTA	0.31	475
IMZ	2.93	13 753
TBA	0.32	826
CS	2.20	1200.6
DSPE-PEG	4.47	1175

The precursor solutions (1 ml) were prepared using 200 µl of either R12 (1mM), DAOTA (1mM), IMZ (1mM) or TBA (1 mM), 2.5 molar equivalent (250 µl) of cyanostar (2 mM) and 66 wt% of DSPE-PEG. The weight percentage (wt%) of DSPE-PEG was controlled by varying the amount of DSPE-PEG stock solution. THF was added to each precursor solution to obtain a total volume of 1 ml (Table 5.).

Table 5. Precursor solutions of NPs 2.0.

	Cation (µl)	CS (µl)	DSPE-PEG (µl)	THF (µl)
R12	200	250	300	250
DAOTA	200	250	300	250
IMZ	200	250	250	300
TBA	200	250	260	290

The nanoprecipitation was performed similarly to the first nanoprecipitation (Chapter 8.1), but the injection of precursor solutions (1 ml) into 10 ml of Milli-Q water was done faster and more aggressively to mix the precursor solutions more rapidly with water. Nanoprecipitation resulted in pink and transparent SMILES nanoparticle solutions as before (Figure 17).

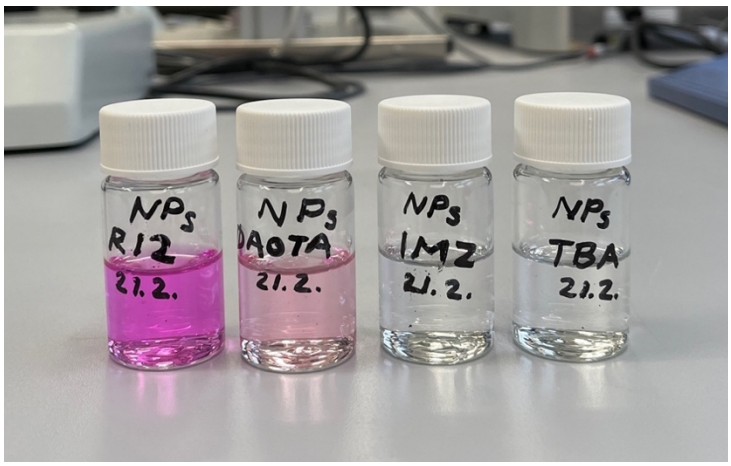

Figure 17. Synthesized R12, DAOTA, IMZ and TBA SMILES nanoparticles 2.0 in aqueous solution.

9 DLS measurements of SMILES nanoparticles

For particle size measurements, the nanoparticle solutions were filtered through a hydrophilic PTFE filter (0.22 µm) to reduce the contribution from dust. As a reference for 1.0 NPs, nanoparticle solutions without filtering were measured. For 2.0 nanoparticles, only filtered samples were measured. The experimental parameters for DLS measurements are presented in Table 6.

Table 6. Parameters for DLS particle size measurements.

Parameter	Value
Temperature	25 ℃
Equilibrium time	120 s
Wavelength of laser	633 nm
Cuvette	Glass PCS1115
Refractive index of the material	1.59
Dispersant	Water
Beam angle	Backscatter

The SMILES nanoparticles were measured by performing five parallel measurements for each sample and taking the average of the measurements. The results from the DLS particle size measurements of nanoparticles 1.0 and 2.0 are presented in Table 7.

Table 7. The DLS results from the particle size measurements of filtered nanoparticle 1.0 solutions.

NPs 1.0 filtered	**Size (nm)**	**Width (nm)**	**PI**
R12	61.8	17.0	0.1
DAOTA	28.6	9.6	0.3
IMZ	19.2	6.1	0.2
TBA	37.6	11.3	0.2
NPs 1.0 unfiltered			
R12	63.8	17.9	0.2
DAOTA	105.1	44.1	0.2
IMZ	14.1	4.4	0.3
TBA	40.7	12.1	0.3
NPs 2.0 filtered			
R12	14.8	4.5	0.3
DAOTA	20.0	5.7	0.3
IMZ	5.0	1.5	0.3
TBA	5.8	1.7	0.3

The particle size measurements revealed that the SMILES nanoparticles 1.0 (Table 7) were larger than expected. R12 SMILES NPs particle size (61.8 nm) was nearly four times larger than that of previously reported for DSPE-PEG capped R12 nanoparticles (16 ± 3 nm)[13] and (18 ± 2 nm)[23] measured by DLS.

Also, the sizes of DAOTA (28.6 nm), IMZ (19.2 nm) and TBA (40.7 nm) NPs were larger than predicted. The particle size of IMZ NPs was remarkably larger than previously prepared IMZ NPs with a particle size of 7.7 nm.[52] DAOTA and TBA nanoparticles have not been prepared before, hence no published particle size data is available.

The particle size for the unfiltered DAOTA nanoparticle 1.0 solution was significantly larger (105.1 nm) than for the corresponding filtered solution (28.6 nm; Table 7). This might indicate

larger nanoparticles or aggregates in the DAOTA nanoparticle solution. For the other 1.0 nanoparticles, filtration was not considered to have a significant effect.

The DLS measurements showed significantly smaller nanoparticles from the second nanoprecipitation (Table 7) than from the first nanoprecipitation. The R12 NPs hydrodynamic size (14.8 nm) was closer to previously reported sizes (16 ± 3 nm and 18 ± 2).[13,23]

The hydrodynamic sizes of R12 and DAOTA NPs from the second nanoprecipitation were also closer to each other in size. The IMZ and TBA NPs sizes (5.0 nm and 5.8 nm) were considerably similar, and IMZ NPs particle size was slightly smaller than previously obtained (7.7 nm)[52]. Not only the particle size but also the width of the peak decreased in NPs 2.0. This corresponds to more homogenous nanoparticles than those prepared with the first method. However, since the polydispersity index (PI) values for filtered nanoparticles were 0.1–0.3 for both nanoparticle batches, they are mainly monodisperse.

Based on these two nanoprecipitation methods, it can be concluded that the injection rate of the precursor solution can significantly influence the size of the resulting nanoparticles. One possible explanation could be that with slow injection, the precursor solution accumulates first on the top of the vial, leading to further growth of the nanoparticles already formed. Since the particles have more time to grow, slow injection results in larger particles. In faster injection, the precursor solution is added to water at once, diluting the solutions very quickly and producing smaller particles. Thus, it seems that the nucleation size of the nanoparticles is smaller with faster nucleation. Previous examples of the effect of nucleation on nanoparticle size have indeed been described. In a study by Reisch and Klymchenko[5] on fluorescent polymer NPs, the inhomogeneous nucleation of nanoparticles led to an increase in particle size.

10 Cryo-TEM

Cryo-TEM was used for more accurate particle size characterization and visualization of nanoparticle morphology. Because Cryo-TEM images from R12 SMILES nanoparticles have been presented in the previous studies by Flood, Laursen and coworkers,[13] only DAOTA, IMZ and TBA SMILES nanoparticles were imaged.

For Cryo-TEM measurements, the nanoparticles were concentrated to enhance their visibility in the microscopy images. DAOTA, IMZ and TBA nanoparticle solutions were upconcentrated 40-fold by centrifuging 4 ml of each solution for 30 min to obtain a volume of 100 µl. The samples were deposited on a TEM grid and cooled to cryogenic temperatures using the cryo-fixation technique described above (Chapter 4.5).

DAOTA, IMZ and TBA SMILES nanoparticles were measured manually using FIJI ImageJ to show the nanoparticle sizes comparable to the hydrodynamic sizes obtained from DLS measurements. Gaussian function was fitted to the particle size distribution histograms to obtain the mean of the particle size, µ and the standard deviation of the mean, σ. The cryo-TEM images of DAOTA, IMZ and TBA NPs are presented in Appendices 1–3.

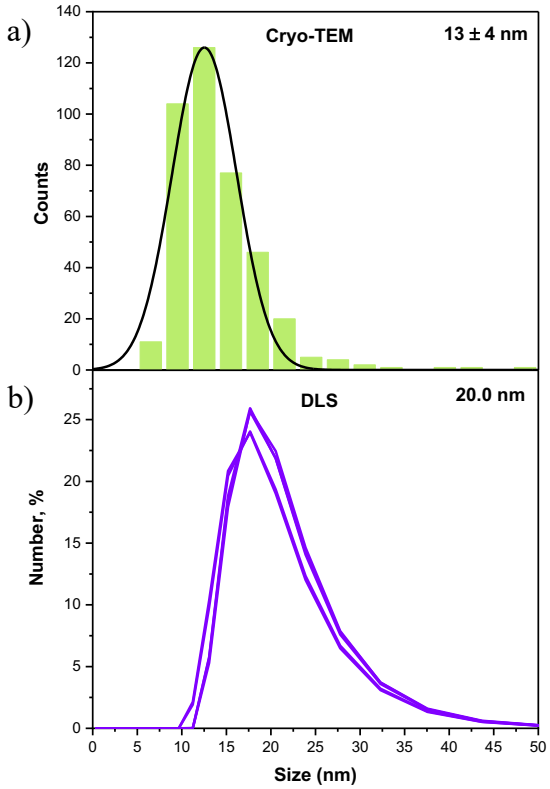

Figure 18. a) The size distribution histogram of 399 manually measured DAOTA SMILES NPs from cryo-TEM, where the Gaussian fit is presented as a black curve and b) the size distribution graphs from DLS.

The mean of DAOTA NPs particle size, µ, from cryo-TEM was 13 nm, and the standard deviation, σ was 4 nm, indicating a smaller particle size than the corresponding DLS hydrodynamic size (20 nm) (Figure 18). The smaller particle size of DAOTA NPs from cryo-TEM compared to the hydrodynamic size from DLS may be caused by the invisibility of the

DSPE-PEG capping agent in cryo-TEM images. In addition, DLS measures the hydrodynamic diameter of the particles in solution, while cryo-TEM provides detailed, high-resolution images of the particles themselves excluding the solvent. Therefore, these two techniques may give slightly different results.

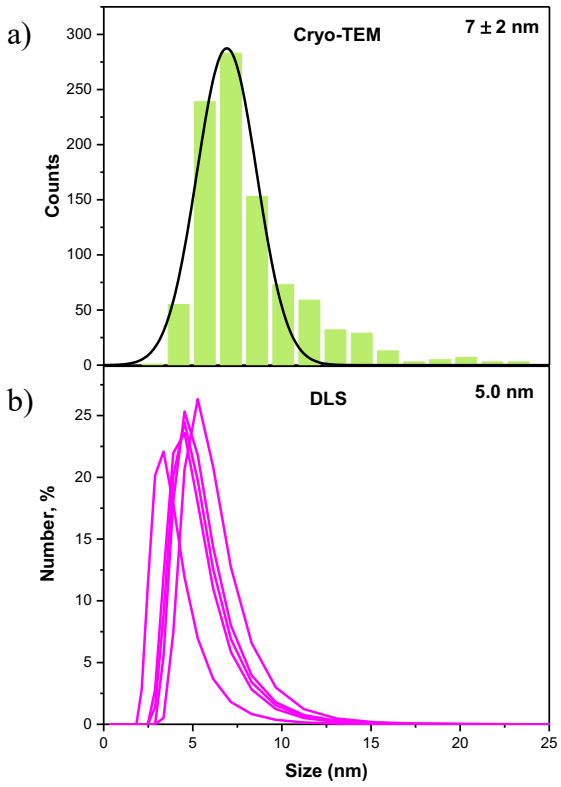

Figure 19. a) The size distribution histogram of 958 manually measured IMZ SMILES NPs from cryo-TEM, where the Gaussian fit is presented as a black curve and b) the size distribution graphs from DLS b).

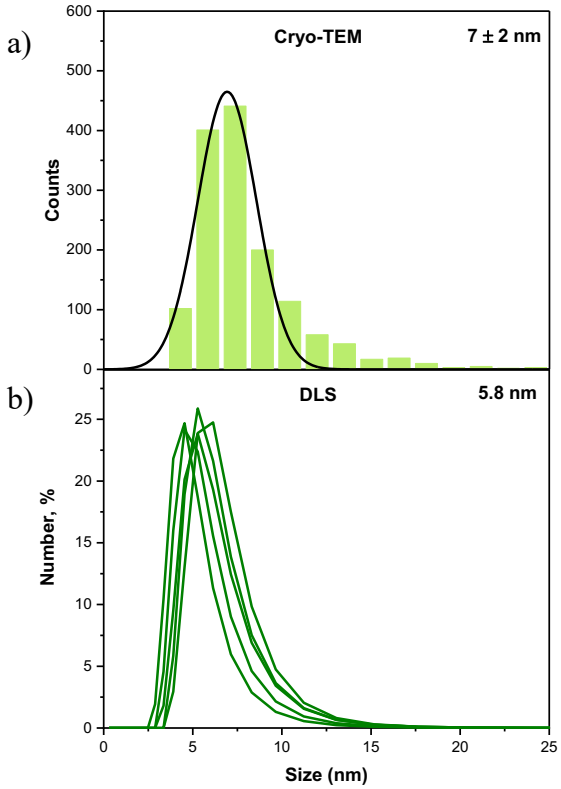

Figure 20. a) The size distribution histogram of 1420 manually measured TBA SMILES NPs from cryo-TEM, where the Gaussian fit is presented as a black curve and b) the size distribution graphs from DLS b).

IMZ and TBA nanoparticles had similar particle sizes based on cryo-TEM, with the mean particle size (μ) of 7 nm and the standard deviation, σ, of 2 nm for both nanoparticles (Figures 19 and 20). The cryo-TEM results are not fully comparable with the hydrodynamic sizes of 5 nm for IMZ NPs and 5.8 nm for TBA NPs obtained from DLS due to the distinct nature of what each techniques measure.

Overall, the sizes obtained from cryo-TEM are consistent with those from DLS measurements, indicating that the nanoparticle sizes achieved can be considered reliable. Similarly to the DLS results, the cryo-TEM results of 2.0 nanoparticles show a smaller nanoparticle size compared to 1.0 nanoparticle sizes obtained from DLS. This outcome confirms the effect of rapid injection of the nanoparticle solution on the size of the formed nanoparticles, as discussed in Chapter 9.

11 UV-Vis spectroscopy

11.1 R12 and DAOTA stock solutions

The absorption spectra of R12 and DAOTA stock solutions were measured in DCM instead of THF due to a broadened background absorption spectrum of THF. For that reason, new R12 and DAOTA stock solutions were prepared in DCM. The weighted masses and the required volumes of DCM for the stock solutions are presented in Table 8.

Table 8. Weighted masses and calculated volumes of reagents for R12 and DAOTA stock solutions in DCM.

Reagent	Mass (mg)	DCM Volume (µl)
R12	0.65	858.8
DAOTA	0.58	888.6

The samples for UV-Vis spectroscopy were prepared separately by diluting 2.5 µl of R12 stock solution and 4 µl of DAOTA stock solution in 3 ml of DCM. The background was measured with DCM. The absorption spectra with raw values are presented in Appendix 4. The absorption spectra were normalized to $S_0 \rightarrow S_1$ absorption bands of the dyes (Figure 21).

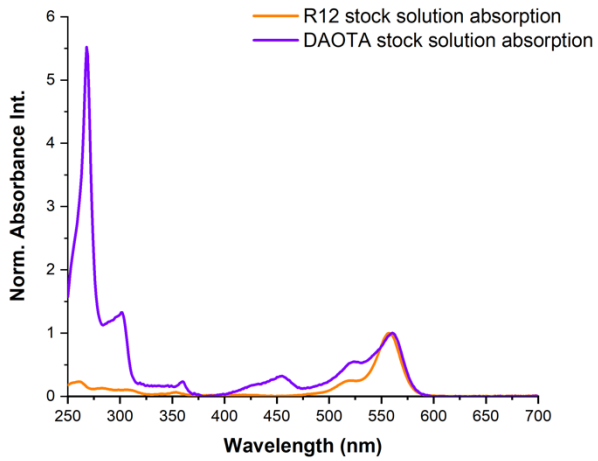

Figure 21. Normalized absorption spectra of R12 and DAOTA dyes in DCM.

Figure 21. illustrates the transition from the ground state (S_0) to the excited state (S_1) with the maximum absorption wavelength of R12 dye observed at 557 nm. This corresponds to the previously observed main rhodamine absorption peak at 560 nm.[13] Respectively, DAOTA exhibits maximum absorbance intensity for the same transition at 561 nm coinciding with the

previously reported,[48] while other absorption peaks arise from higher transitions.[49,50] The obtained absorption spectra of dye molecules were later used as a reference for the characterization of the absorption spectra of R12 and DAOTA NPs.

11.2 R12 and DAOTA SMILES nanoparticle precursor solutions

To ensure a cyanostar molar equivalent of around 2.5 in the precursor solutions, the absorption spectra of R12 and DAOTA precursor solutions (for 2.0 nanoparticles, Chapter 8.2) were measured in THF. The concentrations of the samples were kept low enough to have an absorbance below 3.0 over the whole range of excitation wavelength applied (250 nm – 700 nm) to obtain reliable results. The samples were prepared by diluting 100 µl of dye precursor solution in 3 ml of Milli-Q water. THF was used for background measurement.

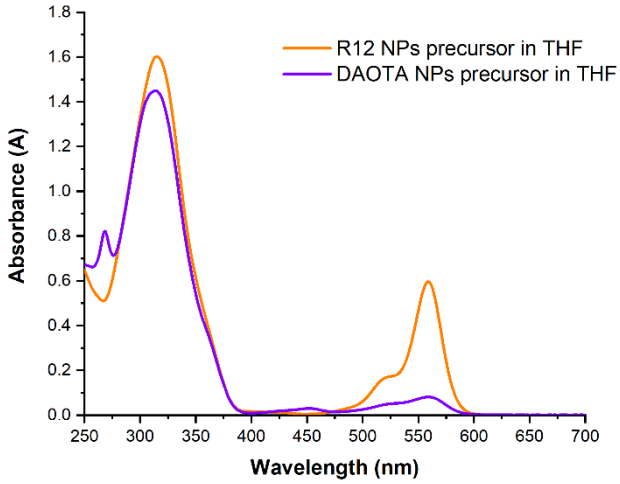

Figure 22. The absorption spectra of R12 and DAOTA SMILES nanoparticle precursor solutions in THF.

The maximum absorbance intensities for R12 and DAOTA NPs were determined to be at 315 nm and 314 nm, corresponding to the absorption of cyanostar (Figure 22). Accordingly, the maximum absorbance intensities at the dye's band were obtained at 559 nm for both precursor solutions.

Since the molar absorption coefficients of R12 and cyanostar are equal (120 000 $M^{-1}cm^{-1}$), the molar equivalent of cyanostar in R12 precursor solution was determined from the maximum absorbance intensity ratio of cyanostar (at 315 nm) and dye molecule (at 559 nm) as follows:

$$\frac{A_{315\,nm}}{A_{559\,nm}} = \frac{1.60349}{0.5968} = 2.6868 \approx 2.69 \text{ molar eq.}$$

The molar equivalent of cyanostar in DAOTA precursor solution was determined from the maximum absorbance intensity ratio of cyanostar (at 314 nm) and dye molecule (at 559 nm) taking into account the molar absorption coefficient ratio of cyanostar and DAOTA.

$$\frac{A_{314\,nm}}{A_{559\,nm}} \times \frac{\varepsilon_{DAOTA}}{\varepsilon_{CS}} = \frac{1.44956}{0.08114} \times \frac{15\,000\ M^{-1}cm^{-1}}{120\,000\ M^{-1}cm^{-1}} = 2.2331 \approx 2.23 \text{ molar eq.}$$

A slight excess of cyanostar in the R12 precursor solution reduces the dye's density and can impact the brightness per volume (*B/V*) of the NPs. While the smaller molar equivalent of cyanostar in DAOTA precursor solution leads to a decrease of fluorescence quantum yield (ϕ) and brightness of the NPs. Yet, the molar equivalents of cyanostar in R12 and DAOTA precursor solutions were sufficiently close to the desired 2.5 molar equivalents to obtain the adequate optimal brightness in the nanoparticles.[13]

11.3 Absorption of SMILES nanoparticles

The absorption spectra of prepared R12, DAOTA, IMZ and TBA SMILES nanoparticles were measured in aqueous solution. To avoid inner filter effects, the concentrations of the samples were kept low enough to have an absorbance below 0.1 over the whole range of excitation wavelength applied (250 nm – 700 nm). Milli-Q water was used for background measurement.

11.3.1 R12 and DAOTA SMILES nanoparticles

The samples were prepared separately by diluting 125 µl of R12 NPs solution and 150 µl of DAOTA NPs solution in 3 ml of Milli-Q water. The spectra with raw values are presented in Appendix 5. The resulting absorption spectra were normalized to the dye's absorption band and

plotted together with earlier obtained R12 and DAOTA stock solution absorption spectra (Chapter 11.1.) to compare the absorption bands of dyes and NPs (Figure 23).

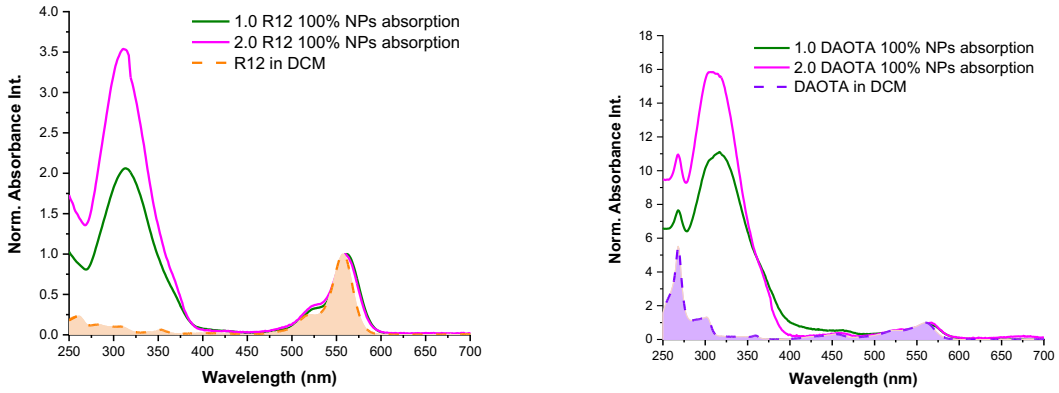

Figure 23. Normalized absorption spectra of 1.0 and 2.0 R12 (left) and DAOTA (right) SMILES nanoparticles showed together with normalized absorption spectra of R12 and DAOTA stock solutions in DCM as shaded areas under dashed lines.

Figure 23 shows the $S_0 \rightarrow S_1$ transition's absorption band at 561 nm for 1.0 R12 NPs, 560 nm for R12 2.0 NPs and 567 nm for both DAOTA NPs. 1.0 DAOTA NPs exhibit a spectral broadening around 400 nm compared to the spectrum of 2.0 DAOTA NPs. This can be assigned to aggregates and large particles that scatter light. As the spectrum of 2.0 DAOTA NPs with a smaller particle size resembles more closely those measured previously for DAOTA[48], it can be considered more reliable.

In addition to the dye's absorption band, both NPs exhibit a strong UV absorption band at around 309-313 nm, attributed to the cyanostar anion complex ($CS_2PF_6^-$). According to the earlier determined (Chapter 10.2) ~2.5 molar equivalents of cyanostar in the precursor solution, the absorption of cyanostar for 1.0 R12 has decreased and for 2.0 R12 increased in nanoparticles. Likewise, in DAOTA nanoparticles, the amount of cyanostar in 2.0 nanoparticles is higher than in 1.0 nanoparticles, although in both cases the molar equivalent of cyanostar is less than 2.5. For a more precise comparison, the absorbance of the precursor solution of 2.0 NPs should be measured. The lower absorbance values of 1.0 NPs could potentially be attributed to the inner filter effect caused by their larger particle size. When light passes through the sample at the CS band, the large particles absorb practically all the light, thereby diminishing the contribution of other cyanostar molecules in the light path and thus, the overall absorption in the cyanostar band. This effect should result in non-Lambert-Beer behavior and

might cause measurement errors. Nonetheless, providing a comprehensive explanation for this observation requires further experiments.

The small distortion in the spectra of 2.0 R12 nanoparticles at 319 nm is due to the instrument switching lamp from tungsten to deuterium at that wavelength. When considering the results, it should also be noted that the measurement accuracy may have been influenced by the absorbance values of 2.0 R12 and 1.0 DAOTA nanoparticles, which were slightly above the aimed 0.1. Additionally, errors in the concentrations between the nanoparticle samples 1.0 and 2.0 could have contributed to differences in the absorption spectra. Despite the 1.0 and 2.0 NPs differences in the absorption band at the CS band, the absorption spectra of the two SMILES nanoparticles at the dye's band closely resemble the spectra of dilute DCM solution. This suggests that the SMILES nanostructures have been successfully generated, inhibiting close dye-dye packing and electronic coupling.

11.3.2 IMZ and TBA SMILES nanoparticles

The samples were prepared separately by diluting 50 µl of IMZ or TBA NPs solution in 3 ml of Milli-Q water. The spectra with raw values are presented in Appendix 6. The absorption spectra of 1.0 and 2.0 nanoparticles were normalized to unity and plotted together.

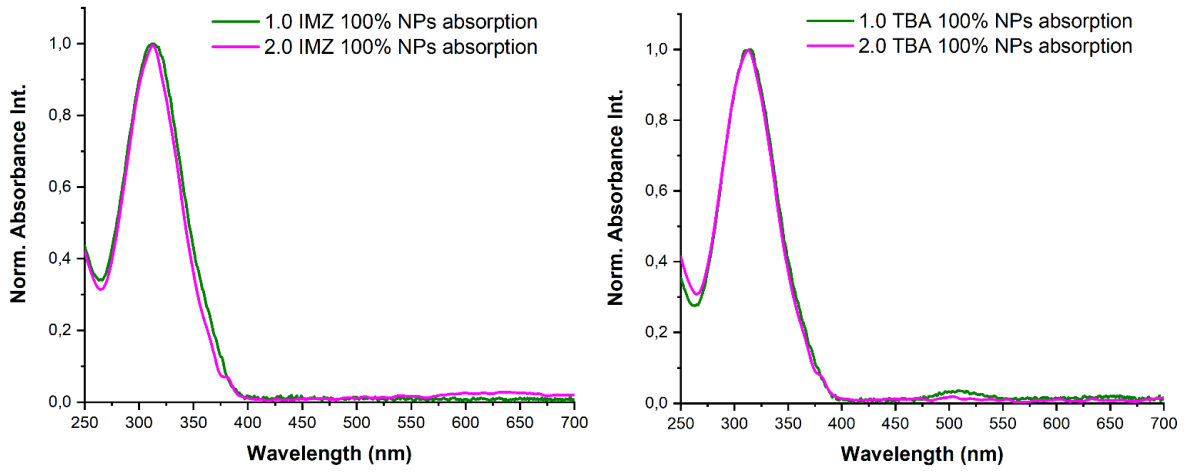

Figure 24. Normalized absorption spectra of IMZ and TBA 1.0 and 2.0 SMILES nanoparticles.

Since IMZ and TBA are optically inactive cations, Figure 24 shows the absorption of CS at 312 nm for IMZ NPs, at 315 nm for 1.0 TBA NPs and at 313 nm for 2.0 TBA NPs. The absorption peaks correspond to CS absorption at ~320 nm. Moreover, the shape of the absorption spectra are similar for the nanoparticles from the first and second nanoprecipitation in the case of both IMZ and TBA nanoparticles suggesting that the NPs size did not affect the absorption properties of the nanoparticles. Since the cyanostar molecule exhibits no absorption other than around 320 nm, the non-uniformity observed in the absorption spectrum of 1.0 TBA NPs around 500 nm can be interpreted as an impurity in the sample.

11.4 Absorption of filtered SMILES nanoparticles

The absorption of filtered SMILES nanoparticles was measured to observe the possible effect of filtering on the absorption spectra. The filtration was done to ensure that the absorption properties of the nanoparticles were not affected by any aggregates within the NPs. A comparison of the absorption properties between filtered and unfiltered nanoparticles was conducted for the 2.0 nanoparticles.

The samples were prepared by filtering R12, DAOTA, IMZ and TBA NPs solutions through a hydrophilic PTFE filter (0.22 µm). The filtered NP samples were measured using the same sample concentrations and measurement parameters as for the unfiltered nanoparticles (Chapter 11.3). The absorption spectra were measured using Milli-Q water as background and plotted together with unfiltered particles as a comparison (Figure 25).

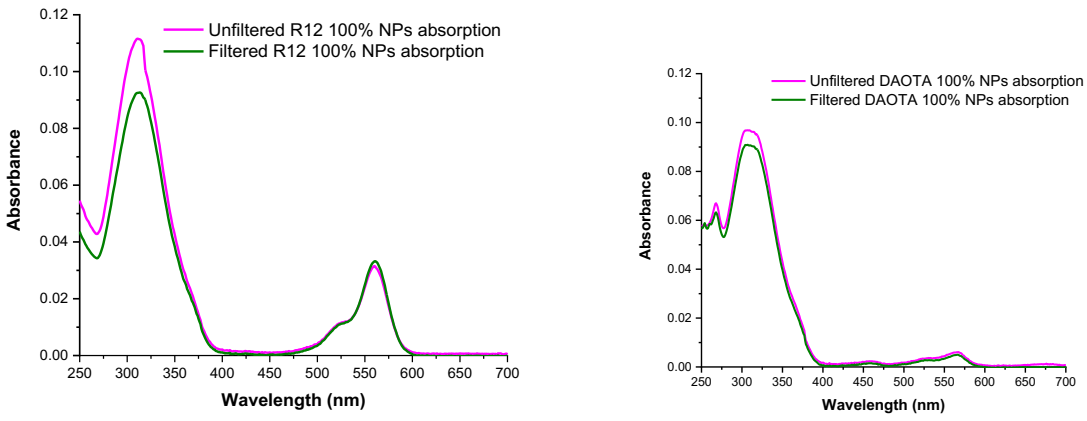

Figure 25. The absorption spectra of filtered and unfiltered R12 and DAOTA SMILES nanoparticles.

The filtering of R12 and DAOTA nanoparticles showed slightly decreased absorption intensity at the cyanostar band (Figure 25). The higher absorption intensity at the cyanostar band for unfiltered particles could be due to the presence of larger nanoparticles, which deviate from Lamber-Beer law dye to their increased size. The larger particles are removed by filtering, resulting in a more accurate absorption spectrum for the filtered sample. However, the filtration didn't affect the dye's absorption, meaning that no dye was removed by filtration.

Figure 26 shows a similar absorption spectral shape for the filtered and unfiltered IMZ and TBA nanoparticles. This could be due to the small size of IMZ and TBA SMILES nanoparticles and the homogeneity of the nanoparticle solution. All in all, because the absorption spectra were measured using the 2.0 SMILES nanoparticles with smaller particle size, filtering did not show any significant effect on the absorption of the nanoparticles. Hence, it was not considered necessary to filter the nanoparticle samples for further measurements.

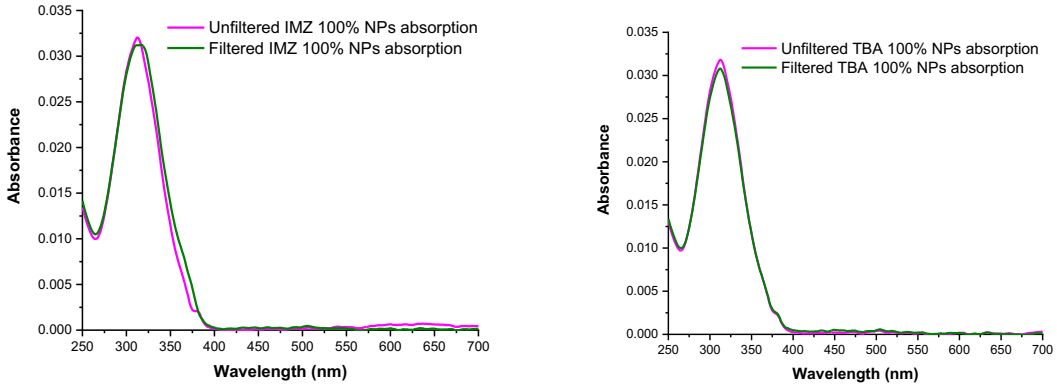

Figure 26. The absorption spectra of filtered and unfiltered IMZ and TBA SMILES nanoparticles.

12 Fluorescence spectroscopy

Fluorescence measurements were performed with the SMILES NPs samples prepared for UV-Vis spectroscopy (Chapter 11.3). The excitation wavelengths were chosen according to the maximum absorbance wavelengths from UV-Vis spectroscopy measurements. Milli-Q water was measured as a background.

12.1 R12 and DAOTA SMILES nanoparticles

Emission spectra of R12 and DAOTA SMILES nanoparticles were recorded with direct excitation using 530 nm excitation light. The excitation spectra were measured using 600 nm and 620 nm emission detection for both nanoparticles. The excitation spectra with 600 nm emission detection were selected for further analysis. The emission and excitation spectra (Appendix 7-10) were normalized and plotted together (Figure 27). In addition, the emission spectra of R12 and DAOTA SMILES nanoparticles 2.0 were recorded with excitation at cyanostar band at 320 nm to observe the emission of cyanostar (Appendix 11, Figure 28). The experimental parameters for fluorescence measurements are presented in Table 9.

Table 9. Parameters for fluorescence measurements.

Parameter	Value
Solvent	Water
Emission attenuator	90 %
Integration time per point	0.2 s
EXC & EM monochromator bandwidth	2.7 nm
Excitation wavelength	320/530 nm
Emission scanning wavelength	330/540 nm – 800 nm
Emission detection wavelength	600 nm
Excitation scanning wavelength	250 nm – 590/610 nm

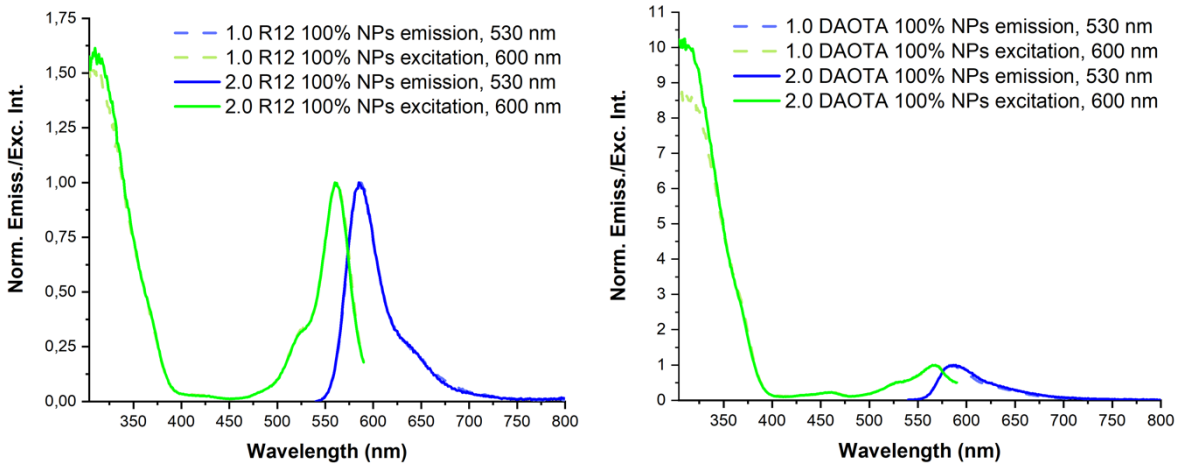

Figure 27. Normalized emission and excitation spectra of R12 and DAOTA SMILES nanoparticles (530 nm excitation and 600 nm emission detection).

Both R12 and DAOTA NPs show a peak in the emission spectrum with a maximum intensity at ~590 nm (Figure 27) comparable to previous studies.[13,48] The peak at ~560 nm in the excitation spectra of R12 and at ~568 nm of DAOTA NPs correspond to the earlier obtained absorption spectra (Chapter 11.3.1) and is attributed to the dye molecule. Respectively, the intensity maximum of R12 and DAOTA NPs excitation spectra at ~320 nm is assigned to the cyanostar anion complex. At that wavelength, the excitation intensities are slightly higher in 2.0 than 1.0 NPs, indicating a more efficient energy transfer in 2.0 NPs. Otherwise, the excitation spectra between 1.0 and 2.0 for R12 and DAOTA nanoparticles matched well. The emission spectra showed no apparent difference in fluorescence between 1.0 and 2.0 R12 and DAOTA NPs. This implies that variation in nanoparticle size did not affect remarkably their fluorescence characteristics.

Emission spectra of R12 and DAOTA nanoparticles excited in the cyanostar absorption band were expected to show a slight emission intensity corresponding to the cyanostar emission band at 430 nm. Contrary to the expectations, no significant signal for the emission of CS was seen in the spectra (Figure 28). Instead, a slight increase in emission intensity towards shorter wavelengths was observed, presumably due to impurities or scattered light. The small peak at 640 nm is assumed to result from the second-order excitation at 320 nm and may be assigned to instrument error.

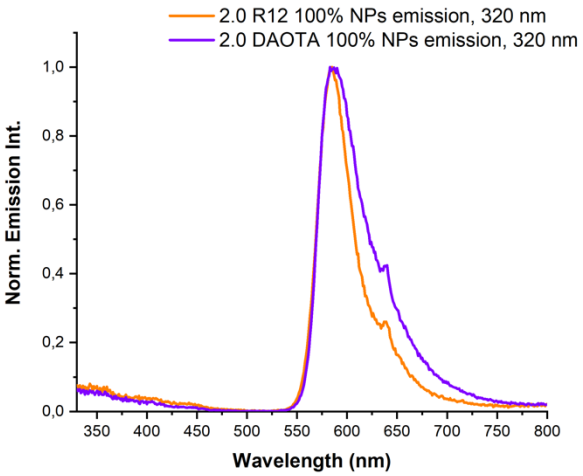

Figure 28. Normalized emission spectra of R12 and DAOTA 2.0 SMILES nanoparticles excited at 320 nm.

12.2 IMZ and TBA SMILES nanoparticles

For IMZ and TBA SMILES nanoparticles an excitation wavelength of 320 nm was used to measure the emission spectra of $CS_2PF_6^-$. Excitation spectra were measured using 400 nm, 430 nm, 450 nm and 500 nm emission detection for both SMILES nanoparticles to ensure the homogeneity of the particles. For further analysis, the excitation spectra with 430 nm emission detection were used. The emission and excitation spectra (Appendices 12–15) were normalized and plotted together (Figure 29). The experimental parameters for fluorescence measurements are presented in Table 10.

Table 10. Parameters for fluorescence measurements.

Parameter	Value
Solvent	Water
Emission attenuator	100 %
Integration time per point	0.2 s
EXC & EM monochromator bandwidth	7.0 nm
Excitation wavelength	320 nm
Emission scanning wavelength	330 nm – 800 nm
Emission detection wavelength	400/430/450/500 nm
Excitation scanning wavelength	250 nm – 390/420/440/490 nm

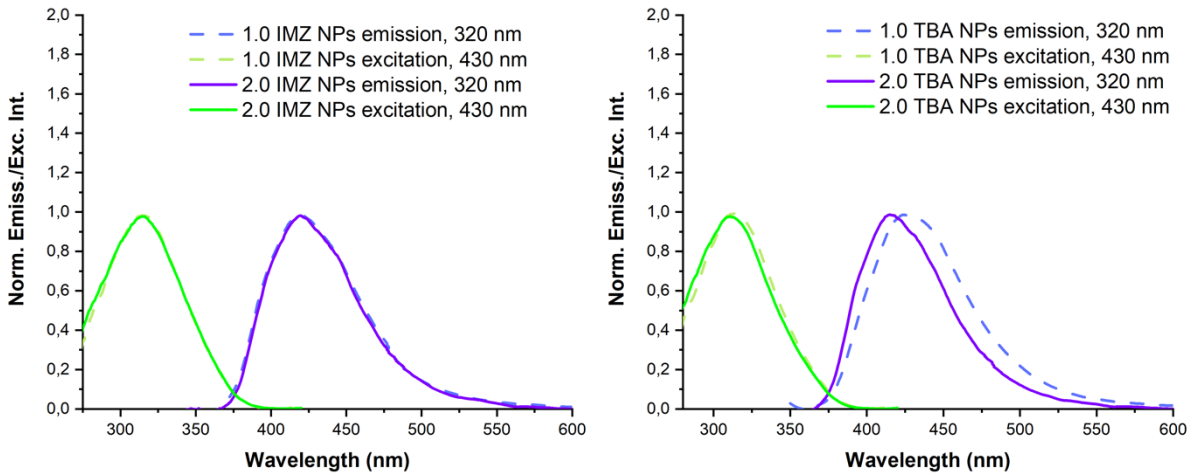

Figure 29. Normalized emission and excitation spectra of IMZ and TBA SMILES nanoparticles (320 nm excitation and 430 nm emission detection).

Due to the optically inactive characteristics of IMZ and TBA cations, the emission spectra of IMZ and TBA NPs display the fluorescence from the cyanostar anion complex, observed between 415-424 nm (Figure 29). The emission of TBA NPs from the first preparation exhibited a red shift compared to the emission of 2.0 TBA NPs. One hypothesis for this disparity could be that the larger size of 1.0 TBA NPs causes an inner filter effect as the large particles self-absorb light.

However, the same red shift does not appear in IMZ nanoparticles; otherwise, there are no differences in the emission spectra between 1.0 and 2.0 nanoparticles. The intensity maximum of the excitation spectra of IMZ and TBA NPs, assigned to cyanostar, appears between 310-316 nm. Although the larger particle size in 1.0 TBA NPs led to a slight difference in the emission of nanoparticles, the mainly similar emission and excitation spectra of 1.0 and 2.0 IMA and TBA NPs suggest that the nanoparticle size had no significant effect on the fluorescence properties of the nanoparticles.

13 Fluorescence properties of SMILES NPs

Since the nanoparticles obtained from the first and second nanoprecipitation differed significantly in particle size, it was investigated whether the particle size affects the optical properties of the nanoparticles. To compare the spectral properties of 1.0 and 2.0 nanoparticles, the UV-Vis and fluorescence results (chapters 11 and 12 were used to plot the normalized absorption, emission, and excitation spectra of the observed nanoparticles together.

Since the optical properties of the nanoparticles from the first and second nanoprecipitation did not differ significantly, only the 2.0 NPs with smaller particle sizes were chosen for further investigation. Additionally, all the following experiments were conducted using the 2.0 nanoparticles.

13.1 Comparison of optical properties of IMZ and TBA NPs

The first aim of investigating the cyanostar anion complex in nanoparticles was to determine whether the optically inactive cation affected the optical properties of the nanoparticles. To

achieve this, the normalized absorption, emission, and excitation spectra of IMZ and TBA NPs were plotted together for comparison.

The obtained spectra of IMZ and TBA SMILES nanoparticles (Figure 30) showed similar spectral shapes between IMZ and TBA NPs. This indicates that either of the cations could effectively be employed to investigate the cyanostar anion complex in nanoparticles. Furthermore, the comparable sizes of IMZ and TBA nanoparticles provide additional support for this conclusion.

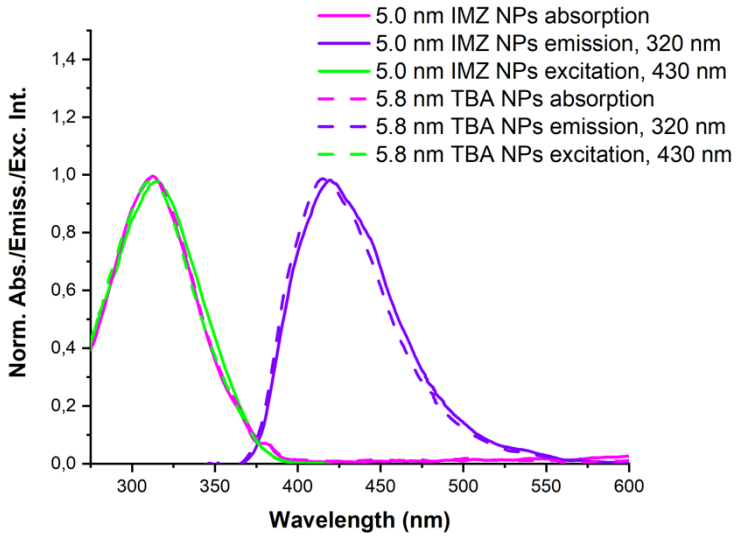

Figure 30. Normalized absorption, emission and excitation spectra of IMZ and TBA SMILES nanoparticles (320 nm excitation and 430 nm emission detection).

13.2 Relative Quantum Yield

For further analysis of the fluorescence properties of SMILES nanoparticles, relative quantum yields (RQY) were determined. The samples were prepared by diluting 50 µl of NPs solution in 3 ml of Milli-Q water. Based on Equation 4, the relative quantum yields for R12, DAOTA, IMZ and TBA SMILES nanoparticles were estimated by measuring their absorption and emission (Appendices 16–21) on the same day and dividing the emission by the absorbance value at the excitation wavelength used in emission measurement. The absorbance values were kept below 0.05 over the whole range of applied excitation wavelength (250-700 nm) to avoid the inner filter effect. The nanoparticles were excited at the cyanostar band at 320 nm. In

addition, R12 and DAOTA NPs were excited at the dyes' excitation band (530 nm). For all the measurements, water was measured as a background. The measurement parameters are presented in Table 11 and the graphs for resulting relative quantum yields in Figures 31 and 32.

Table 11. Parameters for R12, DAOTA, IMZ and TBA NPs fluorescence measurements.

Parameter	**Values for R12 and DAOTA NPs**	**Values for IMZ and TBA NPs**
Solvent	Water	Water
Emission attenuator	90 %	100%
Integration time per point	0.2 s	0.2 s
EXC & EM monochromator bandwidth	2.7 nm	7.0 nm
Excitation wavelength	320/530 nm	320 nm
Emission scanning wavelength	330/540 nm – 800 nm	330 nm – 800 nm

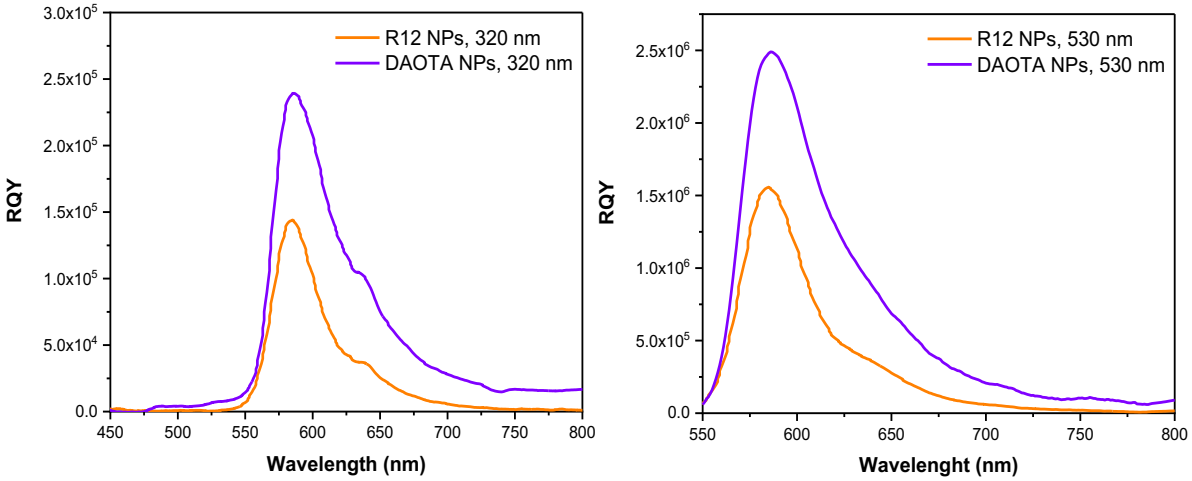

Figure 31. Estimated relative quantum yields of the R12 and DAOTA NPs with 320 nm excitation (left) and 530 nm excitation (right).

Since different measurement parameters (Table 11) were used when detecting the emissions for dyes and optically inactive cations, the comparison of the quantum yields is only possible between R12 and DAOTA NPs and between IMZ and TBA NPs. DAOTA NPs exhibited a higher quantum yield than R12 NPs when excited at both CS band and dye bands (Figure 31). The quantum yield of DAOTA NPs was determined to be 1.7 times higher than that of R12 NPs when excited at 320 nm and 1.6 higher when excited at 530 nm. The lower quantum yield of

R12 NPs could be assigned to a higher number of trap states acting as fluorescence quenchers. These trap states facilitate energy migration and lead to more efficient energy transfer away from the emissive states, thereby reducing the overall fluorescence efficiency.[13,46] While the energy transfer between dyes is assumed to be FRET, the increase in non-radiative relaxation leads to lower quantum yield (Equation 5).[17]

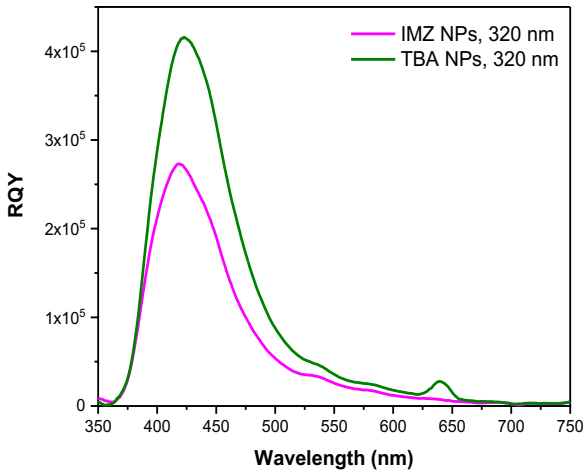

Figure 32. Estimated relative quantum yields of IMZ and TBA SMILES nanoparticles with 320 nm excitation.

TBA NPs have higher quantum yields than IMZ NPs (Figure 32), with a calculated ratio of 1.5 between their maximum relative quantum yield values. This difference in quantum yields is considered unexpected, given that IMZ and TBA NPs had nearly the same size and similar fluorescence spectra.

To understand the remarkably large difference between IMZ and TBA NPs' quantum yields, further investigation should be performed. Factors such as water content in nanoparticles or difference in surface area may quench the fluorescence of the nanoparticles and contribute to this variation. This unexpected outcome suggests that more optically inactive cations with different structures could be investigated to find the with the highest quantum yield.

The peak around 640 nm at excitation spectra of R12, DAOTA and TBA NPs is due to the second-order excitation of 320 nm, which is considered to be an instrument error. Interestingly, a respective spectral shape does not appear in the IMZ spectrum. Since the same bump was observed in the background spectra before subtracting it, this can be explained by an error in the background measurement.

Since these quantum yield results are relative, they can be regarded as indicative without giving any information on the actual fluorescence quantum yields of the nanoparticles. To obtain accurate fluorescence quantum yields a reference sample with a known quantum yield should be measured (Chapter 4.2.1).

13.3 Fluorescence lifetime

13.3.1 SMILES NPs

The samples for fluorescence lifetime measurements were prepared separately by diluting 50 µl of R12 and DAOTA NPs solution and 100 µl of IMZ and TBA NPs solutions in 3 ml of Milli-Q water. To ensure an absorbance below 0.1, the absorption spectra of NPs were measured using water as a background.

Fluorescence lifetimes of nanoparticles were detected using a pulse diode laser with an excitation wavelength of 300 nm, which was close to the CS excitation wavelength of around 320 nm. An emission detection wavelength of 600 nm was used for R12 and DAOTA SMILES NPs and 430 nm for IMZ and TBA SMILES NPs, respectively. The instrument response function (IRF) was obtained at the excitation wavelength (300 nm) using a dilute Ludox scattering solution.

Recorded fluorescence decay histograms were analysed and the exponential reconvolution fitting method was applied using FluoFit software from PicoQuant (Appendices 22–25). The average intensity weighed fluorescence lifetimes are presented in Table 12, and the multiexponential decays of NPs in Figure 33.

Table 12. Average intensity weighted fluorescence lifetimes of SMILES NPs.

	Excitation wavelength (nm)	**Detection wavelength (nm)**	$\tau_{\mathbf{Av.Int.}}$ **(ns)**
R12 NPs	300	600	2.28
DAOTA NPs	300	600	21.6
IMZ NPs	300	430	1.29
TBA NPs	300	430	1.28

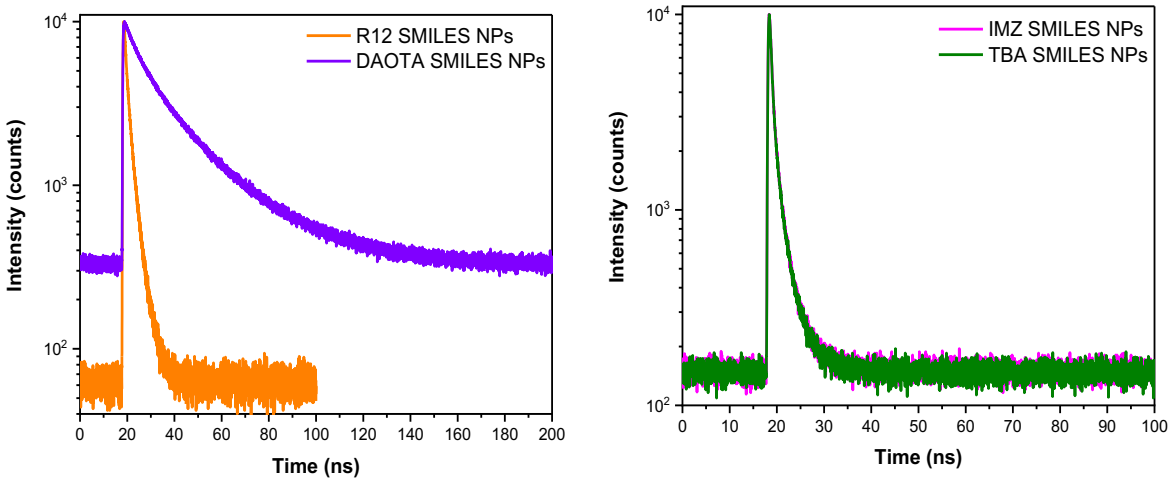

Figure 33. Fluorescence decays of R12 and DAOTA SMILES NPs (left) ($\lambda_{\text{em det}}$ = 600 nm) and IMZ and TBA SMILES NPs (right) ($\lambda_{\text{em det}}$ = 430 nm) all with λ_{ex} = 300 nm.

The R12 NPs fluorescence lifetime of 2.28 ns (Table 12) corresponds with previously obtained lifetimes between 2.1-2.6 ns for R12 SMILES NPs reported by Flood, Laursen *et al.*[13] Similarly, the 21.6 ns lifetime of DAOTA NPs is comparable with 24.8 ns lifetime reported by Stenspil *et al.*[47]

Figure 33 illustrates the almost 9.5-fold longer fluorescence lifetime of DAOTA NPs compared to that of R12 NPs, confirming the distinct characteristics of these two different chromophores. In contrast, as expected, the fluorescence decays of IMZ and TBA display almost identical lifetimes (Table 12 and Figure 33), supporting their previously observed similar fluorescence properties.

13.3.2 R12 and DAOTA SMILES NPs and fluorophores in DCM

To compare R12 and DAOTA SMILES NPs fluorescence lifetimes with the corresponding fluorophore lifetimes, the lifetimes of dyes in DCM were measured and compared to SMILES NPs lifetimes using the same excitation and emission detection wavelengths. The R12 and DAOTA SMILES NPs samples were prepared, and their absorption was measured as above (Chapter 13.3.1). The R12 and DAOTA fluorophore samples were prepared in DCM the same way as the stock solutions (Chapter 11.1) and their absorption was measured keeping the absorbance below 0.1 DCM as a background.

Fluorescence lifetimes of fluorophores in DCM and NPs were detected using pulse diode laser with an excitation wavelength of 560 nm, which was in the excitation band of both dyes. The measurement was performed with an emission detection wavelength of 600 nm for all the samples. The instrument response function (IRF) was obtained at the excitation wavelength (560 nm) using a dilute Ludox scattering solution.

Recorded fluorescence decay histograms were analysed and the exponential reconvolution fitting method was applied using FluoFit software from PicoQuant (Appendices 26–27). The average intensity weighed fluorescence lifetimes of dyes in DCM and NPs are presented in Table 13 and the multiexponential decays in Figure 34.

Table 13. Average intensity weighted fluorescence lifetimes of fluorophores in DCM compared to SMILES NPs.

	Excitation wavelength (nm)	**Detection wavelength (nm)**	$\tau_{\text{Av.Int.}}$ **in DCM (ns)**	$\tau_{\text{Av.Int.}}$ **in NPs (ns)**	$\frac{\tau_{\text{Av.Int.}} \text{ in NPs}}{\tau_{\text{Av.Int.}} \text{ in DCM}}$
R12	560	600	3.21	2.01	0.63
DAOTA	560	600	20.0	22.6	1.13

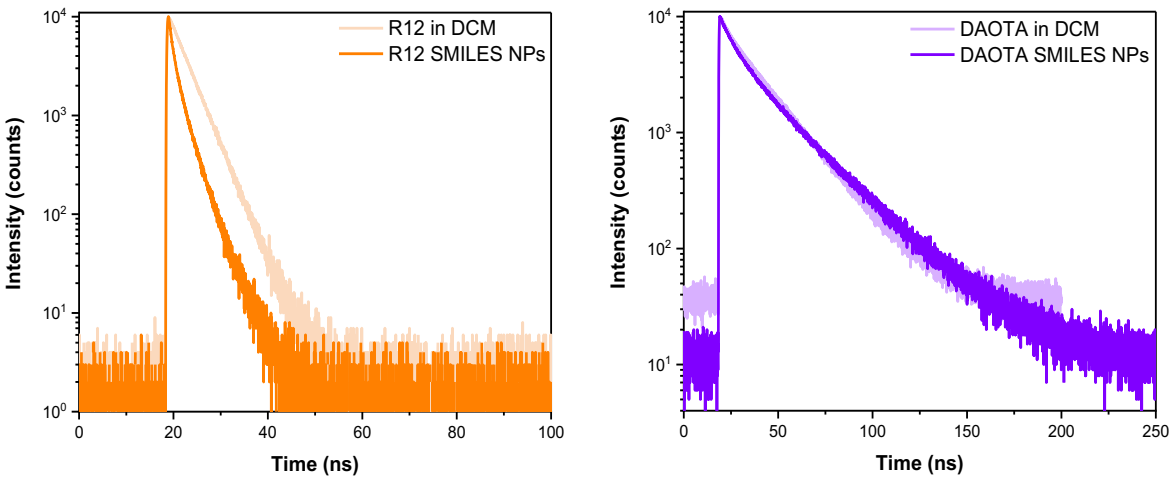

Figure 34. Fluorescence decays of R12 in DCM plotted with R12 SMILES NPs (left) and DAOTA in DCM plotted with DAOTA SMILES (right) all with λ_{ex} = 560 nm and $\lambda_{em\ det}$ = 600 nm.

The fluorescence lifetime decreased from 3.21 ns to 2.01 ns in R12 SMILES NPs compared to the R12 lifetime in the DCM solution (Table 13 and Figure 34). The lifetime of R12 NPs is

only 63 % of the lifetime of R12 in DCM. Similar effects of shortened rhodamine NPs lifetimes have been reported by Kacenauskaite *et al.*[46] and Stenspil *et al.*[47].

In contrast, DAOTA exhibited a longer lifetime (22.6 ns) in SMILES NPs than in DCM solution (20.0 ns), giving a 1.13-fold increase in lifetime in NPs compared to the dye's lifetime in DCM (Table 13). The decay of DAOTA NPs was fitted tri-exponentially, resulting in two lifetimes significantly shorter (11.4 ns and 3.6 ns) than the lifetime of DAOTA in DCM. This suggests that although the lifetime is longer in NPs, fluorescence is still quenched in the nanoparticle structure. This trend of DAOTA's lifetimes is further supported by the previously obtained lifetimes for DAOTA in SMILES NPs and in DCM.[47]

The non-monoexponential fluorescence decays of SMILES NPs result from the heterogeneity of non-radiative rates within the nanoparticles. The outcome for the multiexponential and shortened fluorescence decays has been attributed to energy migration to trap states. The energy migration between dyes in SMILES NPs enables excitons to migrate to dark trap states. An increased number of trap states in NPs with high dye loadings results in fluorescence quenching.[13,46] Furthermore, fluorescence lifetimes are further reduced with increasing FRET, as the fluorescence lifetime is predominantly influenced by non-radiative relaxation[17], as seen in Equation 6.[17]

The fluorescence decays of R12 and DAOTA SMILES NPs were plotted together to illustrate the difference in their decays when excited at the dye's band at 560 nm.

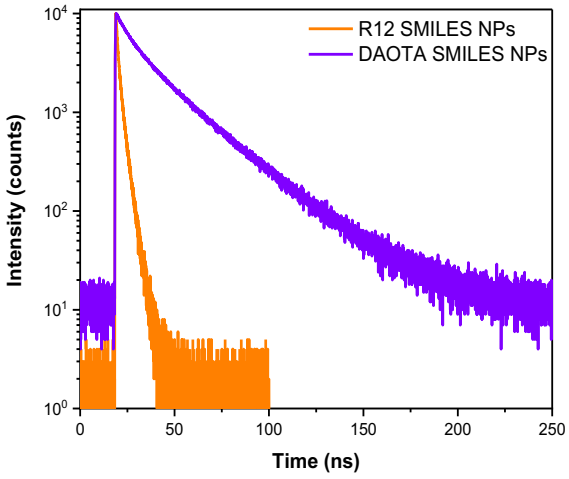

Figure 35. Fluorescence decays R12 and DAOTA SMILES NPs
(λ_{ex} = 560 nm, $\lambda_{em\ det}$ = 600 nm).

The fluorescence lifetime of DAOTA NPs was over 11 times longer than that of R12 NPs (Figure 35), consistent with the trend observed when exciting the NPs at the cyanostar band, 320 nm. While both nanoparticles display different fluorescence decays between SMILES NPs and solution, the decays appear multiexponential and contain short lifetime components. The shortened lifetimes, especially in R12 NPs, can be attributed to strong exciton coupling between transition dipoles of the molecular units, causing more effective energy migration.[46,47] In addition, the result that the fluorescence lifetime of R12 NPs is shortened more than that of DAOTA NPs, while the lifetime of DAOTA NPs remains almost unchanged when comparing the dye in DCM and in NPs is consistent with the lower quantum yield observed for R12 NPs (Chapter 13.2).

To outcompete the energy migration to dark trap states and enhance the lifetime of SMILES nanoparticles, the introduction of a dopant fluorophore (FRET acceptor) into SMILES materials has proven effective. This approach overcomes the challenges of shortened lifetimes in nanoparticles and reinstates the mono-exponential lifetime of the acceptor dye. Additionally, doping has shown to mitigate reabsorption effects in dense SMILES materials, resulting in ultrabright SMILES materials with enhanced fluorescence properties. With the superior properties resulting from the control of lifetime, these ultrabright SMILES nanoparticles are applicable for fluorescence lifetime imaging (FLIM) and time-gated imaging.[46,47]

13.4 Energy transfer in SMILES nanoparticles

To study the energy transfer from cyanostar anion complex ($CS_2PF_6^-$) to dye molecule in SMILES nanoparticles, the energy transfer efficiency for R12 and DAOTA SMILES nanoparticles was determined by measuring and comparing their absorption and excitation spectra.

The samples were prepared by diluting 50 µl of R12 and DAOTA NPs solution into 3 ml of Milli-Q water. The absorbance values were kept below 0.05 to avoid the inner filter effect over the whole range of applied excitation wavelength (250-700 nm).

The excitation spectra were measured with 610 nm emission detection using an EXC filter to filter excitation wavelength below 320 nm to avoid the second-order excitation at 640 nm.

Excitation spectra without filter were detected with the same measurement parameters (Table 14).

Table 14. Parameters for NPs excitation measurements.

Parameter	Value
Solvent	Water
Emission attenuator	100 %
Integration time per point	0.2 s
EXC & EM monochromator bandwidth	5.0 nm
Emission detection wavelength	610 nm
Excitation scanning wavelength	250 nm – 600 nm
Emission Filter	325 LP

The final excitation spectra of R12 and DAOTA NPs were obtained by combining the NPs excitation spectra at the dye's emission band measured with a filter and the NPs excitation spectra at the CS band detected without a filter (Appendix 28). To observe the energy transfer efficiency, the excitation spectra were normalized to the absorption spectra at the dye absorption band and their intensities at the cyanostar band were compared (Figure 36).

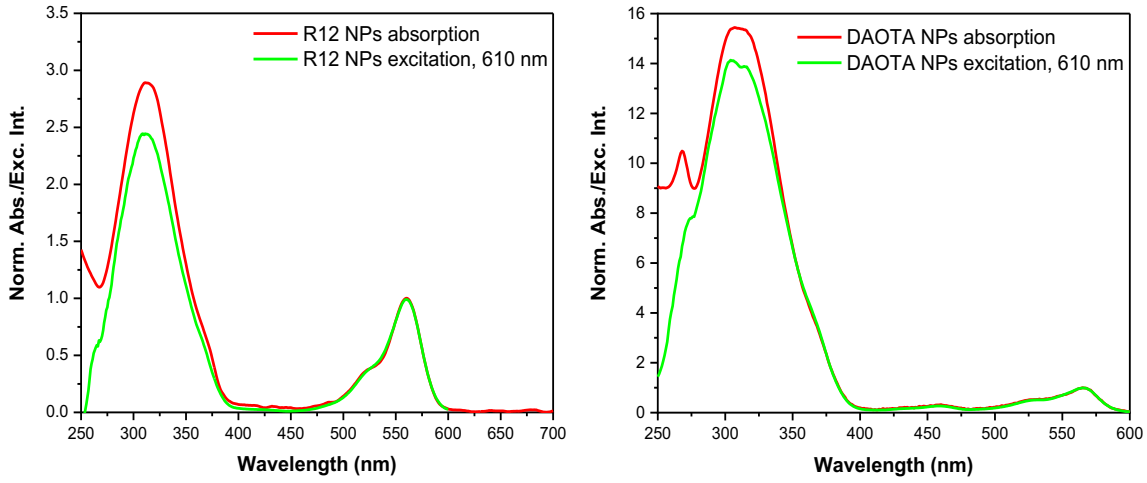

Figure 36. Normalized absorption and excitation spectra of 14.8 nm R12 SMILES and 20.0 nm DAOTA nanoparticles (610 nm emission detection).

The excitation energy transfer efficiencies Φ_{EET} of R12 and DAOTA SMILES nanoparticles were calculated from the formula (15) with the intensities obtained from nanoparticle

absorption and excitation spectra at CS band 320 nm (Figure 36). For R12 SMILES NPs the energy transfer efficiency was obtained to be:

$$\Phi_{\mathrm{EET}} = \frac{2.34907}{2.84934} \times 100\% = 82.44\% \approx 83\%$$

And for DAOTA SMILES NPs respectively:

$$\Phi_{\mathrm{EET}} = \frac{13.52759}{14.95687} \times 100\% = 90.44\% \approx 90\%$$

The relatively high energy transfer efficiencies indicate that only a small fraction of the excitation energy of the cyanostar anion complex is lost and not transferred to the dye in both nanoparticles. The slightly higher energy transfer efficiency observed in DAOTA SMILES nanoparticles compared to R12 SMILES nanoparticles implies more effective energy transfer from the cyanostar donor to the acceptor in DAOTA SMILES nanoparticles. Overall, energy transfer can be considered highly efficient in both nanoparticles.

To ensure the accuracy of calculated energy transfer efficiency percentages, the NPs excitation spectra were corrected to minimize the variations in excitation intensity and detector sensitivity using DAOTA solution in DCM. The absorption and excitation spectra of DAOTA in DCM were measured by diluting 3.5 µl of DAOTA in 3 ml of DCM (Appendix 29). The excitation spectrum was generated similarly to NPs, and both the absorption and excitation spectra were normalized to $S_0 \rightarrow S_1$ absorption bands of the DAOTA and plotted together. According to the Kasha-Vavilov rule,[53] which states that the excitation spectrum ideally matches the absorption spectrum, the detected deviation between the normalized absorption and excitation values can be used to correct the excitation spectra of the NPs. However, since the ratio of absorption and excitation spectra of DAOTA in DCM at 320 nm was relatively close to 1 ($\mathrm{DAOTA_{abs}}/\ \mathrm{DAOTA_{exc}} = 1.15$), indicating a minimal deviation, the excitation spectra of the R12 and DAOTA NPs were not corrected.

13.5 Spectral overlap

To investigate the energy transfer processes more precisely, spectral overlap integrals of the nanoparticles were determined. Since both Förster resonance energy transfer (FRET) and Dexter (electron exchange) can occur, the spectral overlap for both excitation transfer mechanisms was determined.

The spectral overlaps of R12 and DAOTA NPs were calculated from the right side of equation 17. The FRET overlap integrals J_F, were calculated using the fluorescence intensities of the donor and ε_A as the absolute value of the molar absorption coefficient at a specified wavelength of the acceptor. Molar absorption coefficient of 97 000 $M^{-1}cm^{-1}$ for R12 NPs and 15 000 $M^{-1}cm^{-1}$ for DAOTA NPs were used in the calculations.[13,48] Because the Dexter electron exchange is not affected by the molar absorption coefficient of the donor, normalized values of ε_A were used for the Dexter overlap integrals J_D before integration. The $J(\lambda)$ values calculated for FRET and Dexter were normalized by the area. The spectral overlap integrals are shown in Tables 15 and 16.

Table 15. Spectral overlap integrals of $CS_2PF_6^-$ in IMZ and TBA NPs as donors and R12 or DAOTA as acceptor for the assumed cases Förster (J_F) transfer.

	R12 J_F **($M^{-1}cm^{-1}nm^4$)**	**DAOTA** J_F **($M^{-1}cm^{-1}nm^4$)**	$\frac{J(\mathbf{R12})}{J(\mathbf{DAOTA})}$
IMZ	2.49×10^{15}	5.60×10^{14}	4.44
TBA	2.69×10^{15}	5.90×10^{14}	4.56

To illustrate the differences in spectral overlap integrals of R12 and DAOTA nanoparticles in FRET and Dexter energy transfer mechanisms, dyes' absorption spectra were plotted with IMZ NPs emission spectra. For FRET spectral overlap integrals, the absorption was presented with ε_A values (Figure 37), whereas in Dexter spectral overlap integrals the normalized ε_A values were used (Figure 38). The respective spectral overlap graphs of $CS_2PF_6^-$ in 5.8 nm TBA NPs are presented in Appendices 30–31.

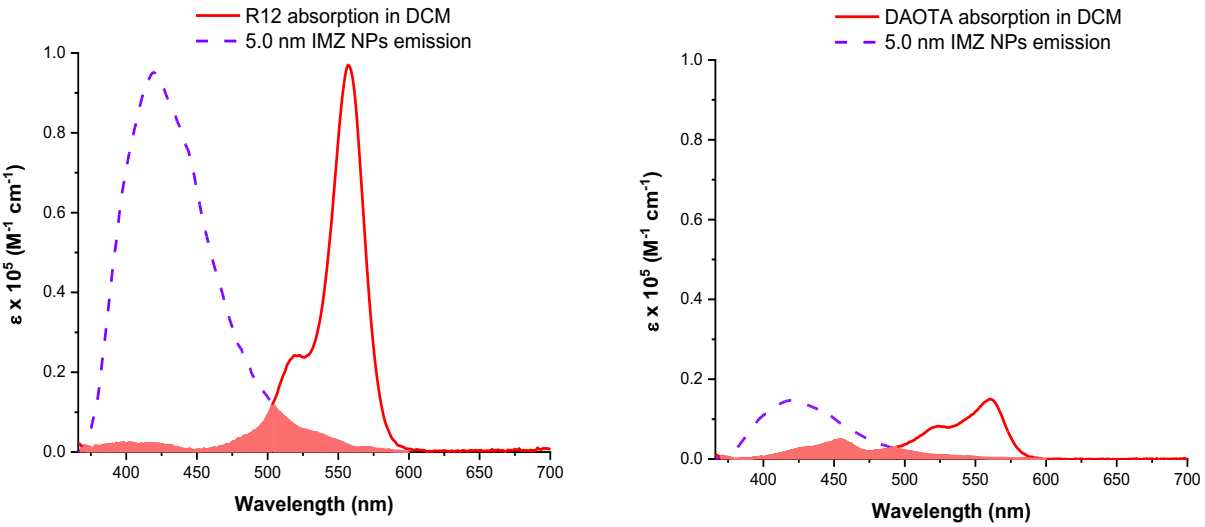

Figure 37. The absorption of R12 (left) and DAOTA (right) in DCM with 5.0 nm IMZ SMILES NPs emission spectra (320 nm excitation) normalized to the acceptor dye molar absorption spectra. The red area indicates the spectral overlap between the emission of the cyanostar anion complex and the absorption spectrum of dye in the case of Förster energy transfer.

The spectral overlap integral between the absorption of R12 in DCM and the 5.0 nm IMZ NPs emission normalized to the acceptors molar absorption coefficient is larger than the corresponding one for DAOTA (Figure 37). This large spectral overlap of R12 illustrates the around 4.5 times higher spectral overlap integral of R12 compared to DAOTA (Table 15). Since the integral *J* in the energy transfer rate (formula 16) is the only factor that contains information about the acceptor, and the other factors are donor-dependent, comparing the integrals for different dyes allows for a direct reflection of the energy transfer rates. The higher spectral overlap integral of R12 indicates that if R12 were replaced in the nanoparticles by DAOTA dye, keeping everything else the same, the energy transfer would be around 4.4 times faster for R12 compared to DAOTA.

The significantly larger spectral overlap of R12 can be explained by the higher molar absorption coefficient of R12 in the case of FRET energy transfer. Since the spectral overlap integral is a determining factor for energy transfer efficiency, FRET energy transfer could be expected to be more efficient in R12 NPs than in DAOTA NPs if it is assumed to be the dominant energy transfer mechanism.

Table 16. Spectral overlap integrals of $CS_2PF_6^-$ in IMZ and TBA NPs as donors and R12 or DAOTA as acceptor for the assumed cases Dexter (J_D) transfer.

	R12 J_D **(nm⁴)**	**DAOTA** J_D **(nm⁴)**	$\frac{J(\mathbf{R12})}{J(\mathbf{DAOTA})}$
IMZ	2.56×10^{10}	3.73×10^{10}	0.69
TBA	2.77×10^{10}	3.93×10^{10}	0.71

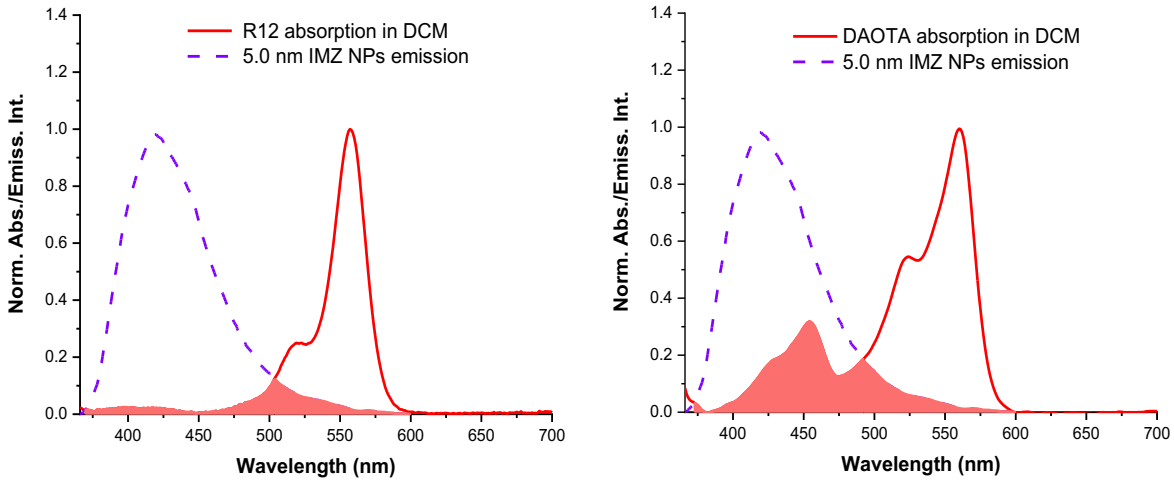

Figure 38. Normalized absorption spectrum of R12 (left) and DAOTA (right) in DCM with the emission spectra (320 nm excitation) 5.0 nm IMZ SMILES. The red area indicates spectral overlap between the emission of the cyanostar anion complex and the absorption spectrum of dye in the case of Dexter energy transfer.

Contrary to FRET energy transfer, the spectral overlap integrals in the case of Dexter energy transfer show relatively higher numbers for DAOTA than R12 (Table 16). For the Dexter energy transfer process, the spectral overlap integral for R12 as an acceptor is only 70% of the spectral overlap integral for DAOTA as an acceptor, meaning that the energy transfer would be 30% slower in R12 than in DAOTA. Figure 38 illustrates the larger spectral overlap between the absorption of acceptor dye in DCM and 5.0 nm IMZ NPs emission in the for DAOTA than R12. These results suggest that if the energy transfer processes in SMILES nanoparticles predominantly occur via the Dexter mechanism, the energy transfer would be more efficient for the DAOTA dye.

The previously obtained energy transfer efficiencies (Chapter 13.4.) indicated that energy transfer was slightly more efficient in DAOTA NPs (90%) than in R12 NPs (83%). Based on

these results, it can be inferred that the predominant energy transfer in SMILES nanoparticles is essentially Dexter electron exchange. The spectral overlap integrals indicated that FRET should be over 4 times more efficient in R12 NPs than in DAOTA NPs. However, since the calculated energy transfer efficiencies do not align with this expectation, it suggests that the dominant mechanism for energy transfer is primarily Dexter rather than FRET. This result can be considered intriguing as it contradicts the previously reported studies assuming the Förster-like transfer to be dominant.[23]

However, as the energy transfer in both nanoparticles is very efficient and the difference between them is small, further research is needed to conclusively determine which dye exhibits more efficient energy transfer. To achieve this, the actual energy transfer rates in both R12 and DAOTA nanoparticles could be determined if all the necessary factors, such as exact distances and orientations in the nanoparticles were known. In addition, nanoparticles with a mixture of IMZ/TBA cation and dye should be prepared to study the energy transfer efficiencies with fewer dye molecules and not with full energy transfer to comprehensively understand which dye has the most efficient energy transfer.

14 Conclusion

SMILES (Small molecule ionic isolation lattices) nanoparticles containing dye molecules have emerged as promising candidates for bioimaging applications. They offer various attractive properties over traditional commercially available fluorescent dye labels. SMILES nanoparticles offer a solution to the strong fluorescence-degrading interactions commonly observed in organic dyes by decreasing the aggregation-caused quenching. Due to their specific structure and enhanced optical properties the advantages of SMILES nanoparticles include increased brightness and photostability.

The aim of the experimental part was to investigate the energy transfer processes from the cyanostar anion complex to the dyes in SMILES nanoparticles. To achieve this, nanoparticles with optically active dyes R12 and DAOTA and nanoparticles with optically inactive cations IMZ and TBA were synthesized. Two series of SMILES nanoparticles were prepared using the same nanoprecipitation method but with different injection rates. The sizes of the formed

nanoparticles were determined with DLS and cryo-TEM and their optical properties were studied using absorption and fluorescence spectroscopy.

The energy transfer efficiencies from the cyanostar anion complex to the dyes and spectral overlap integrals between the cyanostar anion complex and the dye molecules were determined. The energy transfer efficiency for DAOTA SMILES nanoparticles was 90 % and 83 % for R12 SMILES nanoparticles. The energy transfer process in SMILES nanoparticles was determined to be mainly Dexter electron exchange rather than Förster resonance energy transfer, as suggested in previous studies.

Despite the advanced optical properties and the efficient energy transfer in SMILES nanoparticles, there are still challenges that need to be tackled. The photophysical effects, such as strong dye-dye interactions, trap states and fluorescence quenching due to energy migration to these trap states, limit the brightness of fluorescent SMILES nanoparticles. Addressing these challenges will be crucial for further enhancing the performance and applicability of SMILES nanoparticles in various fields, including bioimaging and bioanalysis.

To overcome these challenges and improve the fluorescence properties of SMILES nanoparticles, doping of the nanoparticles with FRET acceptors has already shown effective results enabling their use in fluorescence lifetime imaging. Furthermore, the development of reactive surface coatings for SMILES nanoparticles is crucial to facilitate their application in targeted bioimaging. Dye-based nanoparticles hold a potential promise due to their ability to efficiently transfer superior properties from organic dyes into nanoparticles. However, achieving this requires a thorough understanding of their supramolecular structures and interactions.

15 References

1. Chen, Z.; Ho, C. L.; Wang, L. and Wong, W. Y., Single-Molecular White-Light Emitters and Their Potential WOLED Applications, *Adv. Mater.*, **2020**, *32*, 1–45.
2. Middha, E. and Liu, B., Nanoparticles of Organic Electronic Materials for Biomedical Applications, *ACS Nano*, **2020**, *14*, 9228–9242.
3. Ostroverkhova, O., Organic Optoelectronic Materials: Mechanisms and Applications, *Chem. Rev.*, **2016**, *116*, 13279–13412.
4. Klymchenko, A. S.; Liu, F.; Collot, M. and Anton, N., Dye-Loaded Nanoemulsions: Biomimetic Fluorescent Nanocarriers for Bioimaging and Nanomedicine, *Adv. Healthc. Mater.*, **2021**, *10*, 1–27.
5. Reisch, A. and Klymchenko, A. S., Fluorescent Polymer Nanoparticles Based on Dyes: Seeking Brighter Tools for Bioimaging, *Small*, **2016**, *12*, 1968–1992.
6. Zhang, B.; Soleimaninejad, H.; Jones, D. J.; White, J. M.; Ghiggino, K. P.; Smith, T. A. and Wong, W. W. H., Highly fluorescent molecularly insulated perylene diimides: Effect of concentration on photophysical properties, *Chem. Mater.*, **2017**, *29*, 8395–8403.
7. Aparin, I. O.; Melnychuk, N. and Klymchenko, A. S., Ionic Aggregation-Induced Emission: Bulky Hydrophobic Counterions Light Up Dyes in Polymeric Nanoparticles, *Adv. Opt. Mater.*, **2020**, *8*, 1–10.
8. Reisch, A.; Didier, P.; Richert, L.; Oncul, S.; Arntz, Y.; Mély, Y. and Klymchenko, A. S., Collective fluorescence switching of counterion-assembled dyes in polymer nanoparticles, *Nat. Commun.*, **2014**, *5*, 1–9.
9. Collot, M.; Schild, J.; Fam, K. T.; Bouchaala, R. and Klymchenko, A. S., Stealth and bright monomolecular fluorescent organic nanoparticles based on folded amphiphilic polymer, *ACS Nano*, **2020**, *14*, 13924–13937.
10. Cai, X. and Liu, B., Aggregation-Induced Emission: Recent Advances in Materials and Biomedical Applications, *Angew. Chem. Int. Ed. Engl.*, **2020**, *59*, 9868–9886.
11. Xu, S.; Duan, Y. and Liu, B., Precise Molecular Design for High-Performance Luminogens with Aggregation-Induced Emission, *Adv. Mater.*, **2020**, *32*, 1–31.
12. Benson, C. R.; Kacenauskaite, L.; VanDenburgh, K. L.; Zhao, W.; Qiao, B.; Sadhukhan, T.; Pink, M.; Chen, J.; Borgi, S.; Chen, C. H.; Davis, B. J.; Simon, Y. C.; Raghavachari, K.; Laursen, B. W. and Flood, A. H., Plug-and-Play Optical Materials from Fluorescent Dyes and Macrocycles, *Chem*, **2020**, *6*, 1978–1997.
13. Chen, J.; Fateminia, S. M. A.; Kacenauskaite, L.; Bærentsen, N.; Grønfeldt Stenspil, S.; Bredehoeft, J.; Martinez, K. L.; Flood, A. H. and Laursen, B. W., Ultrabright Fluorescent

Organic Nanoparticles Based on Small-Molecule Ionic Isolation Lattices, *Angew. Chem. Int. Ed.*, **2021**, *60*, 9450–9458.

14. Sun, X.; Rossin, R.; Turner, J. L.; Becker, M. L.; Joralemon, M. J.; Welch, M. J. and Wooley, K. L., An assessment of the effects of shell cross-linked nanoparticle size, core composition, and surface PEGylation on in vivo biodistribution, *Biomacromolecules*, **2005**, *6*, 2541–2554.
15. Fang, F.; Li, M.; Zhang, J. and Lee, C. S., Different Strategies for Organic Nanoparticle Preparation in Biomedicine, *ACS Mater. Lett.*, **2020**, *2*, 531–549.
16. Wiederschain, G. Ya., The Molecular Probes handbook. A guide to fluorescent probes and labeling technologies, *Biochem. (Mosc.)*, **2011**, *76*, 1276–1276.
17. Lakowicz, J. R., *Principles of Fluorescence Spectroscopy*, 3rd edition, Springer, New York, 2006, pp. 1–12 and 443–447.
18. Zheng, Q.; Juette, M. F.; Jockusch, S.; Wasserman, M. R.; Zhou, Z.; Altman, R. B. and Blanchard, S. C., Ultra-stable organic fluorophores for single-molecule research, *Chem. Soc. Rev.*, **2014**, *43*, 1044–1056.
19. Li, K.; Ren, T. B.; Huan, S.; Yuan, L. and Zhang, X. B., Progress and Perspective of Solid-State Organic Fluorophores for Biomedical Applications, *J. Am. Chem. Soc.*, **2021**, *143*, 21143–21160.
20. Würthner, F.; Kaiser, T. E. and Saha-Möller, C. R., J-aggregates: From serendipitous discovery to supramolecular engineering of functional dye materials, *Angew. Chem. Int. Ed.*, **2011**, *50*, 3376–3410.
21. Qi, J.; Sun, C.; Zebibula, A.; Zhang, H.; Kwok, R. T. K.; Zhao, X.; Xi, W.; Lam, J. W. Y.; Qian, J. and Tang, B. Z., Real-Time and High-Resolution Bioimaging with Bright Aggregation-Induced Emission Dots in Short-Wave Infrared Region, *Adv. Mater.*, **2018**, *30*, 1–9.
22. Qiao, B.; Hirsch, B. E.; Lee, S.; Pink, M.; Chen, C. H.; Laursen, B. W. and Flood, A. H., Ion-Pair Oligomerization of Chromogenic Triangulenium Cations with Cyanostar-Modified Anions That Controls Emission in Hierarchical Materials, *J. Am. Chem. Soc.*, **2017**, *139*, 6226–6233.
23. Chen, J.; Stenspil, S. G.; Kaziannis, S.; Kacenauskaite, L.; Lenngren, N.; Kloz, M.; Flood, A. H. and Laursen, B. W., Quantitative Energy Transfer in Organic Nanoparticles Based on Small-Molecule Ionic Isolation Lattices for UV Light Harvesting, *ACS Appl. Nano Mater.*, **2022**, *5*, 13887–13893.
24. Li, K. and Liu, B., Polymer-encapsulated organic nanoparticles for fluorescence and photoacoustic imaging, *Chem. Soc. Rev.*, **2014**, *43*, 6570–6597.

25. Joung, J. F.; Han, M.; Jeong, M. and Park, S., Experimental database of optical properties of organic compounds, *Sci. Data*, **2020**, *7*, 1–6.
26. Nilapwar, S. M.; Nardelli, M.; Westerhoff, H. V. and Verma, M., Absorption spectroscopy, *Meth. Enzymol.*, **2011**, *500*, 59–75.
27. Harris, D., *Quantitative Chemical Analysis*, 7th edition, W. H. Freeman and Company, New York, 2007, pp. 378–423.
28. Becker, W., *Advanced time-correlated single photon counting techniques*, 1st edition, Springer, New York, 2005, pp. 20–25.
29. Jia, Z.; Li, J.; Gao, L.; Yang, D. and Kanaev, A., Dynamic Light Scattering: A Powerful Tool for In Situ Nanoparticle Sizing, *Colloids and Interfaces*, **2023**, *7*, 1–18.
30. Mudalige, T.; Qu, H.; Van Haute, D.; Ansar, S. M.; Paredes, A. and Ingle, T., *Nanomaterials for Food Applications*, Elsevier, Valencia, 2018, pp. 313–353.
31. Milne, J. L. S.; Borgnia, M. J.; Bartesaghi, A.; Tran, E. E. H.; Earl, L. A.; Schauder, D. M.; Lengyel, J.; Pierson, J.; Patwardhan, A. and Subramaniam, S., Cryo-electron microscopy - A primer for the non-microscopist, *FEBS Journal*, **2013**, 280, 28–45.
32. Skoog, D.; West, D.; Holler, J. and Crouch, S., Fundamentals of Analytical Chemistry. 9th edition, Brooks/Cole, Cengage Learning, Belmont, 2013, pp. 650–772.
33. Günzler, H. and Williams, A., *Handbook of Analytical Techniques,* WILEY-VCH, Weinheim, 2001, pp. 419–463.
34. Heath, J. and Poggel, C., *UV-Vis-NIR spectroscopy for nanomaterials research*, 1st edition, John Wiley & Sons Ltd., Chichester, West Sussex, 2021, pp. 1–38.
35. Würth, C.; Grabolle, M.; Pauli, J.; Spieles, M. and Resch-Genger, U., Relative and absolute determination of fluorescence quantum yields of transparent samples, *Nat. Protoc.*, **2013**, *8*, 1535–1550.
36. Levitus, M., Tutorial: Measurement of fluorescence spectra and determination of relative fluorescence quantum yields of transparent samples, *Methods. Appl. Fluoresc.*, **2020**, *8*, 1–36.
37. Becker, W., *Advanced Time-Correlated Single Photon Counting Applications*. 1st edition, Springer Series in Chemical Physics, Berlin, 2015, pp. 1–124.
38. Stetefeld, J.; McKenna, S. A. and Patel, T. R., Dynamic light scattering: a practical guide and applications in biomedical sciences, *Biophys. Rev.*, **2016**, *8*, 409–427.
39. Kaszuba, M.; McKnight, D.; Connah, M. T.; McNeil-Watson, F. K. and Nobbmann, U., Measuring sub nanometre sizes using dynamic light scattering, *J. Nanopart. Res.*, **2008**, *10*, 823–829.

40. Danaei, M.; Dehghankhold, M.; Ataei, S.; Hasanzadeh Davarani, F.; Javanmard, R.; Dokhani, A.; Khorasani, S. and Mozafari, M. R., Impact of particle size and polydispersity index on the clinical applications of lipidic nanocarrier systems, *Pharmaceutics*, **2018**, *10*, 57.
41. Franken, L. E.; Grünewald, K.; Boekema, E. J. and Stuart, M. C. A., A Technical Introduction to Transmission Electron Microscopy for Soft-Matter: Imaging, Possibilities, Choices, and Technical Developments, *Small*, **2020**, *16*, 1–5.
42. Benjin, X. and Ling, L., Developments, applications, and prospects of cryo-electron microscopy, *Protein Science*, **2020**, 29, 872–882.
43. Fan, X.; Wang, J.; Zhang, X.; Yang, Z.; Zhang, J. C.; Zhao, L.; Peng, H. L.; Lei, J. and Wang, H. W., Single particle cryo-EM reconstruction of 52 kDa streptavidin at 3.2 Angstrom resolution, *Nat. Commun.*, **2019**, *10*, 1–11.
44. Stryer, L. and Hauglandt, R. P., Energy transfer: a spectroscopic ruler, *PNAS*, **1967**, *58*, 719–726.
45. Adronov, A. and Frechet, J. M. J., Light-harvesting dendrimers, *Chem. Comm.*, **2000**, 1701–1710.
46. Kacenauskaite, L.; G. Stenspil, S.; H. Olsson, A.; H. Flood, A. and W. Laursen, B., Universal Concept for Bright, Organic, Solid-State Emitters─Doping of Small-Molecule Ionic Isolation Lattices with FRET Acceptors, *J. Am. Chem. Soc.*, **2022**, *144*, 19981–19989.
47. Stenspil, S. G.; Chen, J.; Liisberg, M. B.; Flood, A. H. and Laursen, B. W., Control of the fluorescence lifetime in dye based nanoparticles, *Chem. Sci.*, **2024**, *15*, 5531–5538.
48. Laursen, B. W. and Krebs, F. C., Synthesis, Structure, and Properties of Azatriangulenium Salts, *Chem. Eur. J.*, **2001**, *7*, 1773–1783.
49. Thyrhaug, E.; Sørensen, T. J.; Gryczynski, I.; Gryczynski, Z. and Laursen, B. W., Polarization and symmetry of electronic transitions in long fluorescence lifetime triangulenium dyes, *J. Phys. Chem. A.*, **2013**, *117*, 2160–2168.
50. Bogh, S. A.; Simmermacher, M.; Westberg, M.; Bregnhøj, M.; Rosenberg, M.; De Vico, L.; Veiga, M.; Laursen, B. W.; Ogilby, P. R.; Sauer, S. P. A. and Sørensen, T. J., Azadioxatriangulenium and Diazaoxatriangulenium: Quantum Yields and Fundamental Photophysical Properties, *ACS Omega*, **2017**, *2*, 193–203.
51. Shulov, I.; Oncul, S.; Reisch, A.; Arntz, Y.; Collot, M.; Mely, Y. and Klymchenko, A. S., Fluorinated counterion-enhanced emission of rhodamine aggregates: Ultrabright nanoparticles for bioimaging and light-harvesting, *Nanoscale*, **2015**, *7*, 18198–18210.

52. Blauenfeldt Jensen, N., *Optical properties of SMILES nanoparticles with the redshifted dye Rhodamine 800*, Thesis Paper, Kemisk Institut, Copenhagen, 2023.

53. Veys, K. and Escudero, D., Anti-Kasha Fluorescence in Molecular Entities: Central Role of Electron–Vibrational Coupling, *Acc. Chem. Res.*, **2022**, *55*, 2698–2707.

16 Appendices

APPENDIX 1

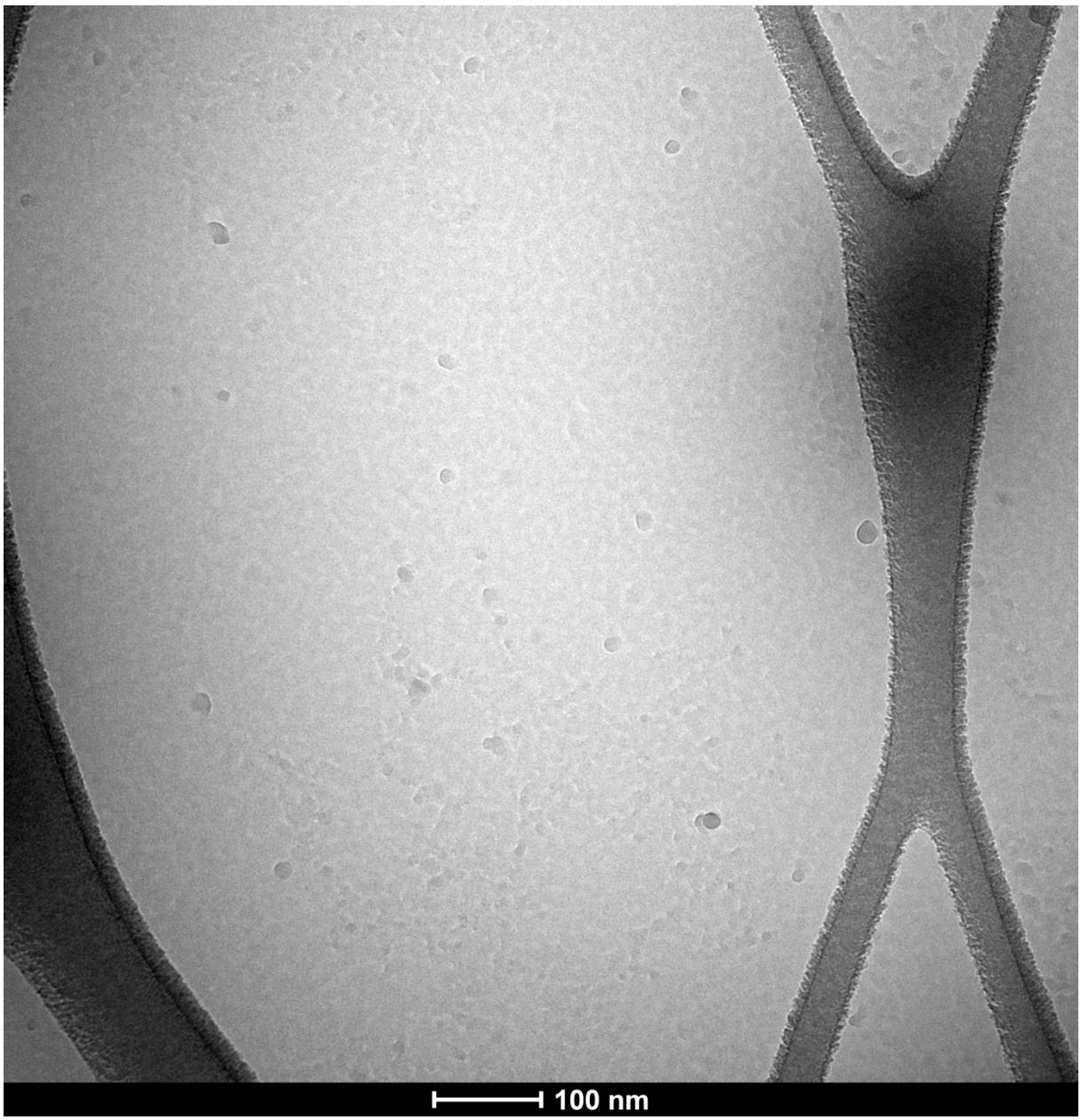

APPENDIX 2

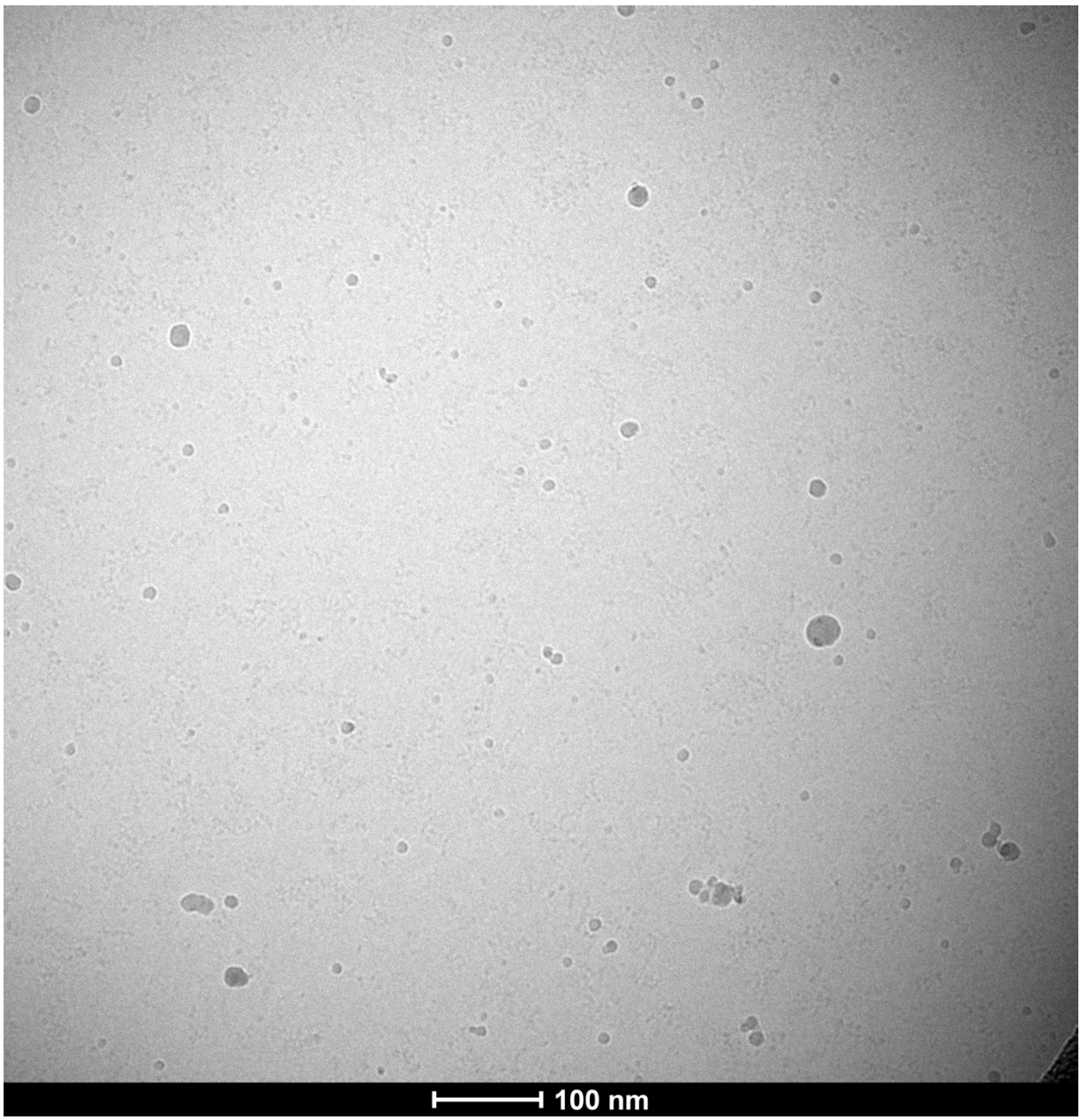

APPENDIX 3

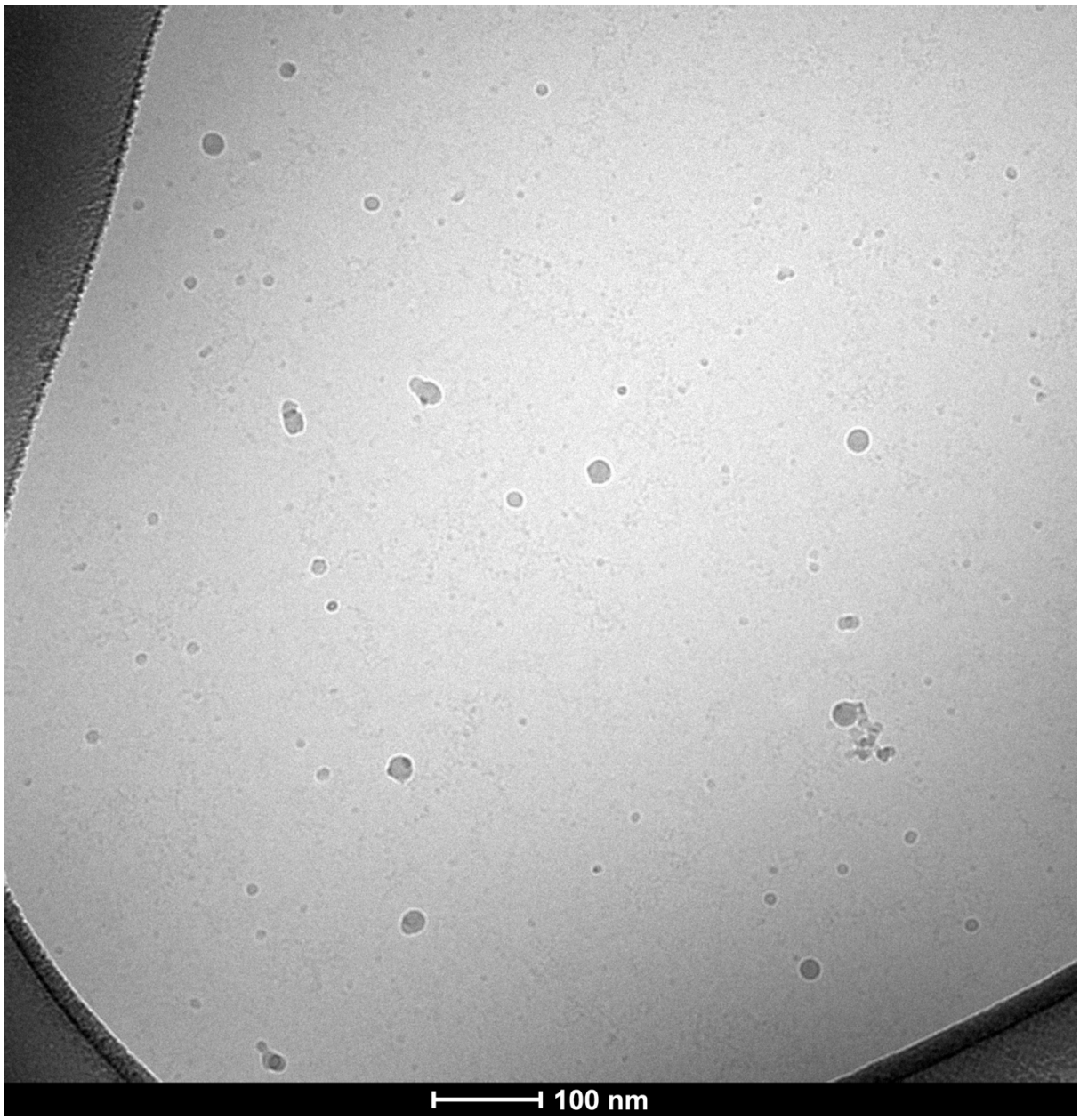

APPENDIX 4

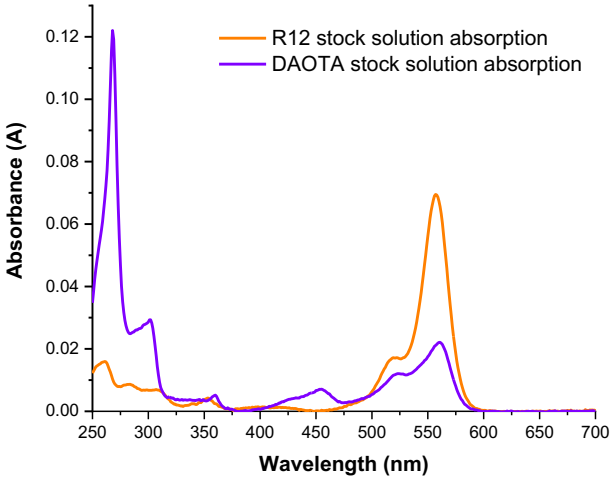

APPENDIX 5

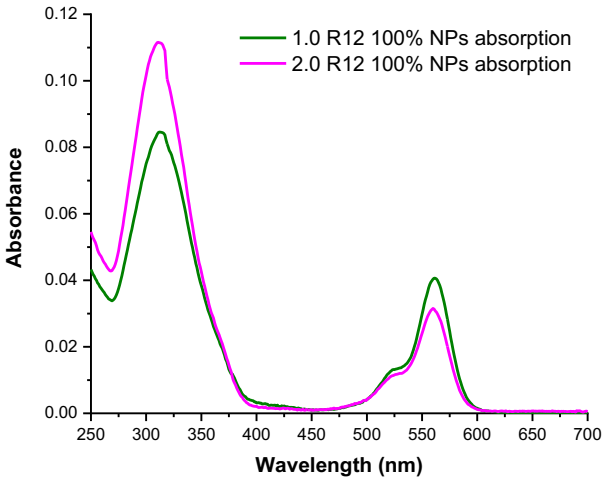

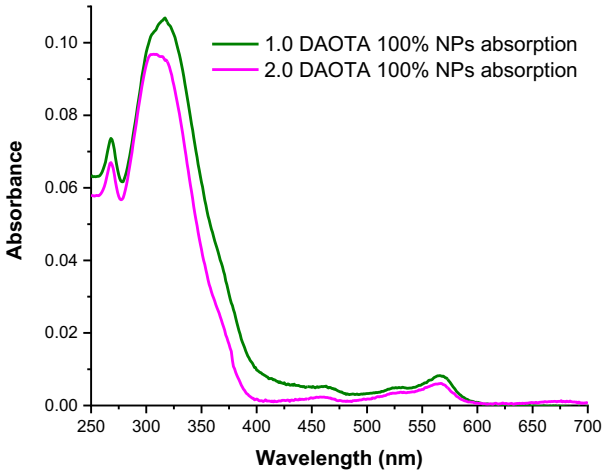

APPENDIX 6

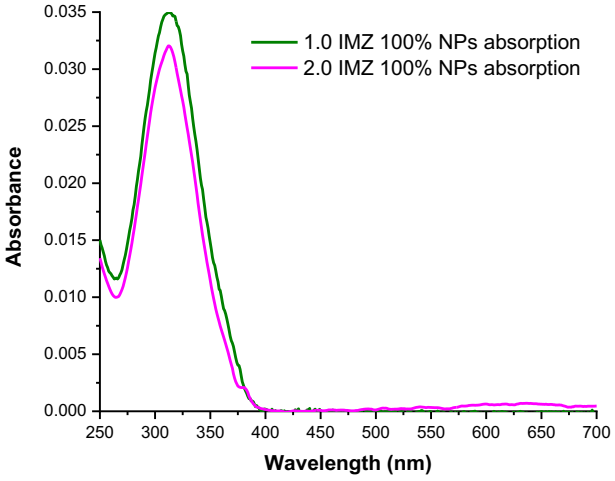

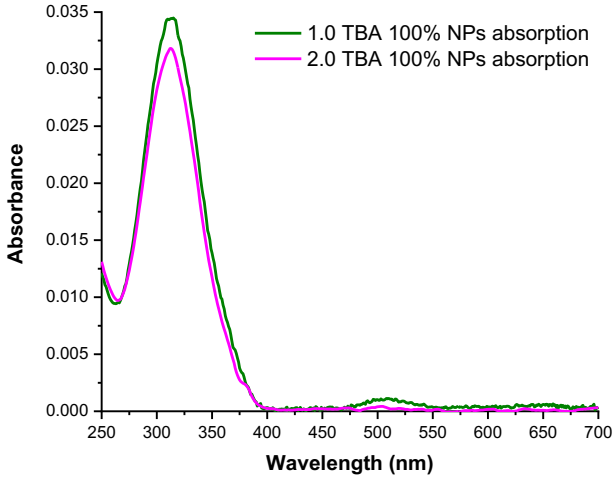

APPENDIX 7

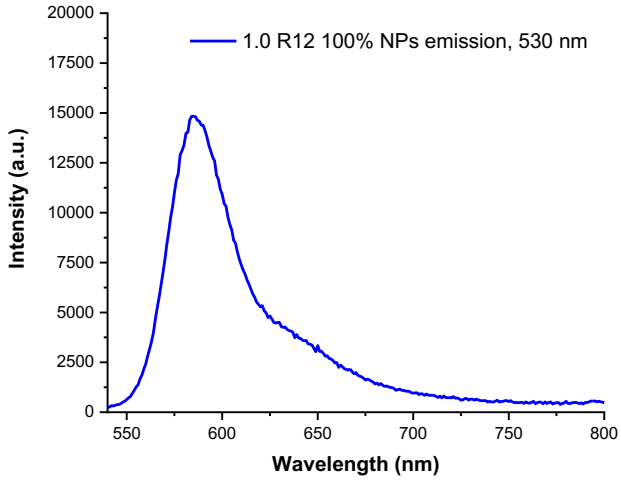

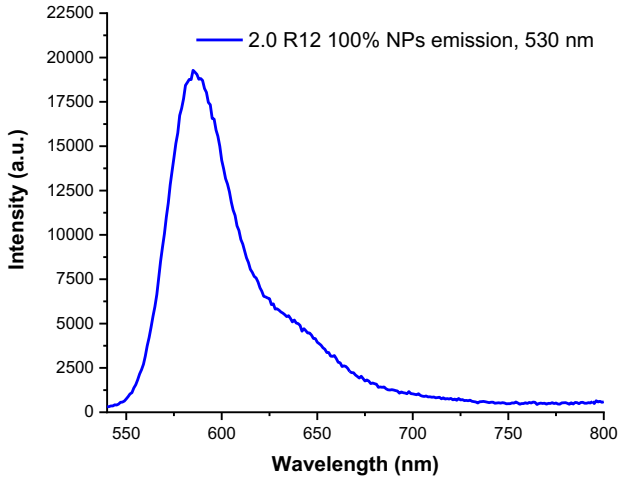

APPENDIX 8

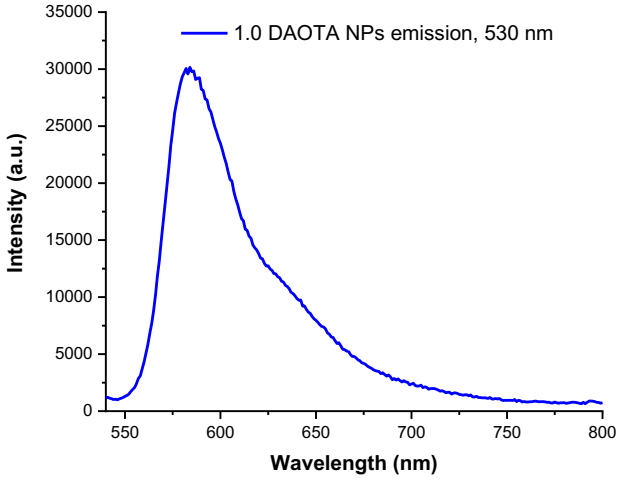

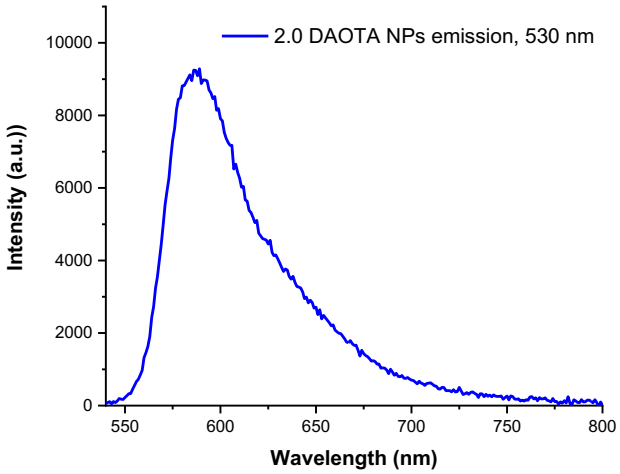

APPENDIX 9

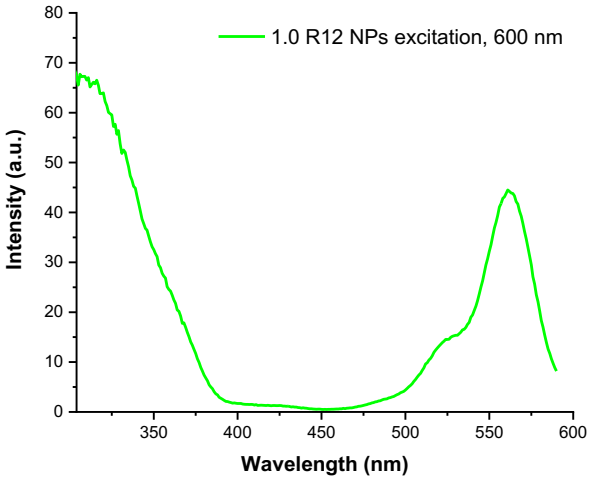

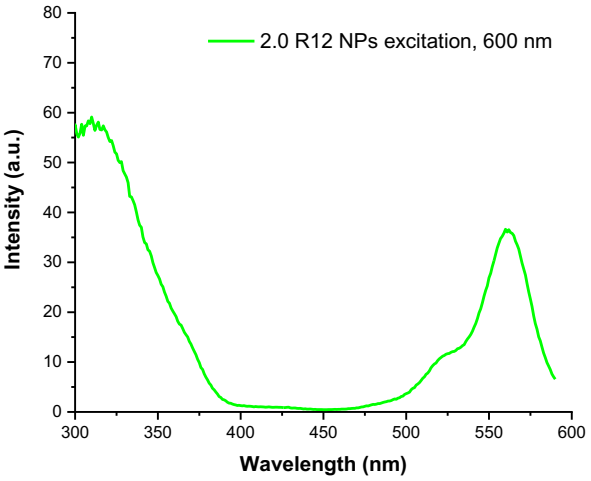

APPENDIX 10

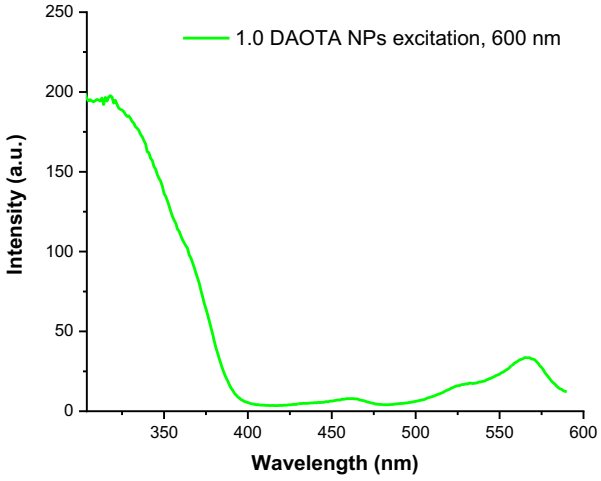

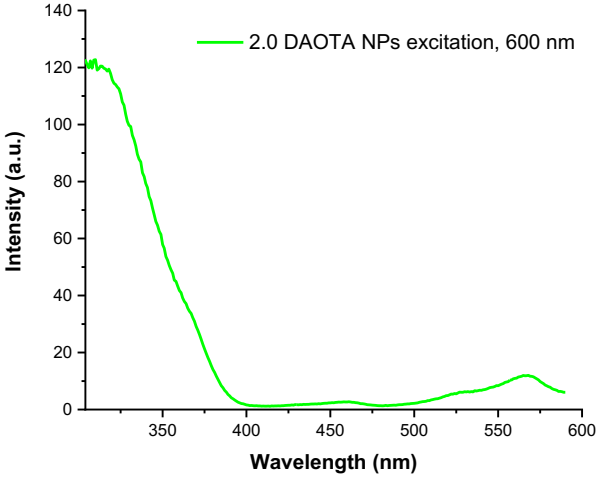

APPENDIX 11

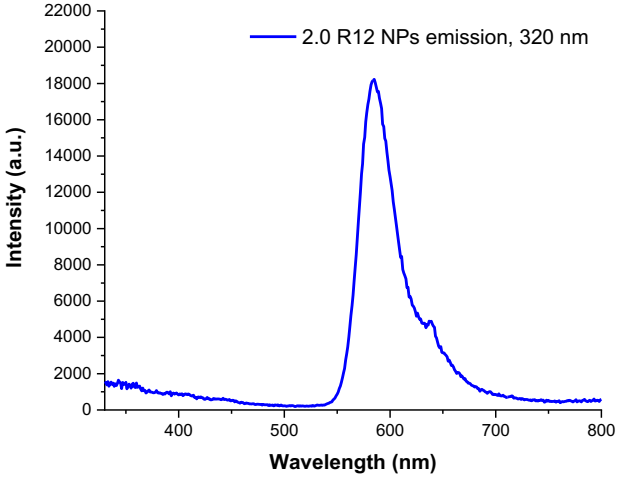

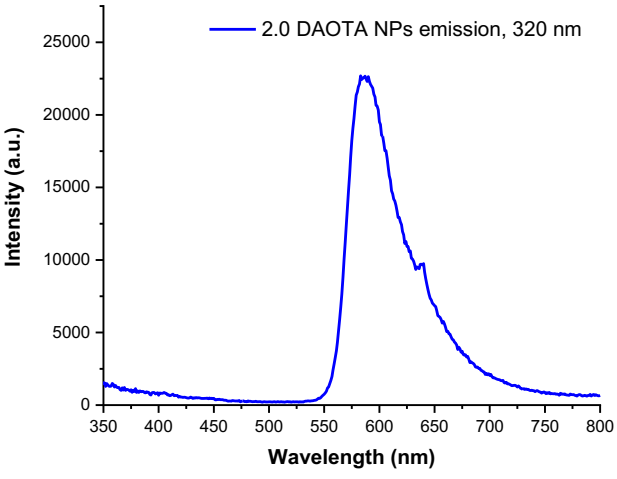

APPENDIX 12

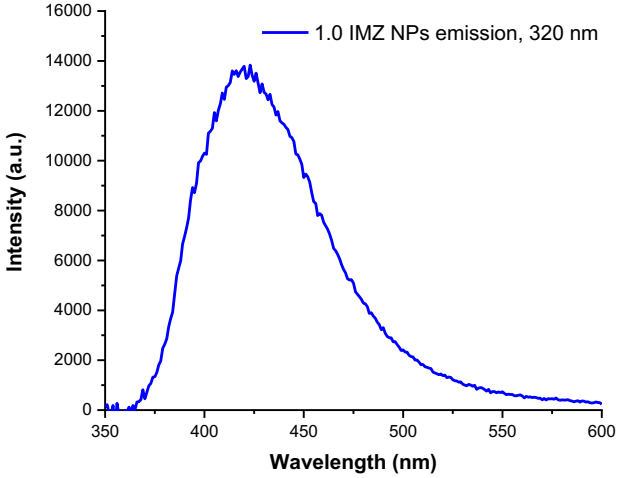

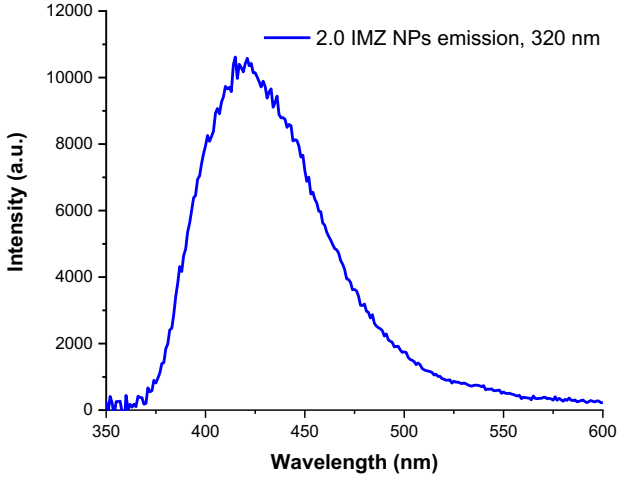

APPENDIX 13

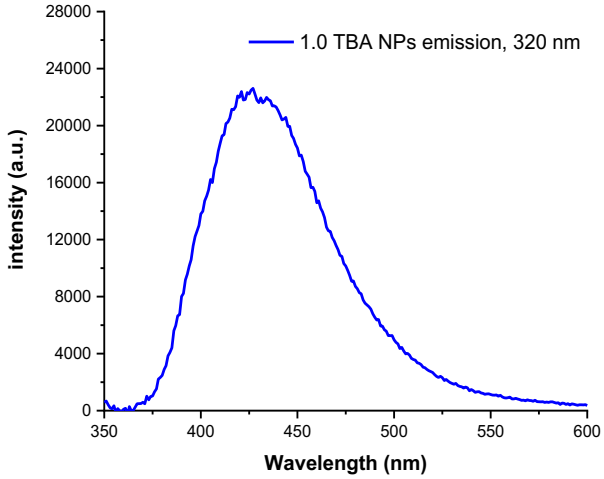

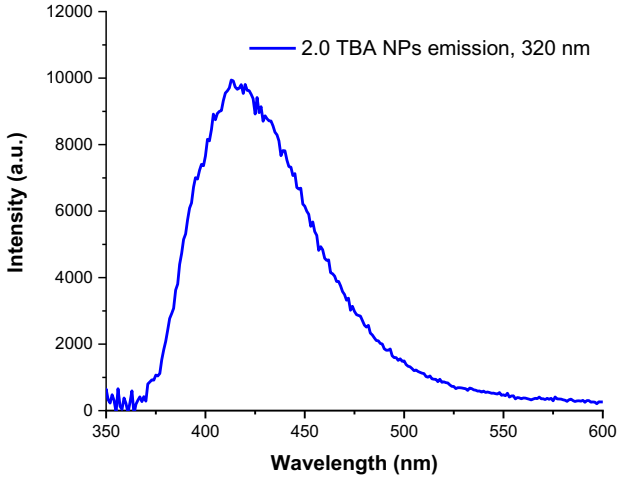

APPENDIX 14

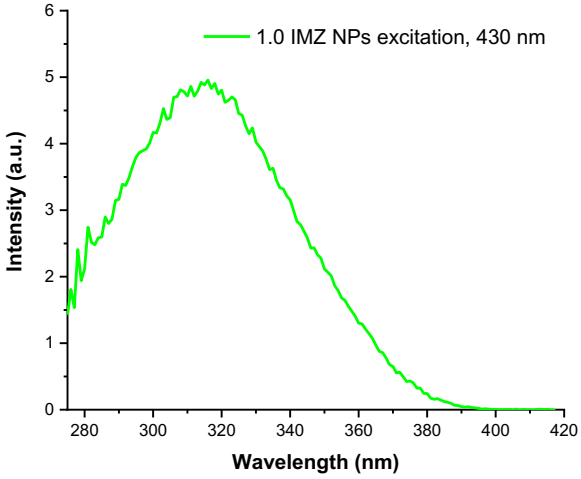

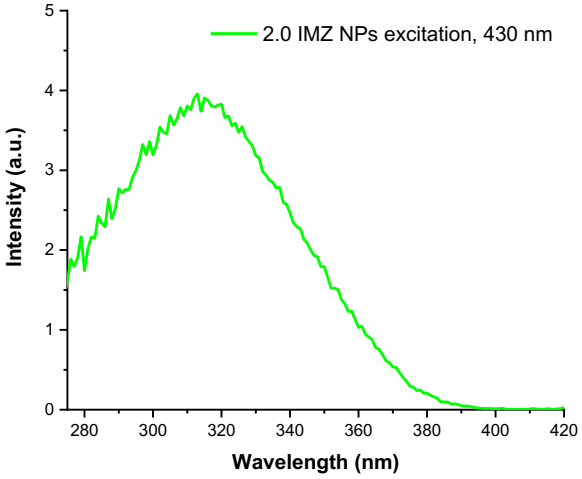

APPENDIX 15

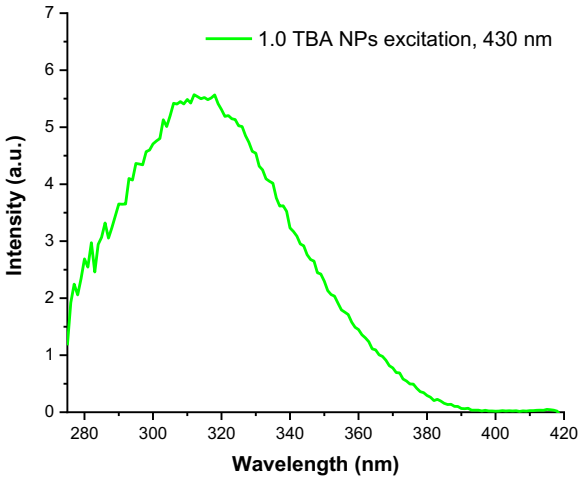

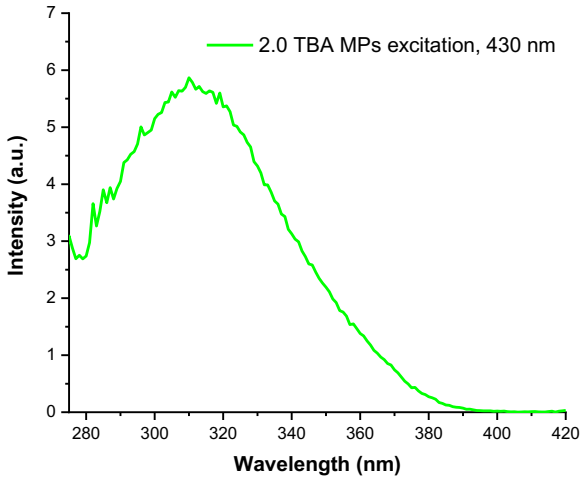

APPENDIX 16

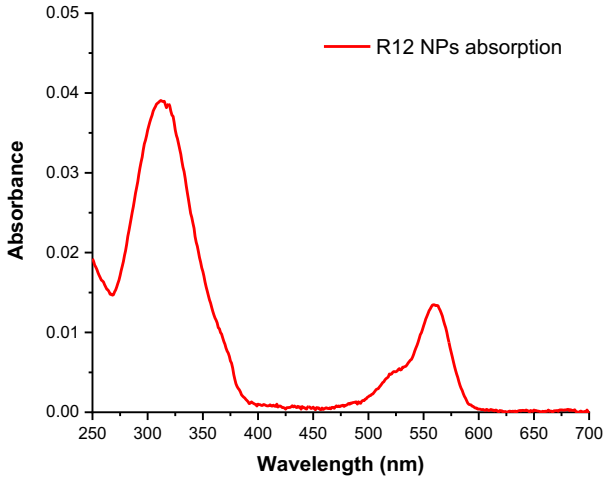

APPENDIX 17

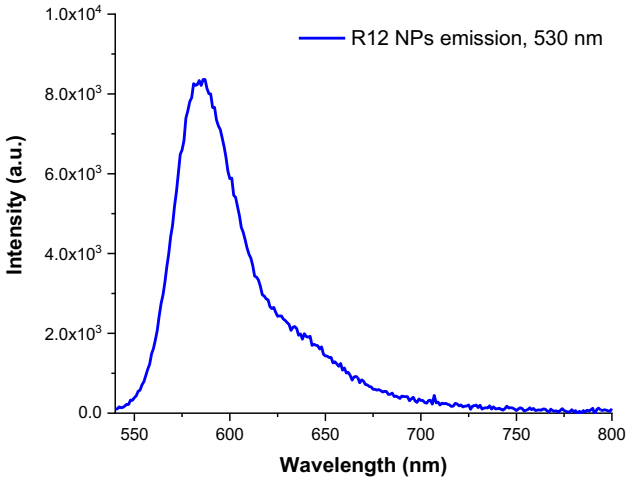

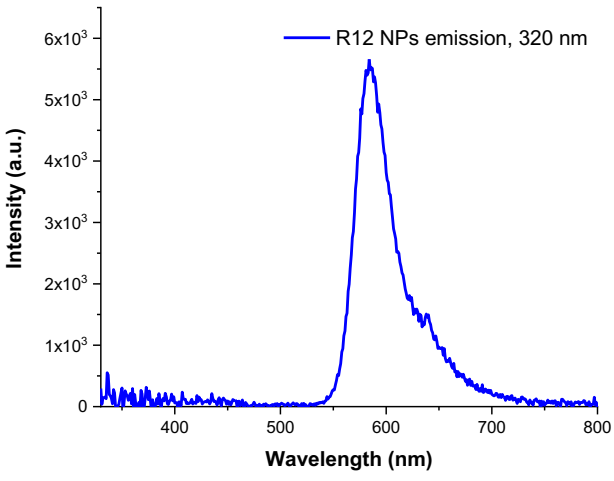

APPENDIX 18

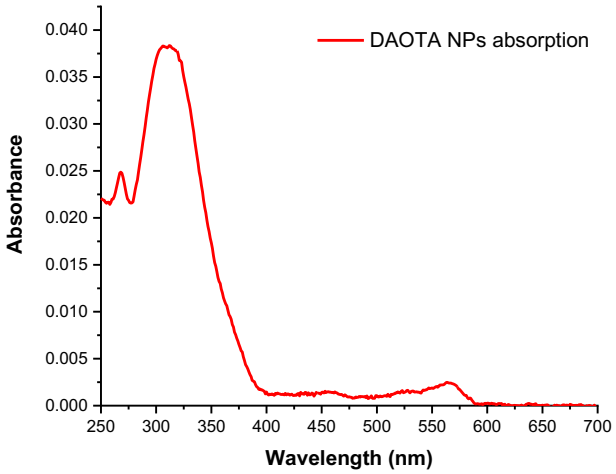

APPENDIX 19

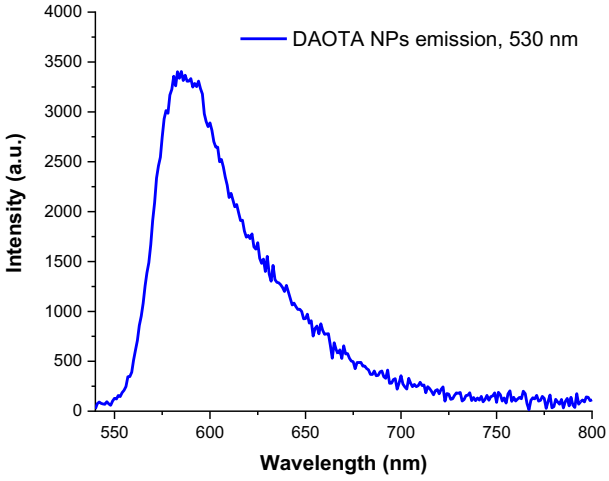

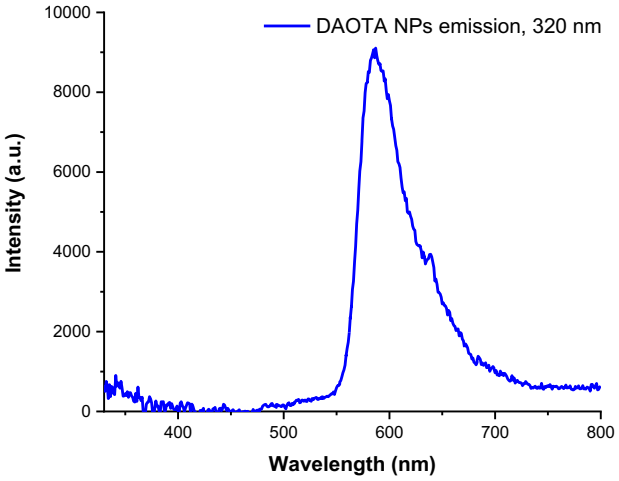

APPENDIX 20

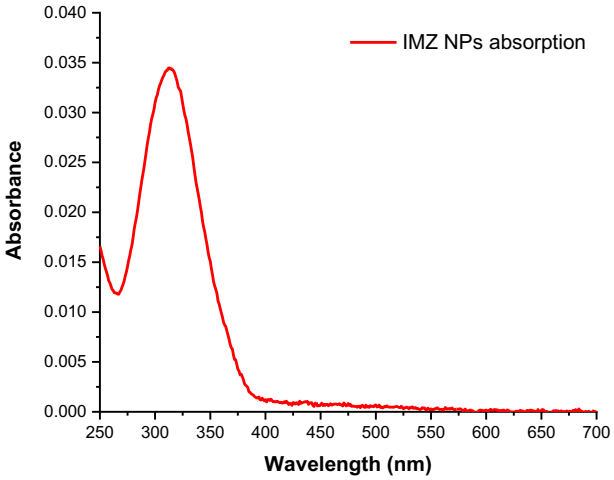

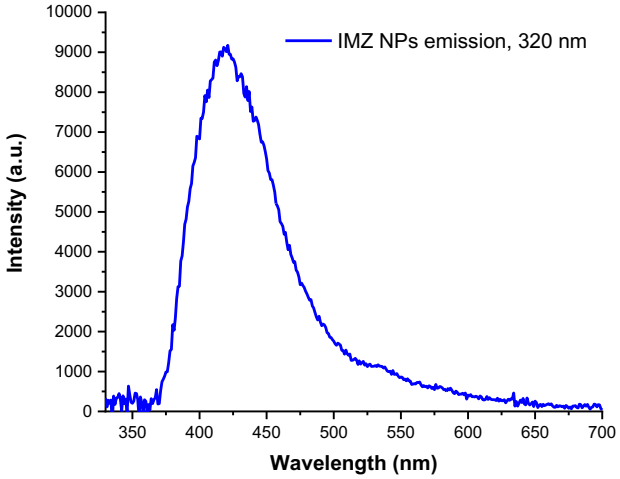

APPENDIX 21

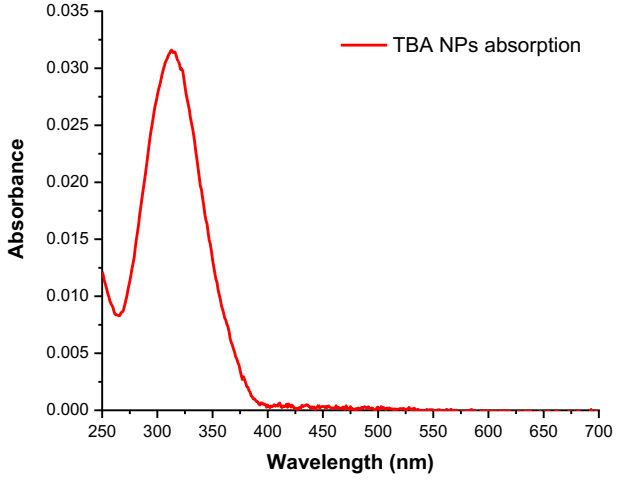

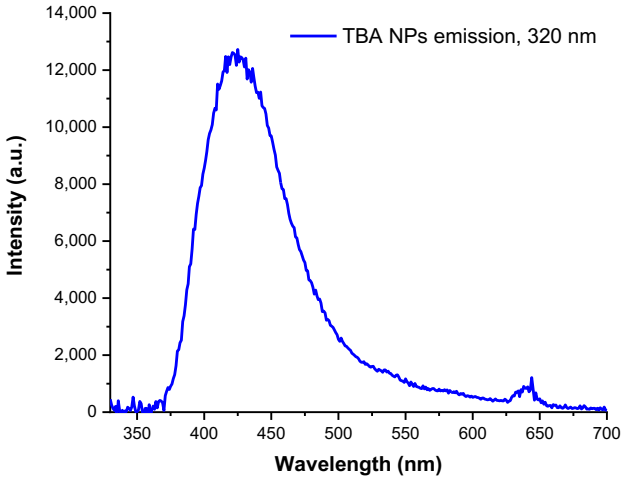

APPENDIX 22

Data Set: 1 / 2

Decay: crv[0]; IRF: crv[2]

Fit

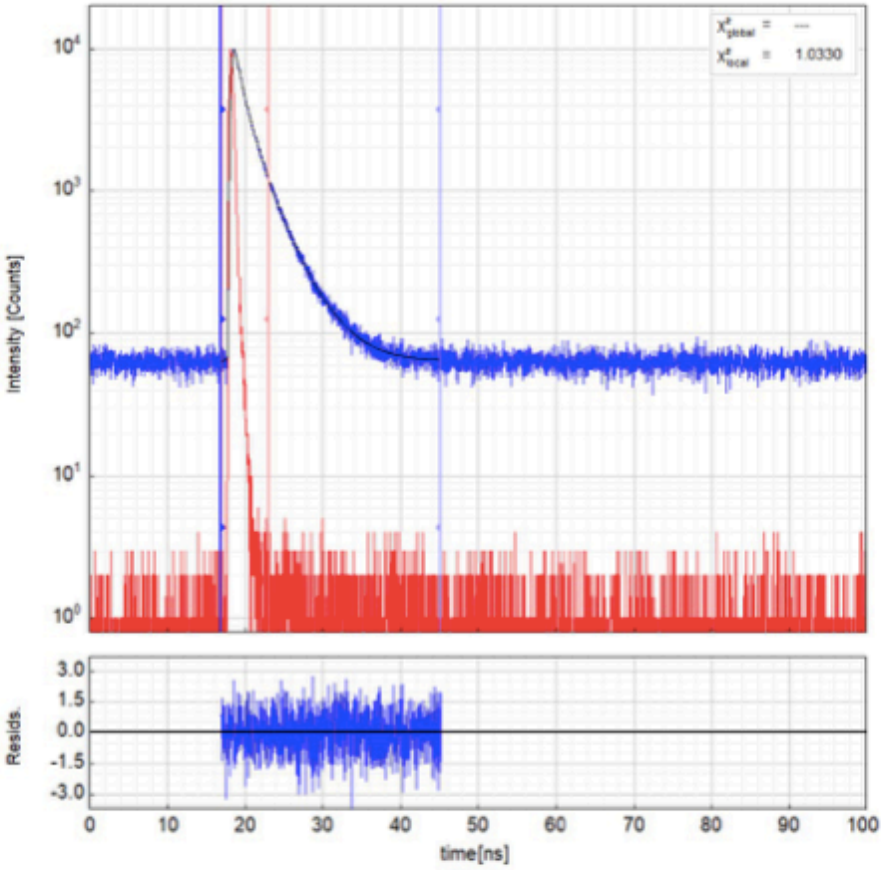

Autocorrelation (Residuals)

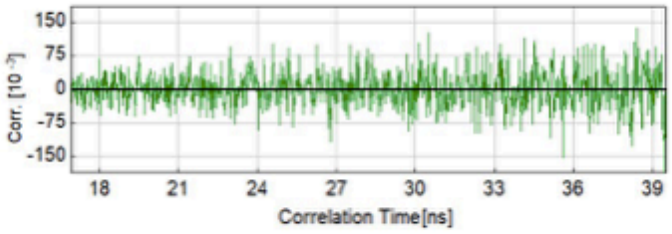

Fitted Parameters

Parameter	Value	Δ	δ
A_1[kCnts/Chnl]	3.44	±0.38	11%
τ_1[ns]	3.43	±0.12	3.5%
I_1[kCnts]	471	±34	7.2%
A_{Rel1}[%]	19.7	±2.2	11%
I_{Rel1}[%]	47.9	±3.6	7.4%
A_2[kCnts/Chnl]	7.01	±0.12	1.6%
τ_2[ns]	1.438	±0.081	5.6%
I_2[kCnts]	403	±25	6.0%
A_{Rel2}[%]	40.2	±0.3	0.7%
I_{Rel2}[%]	41.1	±2.4	5.8%
A_3[kCnts/Chnl]	7.04	±0.39	5.4%
τ_3[ns]	0.387	±0.032	8.0%
I_3[kCnts]	109	±12	11%
A_{Rel3}[%]	40.3	±2.0	4.7%
I_{Rel3}[%]	11.1	±1.2	10%
$Bkgr_{Dec}$[kCnts]	0.0636	±0.0013	1.9%
$Bkgr_{IRF}$[Cnts/Chnl]	-1.0	±1.2	130%
$Shift_{IRF}$[ps]	-49.8	±1.9	3.6%
τ_{AvInt}[ns]	2.275	±0.011	0.5%
τ_{AvAmp}[ns]	1.406	±0.021	1.5%

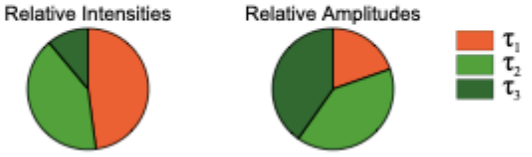

APPENDIX 23

Data Set: 1 / 1

Decay: crv[0]; IRF: crv[1]

Fit

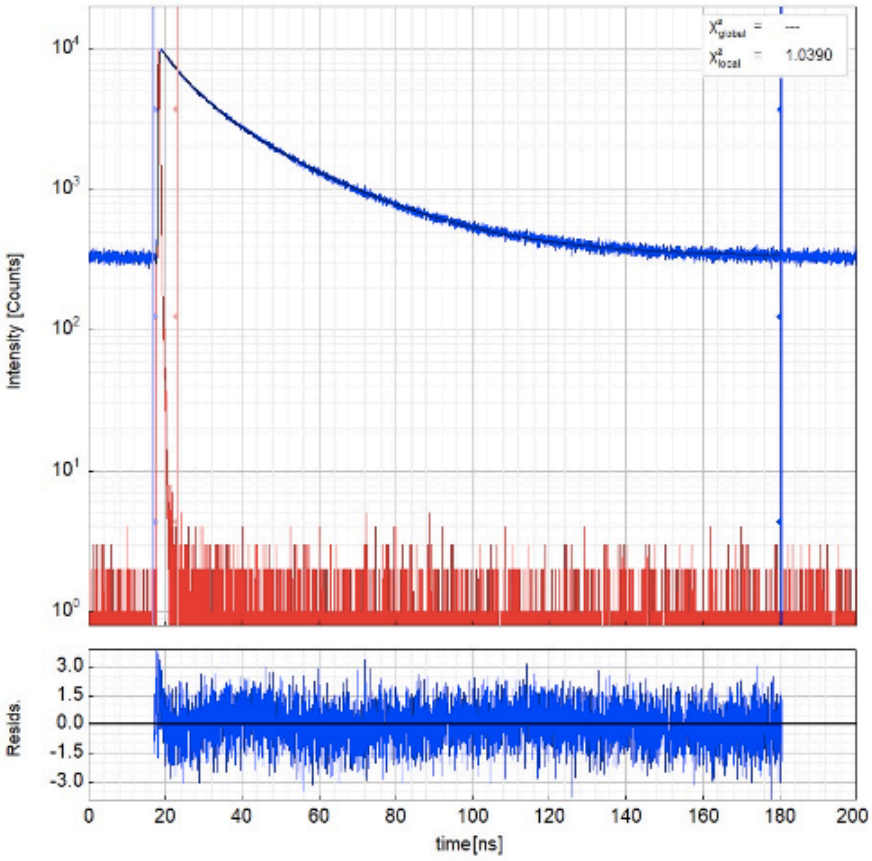

Autocorrelation (Residuals)

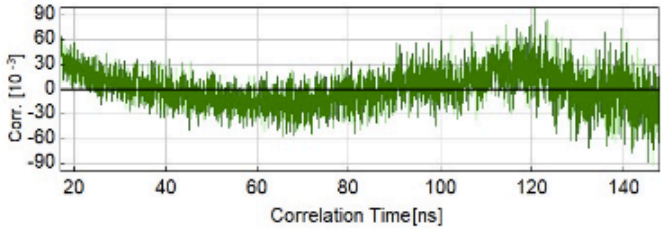

Fitted Parameters

Parameter	Value	Δ	δ
A_1[kCnts/Chnl]	5.070	±0.049	0.9%
τ_1[ns]	7.56	±0.16	2.1%
I_1[kCnts]	1 533	±35	2.3%
A_{Rel1}[%]	49.5	±0.5	0.9%
I_{Rel1}[%]	22.4	±0.6	2.5%
A_2[kCnts/Chnl]	5.193	±0.053	1.0%
τ_2[ns]	25.60	±0.18	0.7%
I_2[kCnts]	5 316	±26	0.5%
A_{Rel2}[%]	50.6	±0.5	0.9%
I_{Rel2}[%]	77.7	±0.6	0.7%
$Bkgr_{Dec}$[kCnts]	0.3347	±0.0009	0.2%
$Bkgr_{IRF}$[Cnts/Chnl]	30.5	±4.2	14%
$Shift_{IRF}$[ps]	-5.6	±3.5	62%
A_{Scatt}[kCnts]	45.0	±1.9	4.1%
τ_{AvInt}[ns]	21.559	±0.071	0.3%
τ_{AvAmp}[ns]	16.685	±0.086	0.5%

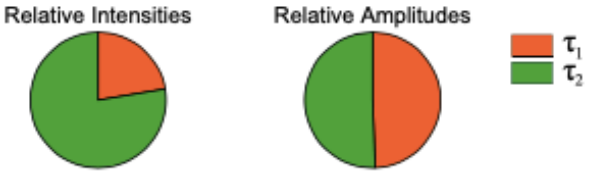

APPENDIX 24

Data Set: 1 / 2

Decay: crv[0]; IRF: crv[2]

Fit

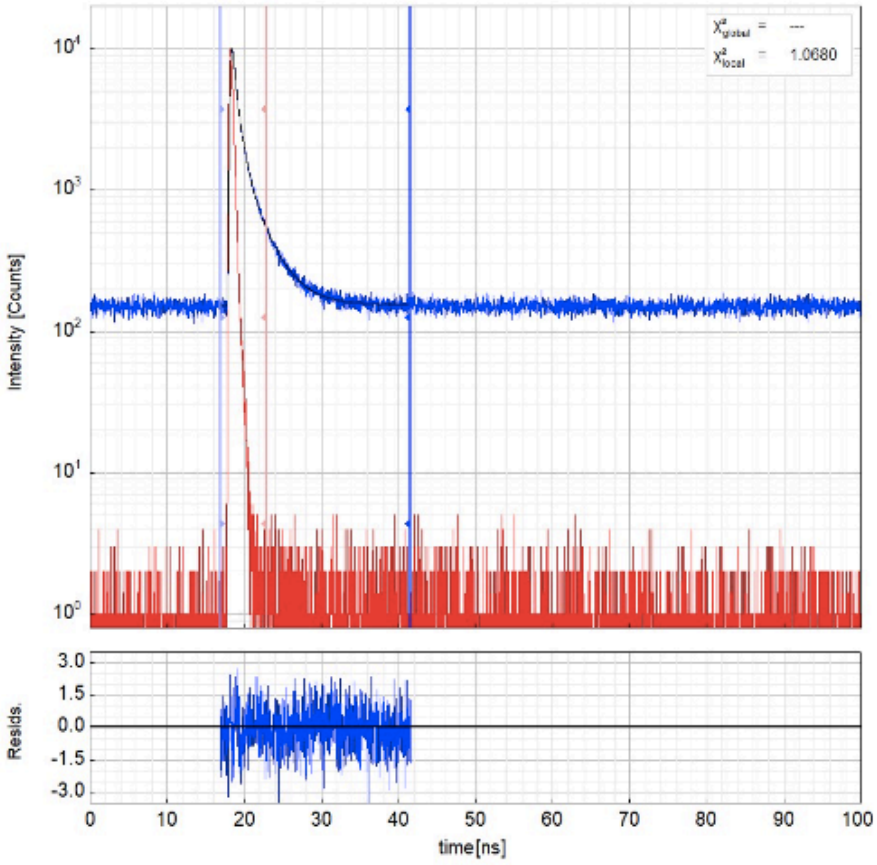

Autocorrelation (Residuals)

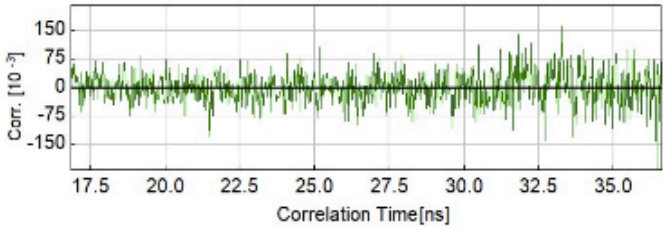

Fitted Parameters

Parameter	Value	Δ	δ
A_1[kCnts/Chnl]	29.8	±1.2	3.8%
τ_1[ns]	0.1528	±0.0092	6.0%
I_1[kCnts]	181.9	±5.2	2.9%
A_{Rel1}[%]	79.9	±0.7	0.8%
I_{Rel1}[%]	31.8	±0.9	2.8%
A_2[kCnts/Chnl]	1.96	±0.18	8.9%
τ_2[ns]	2.676	±0.091	3.4%
I_2[kCnts]	210	±13	5.8%
A_{Rel2}[%]	5.3	±0.3	4.8%
I_{Rel2}[%]	36.6	±2.1	5.5%
A_3[kCnts/Chnl]	5.58	±0.22	3.8%
τ_3[ns]	0.817	±0.056	6.8%
I_3[kCnts]	182.1	±3.3	1.8%
A_{Rel3}[%]	15.0	±0.5	2.7%
I_{Rel3}[%]	31.8	±0.6	1.9%
$Bkgr_{Dec}$[kCnts]	0.1551	±0.0006	0.3%
$Bkgr_{IRF}$[Cnts/Chnl]	2.2	±1.1	49%
$Shift_{IRF}$[ps]	-30.1	±1.8	5.9%
τ_{AvInt}[ns]	1.285	±0.011	0.9%
τ_{AvAmp}[ns]	0.385	±0.015	3.9%

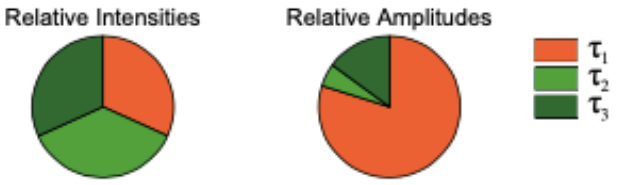

APPENDIX 25

Data Set: 2 / 2

Decay: crv[1]; IRF: crv[2]

Fit

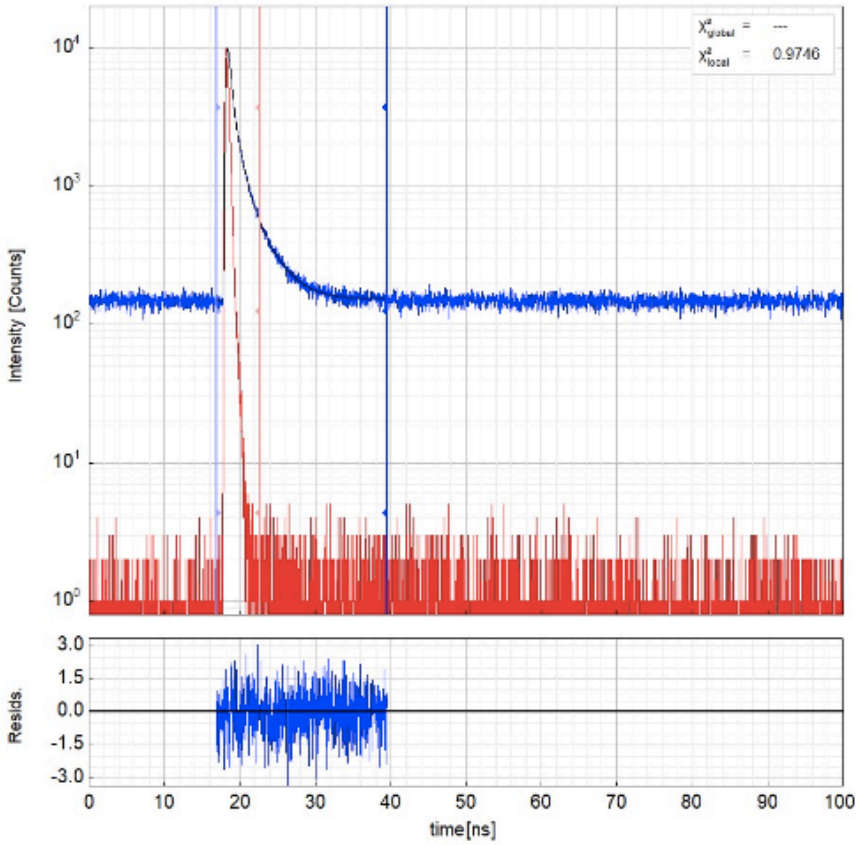

Autocorrelation (Residuals)

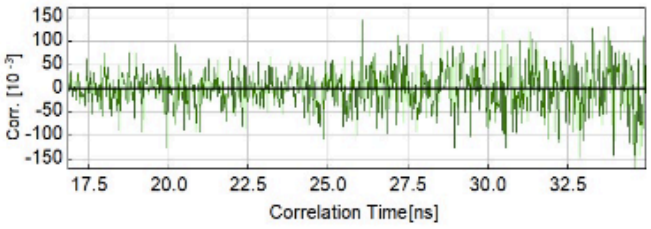

Fitted Parameters

Parameter	Value	Δ	δ
A_1[kCnts/Chnl]	29.8	±1.1	3.4%
τ_1[ns]	0.154	±0.012	7.3%
I_1[kCnts]	182.0	±6.9	3.8%
A_{Rel1}[%]	80.6	±0.9	1.0%
I_{Rel1}[%]	32.5	±1.3	3.9%
A_2[kCnts/Chnl]	5.21	±0.31	5.8%
τ_2[ns]	0.819	±0.067	8.1%
I_2[kCnts]	170.4	±7.5	4.4%
A_{Rel2}[%]	14.2	±0.5	3.4%
I_{Rel2}[%]	30.5	±1.3	4.2%
A_3[kCnts/Chnl]	1.97	±0.19	9.5%
τ_3[ns]	2.65	±0.11	4.1%
I_3[kCnts]	208	±13	5.9%
A_{Rel3}[%]	5.4	±0.4	7.1%
I_{Rel3}[%]	37.2	±2.2	5.8%
$Bkgr_{Dec}$[kCnts]	0.1528	±0.0015	0.9%
$Bkgr_{IRF}$[Cnts/Chnl]	4.4	±1.5	35%
$Shift_{IRF}$[ps]	-26.1	±1.9	7.2%
τ_{AvInt}[ns]	1.280	±0.017	1.3%
τ_{AvAmp}[ns]	0.380	±0.017	4.4%

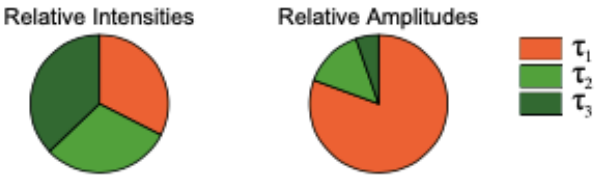

APPENDIX 26

Data Set: 1 / 1

Decay: crv[0]; IRF: crv[1]

Fit

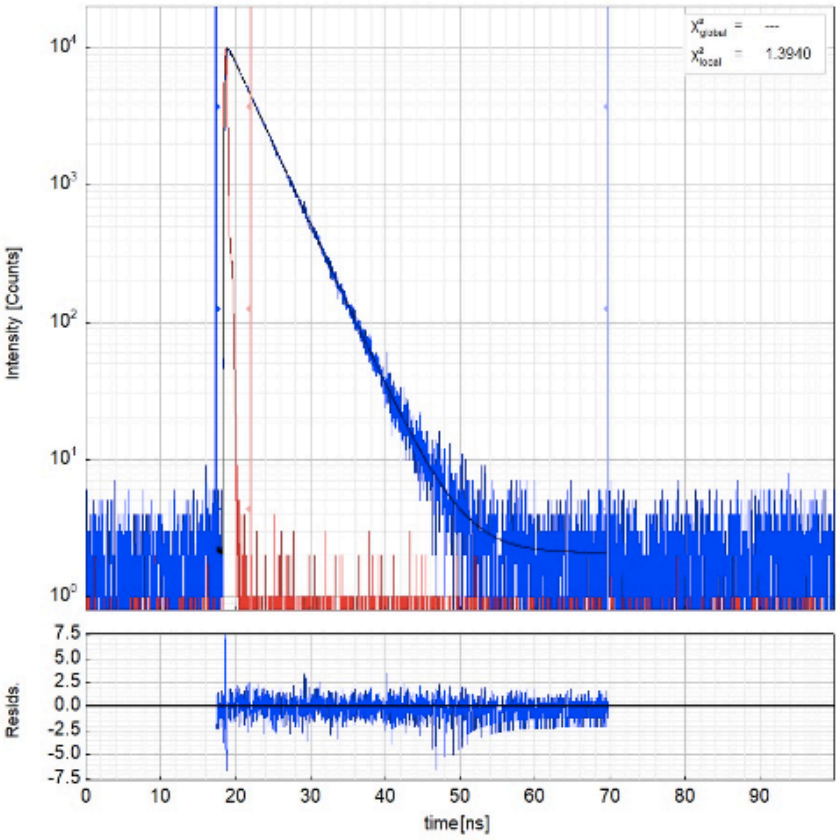

Autocorrelation (Residuals)

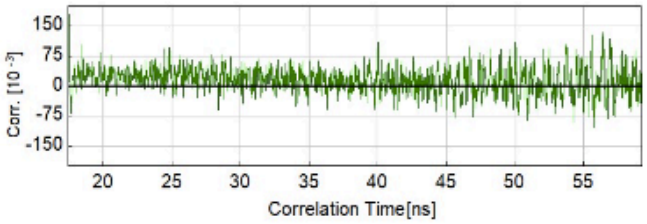

Fitted Parameters

Parameter	Value	Δ	δ
A_1[kCnts/Chnl]	640	±350	55%
τ_1[ns]	0.0095	±0.0013	14%
I_1[kCnts]	240	±90	37%
A_{Rel1}[%]	98.3	±0.7	0.7%
I_{Rel1}[%]	12.8	±4.0	31%
A_2[kCnts/Chnl]	11.097	±0.030	0.3%
τ_2[ns]	3.6774	±0.0049	0.1%
I_2[kCnts]	1 632.3	±2.6	0.2%
A_{Rel2}[%]	1.8	±0.7	40%
I_{Rel2}[%]	87.3	±4.0	4.6%
$Bkgr_{Dec}$[kCnts]	0.0021	±0.0001	2.7%
$Bkgr_{IRF}$[Cnts/Chnl]	0.20	±0.22	112%
$Shift_{IRF}$[ps]	-9.8	±3.0	30%
τ_{AvInt}[ns]	3.21	±0.15	4.6%
τ_{AvAmp}[ns]	0.073	±0.027	36%

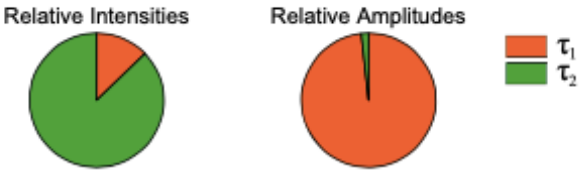

APPENDIX 27

Data Set: 1 / 1

Decay: crv[0]; IRF: crv[1]

Fit

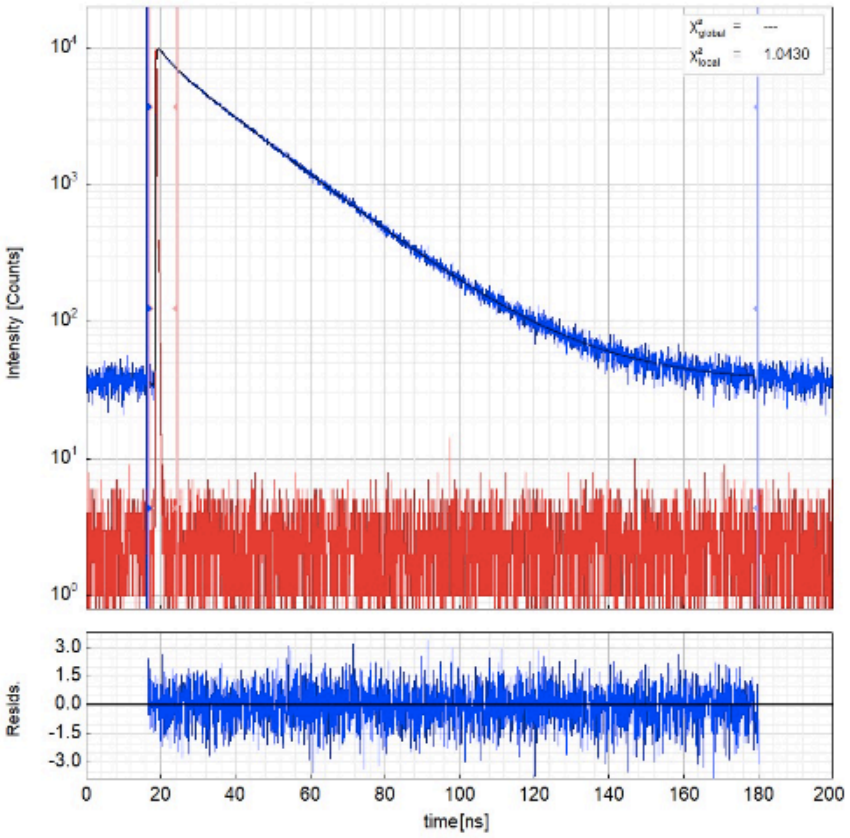

Autocorrelation (Residuals)

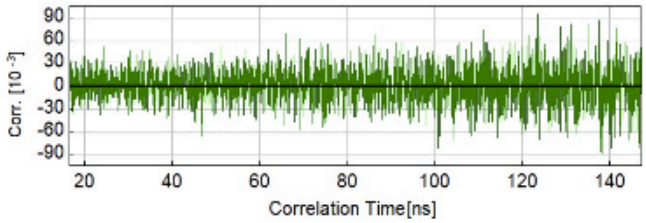

Fitted Parameters

Parameter	Value	Δ	δ
A_1[kCnts/Chnl]	2.106	±0.026	1.2%
τ_1[ns]	3.476	±0.084	2.4%
I_1[kCnts]	146.4	±3.0	2.0%
A_{Rel1}[%]	19.5	±0.2	1.0%
I_{Rel1}[%]	4.0	±0.1	2.2%
A_2[kCnts/Chnl]	8.697	±0.019	0.2%
τ_2[ns]	20.636	±0.025	0.1%
I_2[kCnts]	3 589.1	±3.7	0.1%
A_{Rel2}[%]	80.6	±0.2	0.2%
I_{Rel2}[%]	96.1	±0.1	0.1%
$Bkgr_{Dec}$[kCnts]	0.0367	±0.0002	0.5%
$Bkgr_{IRF}$[Cnts/Chnl]	3.04	±0.40	13%
$Shift_{IRF}$[ps]	13.28	±0.68	5.1%
τ_{AvInt}[ns]	19.963	±0.017	0.1%
τ_{AvAmp}[ns]	17.291	±0.046	0.3%

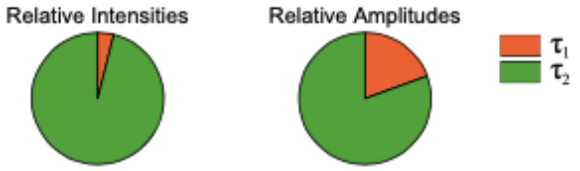

APPENDIX 28

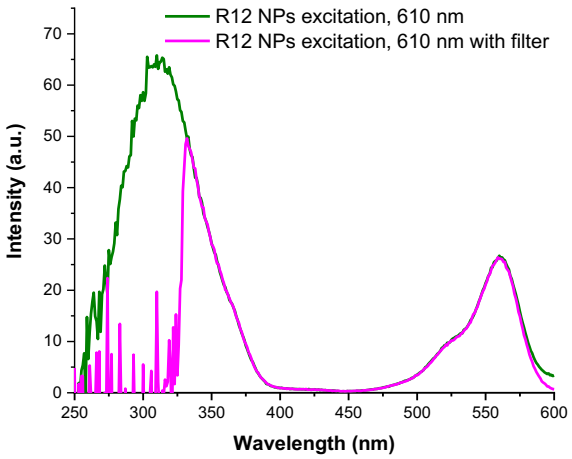

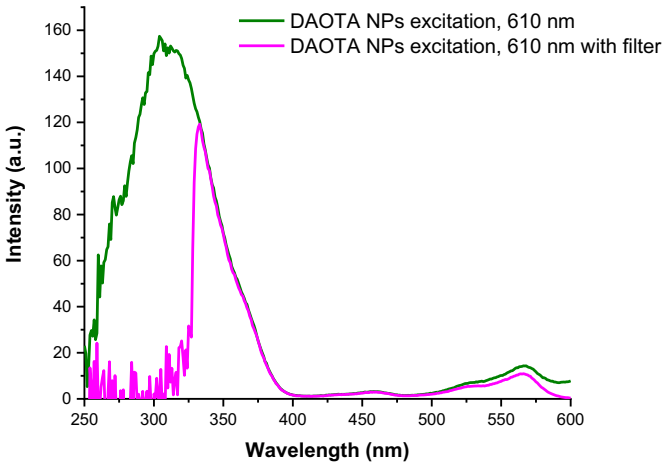

APPENDIX 29

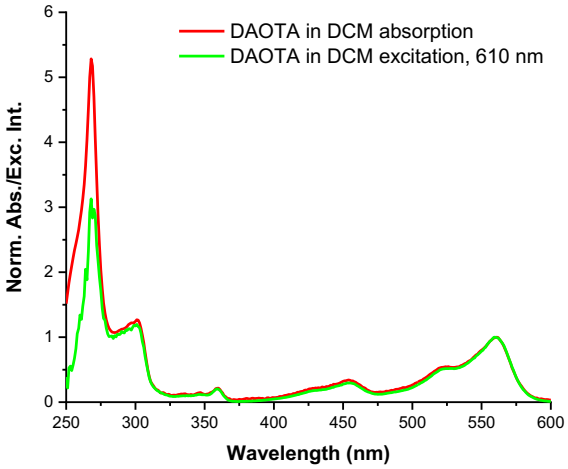

APPENDIX 30

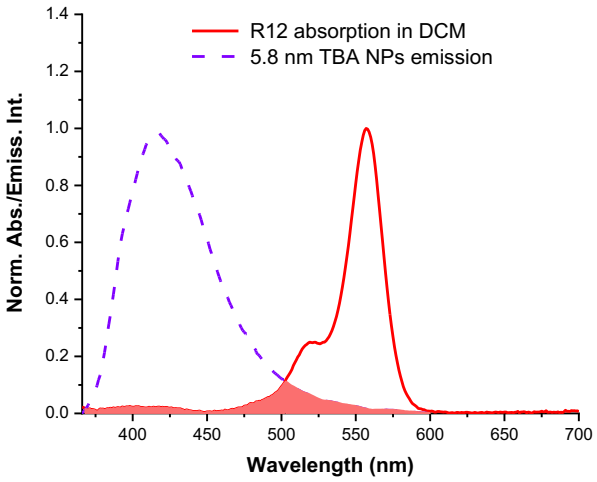

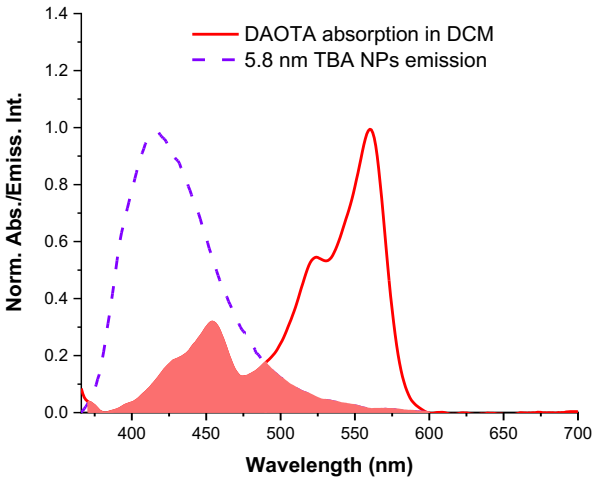

APPENDIX 31